

Human occupation of northern Australia by 65,000 years ago

Chris Clarkson¹, Zenobia Jacobs^{2,3}, Ben Marwick^{3,4}, Richard Fullagar³, Lynley Wallis⁵, Mike Smith⁶, Richard G. Roberts^{2,3}, Elspeth Hayes³, Kelsey Lowe¹, Xavier Carah¹, S. Anna Florin¹, Jessica McNeil^{1,7}, Delyth Cox¹, Lee J. Arnold⁸, Quan Hua⁹, Jillian Huntley¹⁰, Helen E. A. Brand¹¹, Tiina Manne¹, Andrew Fairbairn¹, James Shulmeister¹², Lindsey Lyle⁴, Makiah Salinas⁴, Mara Page⁴, Kate Connell¹, Gayoung Park⁴, Kasih Norman¹, Tessa Murphy⁴ & Colin Pardoe¹³

The time of arrival of people in Australia is an unresolved question. It is relevant to debates about when modern humans first dispersed out of Africa and when their descendants incorporated genetic material from Neanderthals, Denisovans and possibly other hominins. Humans have also been implicated in the extinction of Australia's megafauna. Here we report the results of new excavations conducted at Madjedbebe, a rock shelter in northern Australia. Artefacts in primary depositional context are concentrated in three dense bands, with the stratigraphic integrity of the deposit demonstrated by artefact refits and by optical dating and other analyses of the sediments. Human occupation began around 65,000 years ago, with a distinctive stone tool assemblage including grinding stones, ground ochres, reflective additives and ground-edge hatchet heads. This evidence sets a new minimum age for the arrival of humans in Australia, the dispersal of modern humans out of Africa, and the subsequent interactions of modern humans with Neanderthals and Denisovans.

The date when humans first arrived in Sahul—the combined Pleistocene landmass of Australia and New Guinea—remains a contested issue. Resolving this question has important implications for debates about the timing and rate of dispersal of modern humans out of Africa and across south Asia^{1–3}, and when and where genetic material was transferred between archaic hominins and modern humans^{4–7}. The impact of humans on Australia's ecosystems has also been a long-standing topic of discussion^{8–12}.

Current estimates of the time of initial human colonization of Australia range from 47 thousand years ago (ka) to around 60 ka (refs 9, 12–23). A key site in this debate is Madjedbebe, a rock shelter in northern Australia formerly known as Malakunanja II, which was excavated in 1973 (ref. 24) and 1989 (ref. 13). The earliest artefacts recovered from the latter excavation included stone tools and ground ochre pieces deposited between about 60 and 50 ka, based on thermoluminescence and optical (optically stimulated luminescence, OSL) dating of the surrounding sediments^{13,16}. These ages, the depositional context of the artefacts and their significance have proved contentious, mainly because of the lack of detailed description of the artefacts and concerns over stratigraphic disturbance of the deposit and how the artefacts relate to the dated sediments^{19–22,25–30}. Here we report the results of new excavations at Madjedbebe, concentrating on evidence regarding the age and stratigraphic integrity of the deposits and associated artefacts in the zone of initial human occupation.

Excavations and stratigraphy

Madjedbebe rock shelter is located on the western edge of the Arnhem Land plateau in the Northern Territory, in Mirarr Country (12° 30' S, 132° 53' E, approximately 20 m above sea level; Fig. 1a, b and Extended

Data Fig. 1b, c). The 1989 excavation¹³ revealed cultural deposits starting at 2.6 m depth below the surface, with a peak in artefact density at 2.5–2.3 m depth below surface. Silcrete flakes, ground ochre, a grindstone and more than 1,500 stone artefacts were recovered from the lowest occupation levels²². The associated sediments were dated to around 60–50 ka using thermoluminescence methods, with total uncertainties of 16–20 thousand years (kyr) at the 95.4% confidence level^{15,25}. These ages made Madjedbebe the oldest human occupation site known in Australia; two of these samples were subsequently dated by single-grain OSL methods, which were then under development, and these ages supported the early thermoluminescence chronology^{16,29,30}. We conducted new excavations at Madjedbebe in 2012 and 2015 to obtain additional artefacts and sediment samples for high-resolution OSL dating from the zone of the initial occupation, in particular.

We excavated twenty 1 × 1 m squares adjacent to, and enclosing, the original excavations (Fig. 1c) to a maximum depth of 3.4 m. The three-dimensional coordinates of approximately 11,000 artefacts and other anthropogenic features (hearths, burials and pits) were recorded and samples were collected for chronological, geoarchaeological and macrobotanical analyses. We focus here on the northwest squares of the excavation (southwest faces of B4–B6 and northwest face of C4), where the frequency of artefacts and the number of OSL samples is greatest (Extended Data Fig. 1a) and refer to other squares for ancillary data.

The basal deposits consist of culturally sterile orange sands. The lowest artefacts were recovered from the overlying unit (around 0.7 m thick and composed of well-sorted medium-coarse pink sand), which dips at a low angle (around 5°) towards the front of the shelter. The upper boundary of this unit occurs at 2.0–2.5 m depth (increasing with distance from the back wall; Extended Data Fig. 1a), where it

¹School of Social Science, University of Queensland, Brisbane, Queensland 4072, Australia. ²Australian Research Council (ARC) Centre of Excellence for Australian Biodiversity and Heritage, University of Wollongong, Wollongong, New South Wales 2522, Australia. ³Centre for Archaeological Science, School of Earth and Environmental Sciences, University of Wollongong, Wollongong, New South Wales 2522, Australia. ⁴Department of Anthropology, University of Washington, Seattle, Washington 98195, USA. ⁵Nulungu Research Institute, University of Notre Dame, Broome, Western Australia 6725, Australia. ⁶Centre for Historical Research, National Museum of Australia, Canberra, Australian Capital Territory 2601, Australia. ⁷Department of Anthropology, Harvard University, Cambridge, Massachusetts 02143, USA. ⁸School of Physical Sciences, the Environment Institute and the Institute for Photonics and Advanced Sensing, University of Adelaide, Adelaide, South Australia 5005, Australia. ⁹Australian Nuclear Science and Technology Organisation, Lucas Heights, New South Wales 2234, Australia. ¹⁰Place, Evolution, Rock Art, Heritage Unit, School of Humanities, Griffith University, Nathan, Queensland 4222, Australia. ¹¹Australian Synchrotron, 800 Blackburn Road, Clayton, Victoria 3168, Australia. ¹²School of Earth and Environmental Sciences, University of Queensland, Brisbane, Queensland 4072, Australia. ¹³Archaeology and Natural History, School of Culture, History and Language, The Australian National University, Canberra, Australian Capital Territory 2601, Australia.

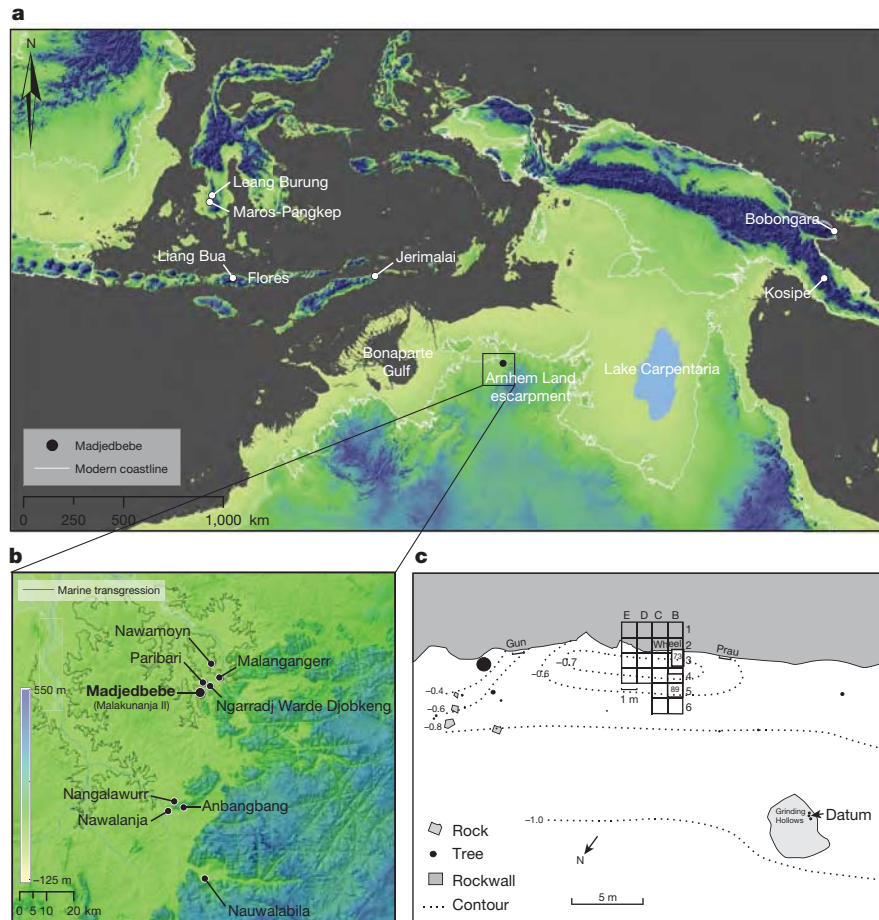


Figure 1 | Site location and stratigraphy. **a**, Regional map showing the location of Madjedbebe in relation to the coastline at 65 ka and the current coastline (white line), and other ancient archaeological sites in Australia and southeast Asia (bathymetric data GEBCO 2014 Grid, version 20150318, <http://www.gebco.net>). **b**, Location of Madjedbebe in relation to

other key archaeological sites in Kakadu National Park, and the location of the high sea-level stand during the last marine transgression about 6–7 ka (topographic data Geoscience Australia 1 arc-second DEM). **c**, Site plan showing the 1973, 1989, 2012 and 2015 excavation squares. Squares E1–B2 were located beneath the sloping back wall.

grades diffusely into poorly sorted medium–coarse (light) brown sands. Organic inclusions are rare, but spalled fragments of bedrock are common, especially near the dripline in square B6. No stone lines, pavements or imbricated structures were encountered during the excavation. The brown sands are compacted below about 1.5 m depth, but become softer and encrusted with carbonates closer to its diffuse contact with the overlying midden (approximately 0.5 m thick). The latter consists of brown silty sand, abundant gastropod shells, numerous bone specimens and some plant roots, and is buried beneath a loose surface layer of dark sandy silt containing abundant charcoal fragments. Most archaeofaunal remains were recovered from this Holocene midden, with some degraded bone found to a depth of 1.76 m. Midden bone is exceptionally well-preserved, including a maxillary fragment of a thylacine (*Thylacinus cynocephalus*) coated in red pigment (Fig. 2o–q).

Artefacts and depositional integrity

Artefacts occur in three dense bands (Extended Data Figs 1, 2), with fewer artefacts in the intervening deposits. Each band corresponds to a change in raw material use and stone working technology (Extended Data Fig. 2a, b) and there is no size sorting of artefacts with depth (posterior r^2 distribution, 95% credible interval: 0.0004–0.0049). These observations imply overall stratigraphic integrity of the deposit.

The lowest dense band (phase 2) at 2.60–2.15 m depth in squares B4–B6 represents the zone of first occupation; it contains an *in situ* hearth and an assemblage of distinctive stone artefacts made mostly from quartzite, silcrete, mudstone and dolerite (Fig. 2 and Extended Data Fig. 2b). The assemblage includes a number of distinctive artefact

types, such as thinning flakes and snapped points (Fig. 2c, d), faceted discoidal cores (Fig. 2h), grinding stones (Fig. 2e, f and Extended Data Fig. 3), whole and fragments of edge-ground hatchets (Fig. 2a, b and Extended Data Fig. 4), ground ochres (Fig. 2g) and fragments of sheet mica (Fig. 2k)—several of which were wrapped around a large piece of ground yellow ochre (Fig. 2k–m).

Artefact residues and macrofossil remains demonstrate exploitation of fuel wood and a range of plant foods (seeds, tubers and *Pandanus* sp. nuts; Extended Data Fig. 5b–d) from the local eucalyptus and monsoon vine thicket forest. The middle dense band (phase 4) at 1.55–0.95 m depth shows an increase in the use of bipolar technology (Extended Data Fig. 2c); quartzite is rare and quartz is abundant (Extended Data Fig. 2b). The upper dense band (0.70–0.35 m depth) is dominated by quartz and chert artefacts with single and multiplatform cores (Extended Data Fig. 2b, c).

Three lines of evidence suggest that post-depositional vertical mixing of the deposit and artefact movement is restricted to depths of approximately 10 cm. First, we refitted silcrete artefacts from the lower and middle dense bands, and found 14 and 3 refits within these two bands, respectively, but not between them (Extended Data Fig. 6); the median vertical distance between refitted pieces is 10.6 cm. The limited downward movement of artefacts is consistent with the outcome of modern trampling experiments at Madjedbebe³¹. Second, burnt artefacts are more abundant in these two bands—indicating a probable association with intense anthropogenic burning—than in the intervening deposits (Extended Data Fig. 7b); their vertical separation, and the presence of intact hearths, argues against mixing and stratigraphic disturbance over

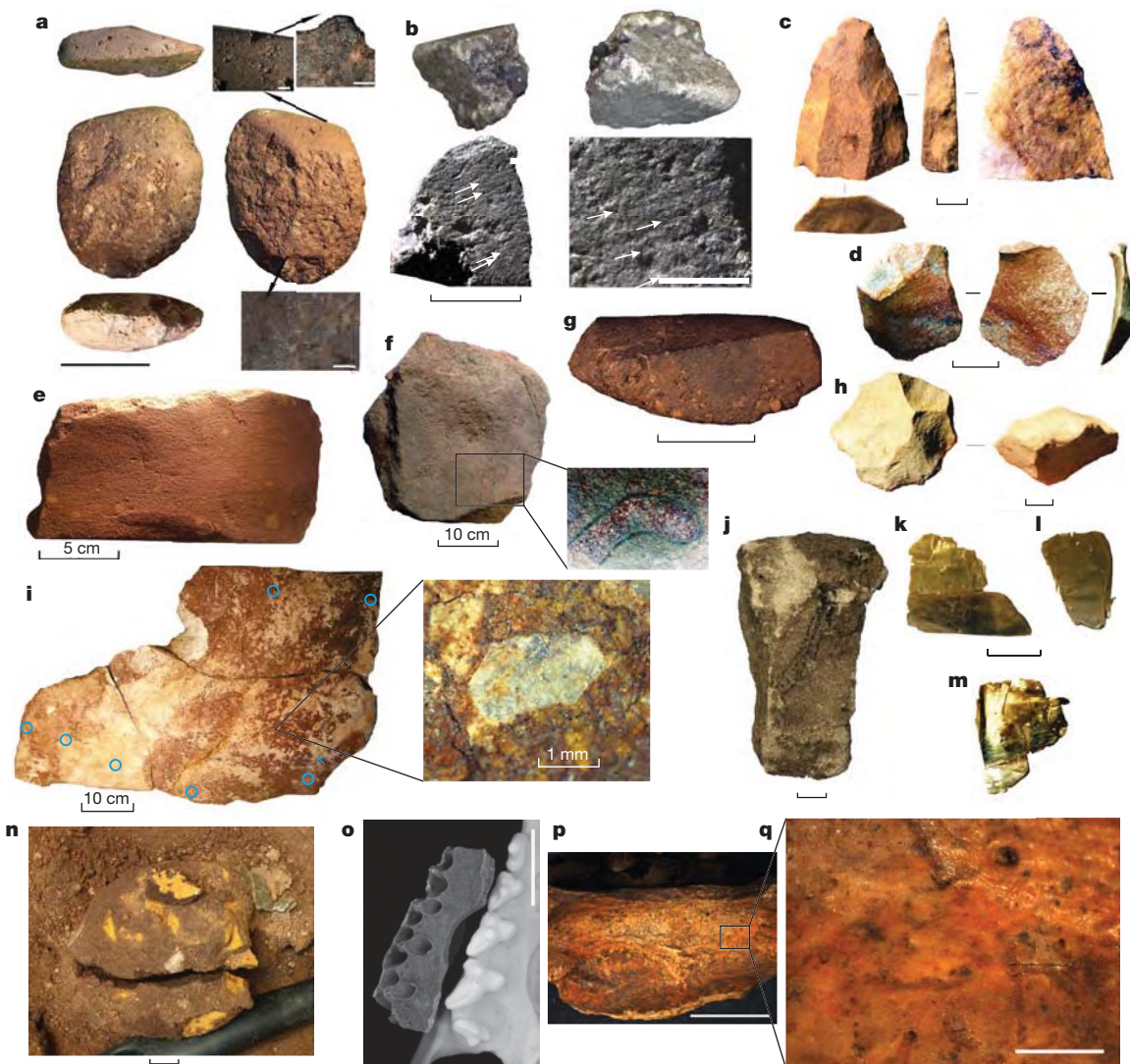


Figure 2 | Artefacts from the 2012 and 2015 excavations. All artefacts are from phase 2 except i (phase 3), f and j (phase 4). Scale bars are 1 cm unless indicated otherwise. **a**, Ground hatchet head number 9 from B1/36 (phase 2). Scale bar, 5 cm. Top insets and micrographs show striations and grinding (left; scale bar, 2 mm) and edge rounding and polish from use (right; scale bar, 0.2 mm). Bottom micrograph and inset show polish (scale bar, 0.2 mm) from movement inside the haft. **b**, Edge-ground margin on flake UPAF51 C2/52 (phase 2). Scale bar, 5 mm. Bottom-right inset (scale bar, 2 mm) shows striations (arrows) from use and grinding. Top-left, the ground edge is shown viewed from the side. Top-right, the ground edge is shown viewed from the front. **c**, Invasively retouched silcrete point from C6/61. **d**, Silcrete thinning flake B4/43 (1989). **e**, Sandstone grinding stone GS79 from B6/54. **f**, Mortar GS32 from B6/31, used to pound hard plant material and with possible outline motif in the bottom-right

corner. **g**, Ground ochre 'crayon' B6/52. **h**, Faceted discoidal core from C6/42. **i**, Conjoining ochre-covered slab (ART9) from D2/33; inset shows fragment of mica embedded in a thick coating of ochre, with blue circles at the <8.5-mm-diameter pXRF sampling locations. **j**, Charcoal lines and dots on sandstone piece from C2/26. **k–m**, Pieces of sheet mica from C5/56 found wrapped around a large, ground yellow ochre 'crayon' (**n**). **o–q**, Photographs of a maxillary fragment of thylacine or Tasmanian tiger (*Thylacinus cynocephalus*) from C2/9, coated in red pigment. **o**, Archaeological specimen (left) is shown relative to a modern thylacine cast. **p** and **q**, Detail of ochred surface at 6.7× magnification (scale bar, 10 mm) and 45× magnification (scale bar, 1 mm), respectively. The probable age of the thylacine specimen is 2.7–3.9 calibrated kyr BP, as indicated by ¹⁴C ages for spit 9 in the surrounding squares (D3 and C4).

depths of several decimetres. Third, micromorphological observations indicate only small-scale reworking of the Pleistocene deposits: sand-sized quartz grains have cappings and linked-cappings of fine silt grains (Extended Data Fig. 7f, k, l), which represent episodes of wetting and drying on stable surfaces that have been disturbed subsequently, but microfauna galleries are absent.

Numerical chronology

We dated the deposits using radiocarbon (¹⁴C) and single-grain OSL techniques. Most of the charcoal samples are isolated fragments, which decrease in abundance with depth, but nine samples were collected from *in situ* hearths in the northwest squares (Extended Data Fig. 5a). Charcoal was pretreated using acid–base–acid or acid–base

wet-oxidation procedures (the latter preferred for charcoal older than around 20 kyr^{32,33} and the ¹⁴C content measured by accelerator mass spectrometry (see Methods). The ¹⁴C ages of 22 charcoal samples (15 from the northwest squares) increase progressively to around 34 calibrated kyr before present (BP) at a depth of approximately 1.6 m, but some isolated fragments have stratigraphically inconsistent ages (Extended Data Fig. 8g). We attribute these anomalies to small-scale mixing of the deposits through post-depositional movement of charcoal fragments and digging of hearth pits.

OSL dating gives an estimate of the time since mineral grains were last exposed to sunlight³⁴. We applied this method to individual grains of quartz^{35,36} from 56 samples (44 from the northwest squares), including the measurement of four samples in two separate laboratories

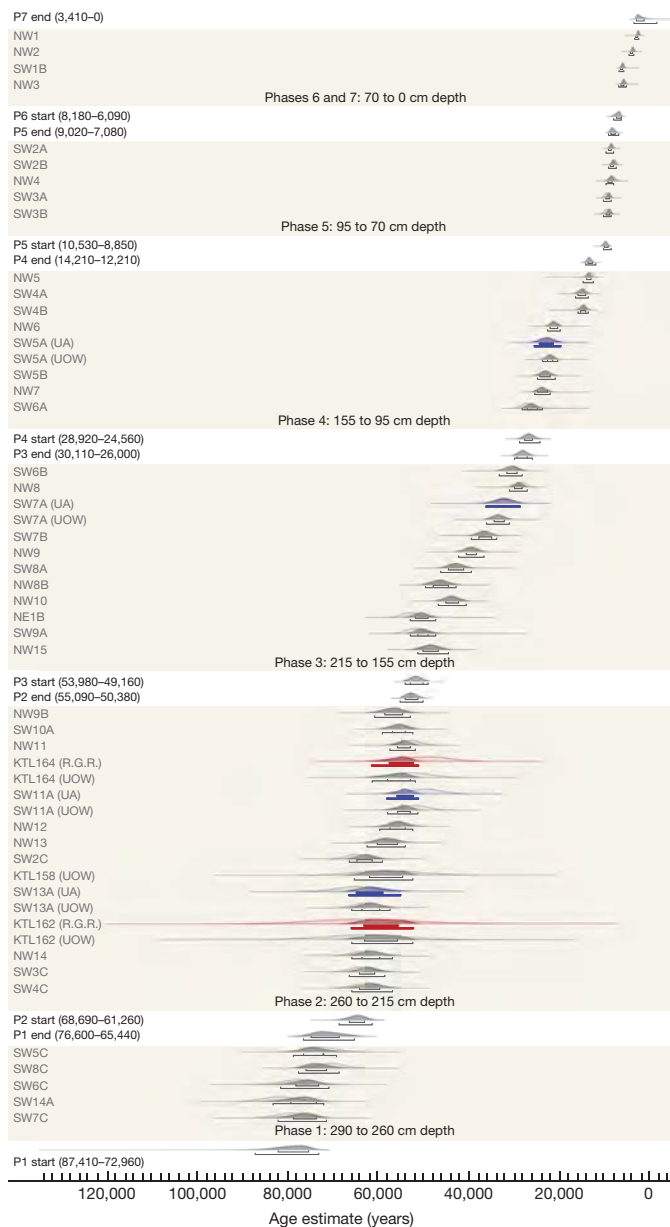


Figure 3 | Bayesian model of the single-grain OSL ages. Ages have been modelled in OxCal version 4.2. Only random errors are included. Pale probability distributions represent the unmodelled ages (likelihoods) and dark grey distributions represent the modelled ages (posterior probabilities) obtained in this study at the University of Wollongong (UOW). Blue distributions represent the ages obtained at the University of Adelaide (UA) for the four replicate samples in this study, while those in red (labelled R.G.R.) represent the two single-grain OSL ages reported in ref. 16. The two brackets beneath the distributions represent the 68.2% and 95.4% probability ranges. Start and end boundary ages have been modelled for each of the phases, with the age ranges (95.4% confidence interval, random-only errors) given in years and rounded off to the closest decade.

(Z.J. and L.J.A.) and four samples collected by R.G.R. in 1989 (KTL158, 162, 164 and 165)¹³. Many of the equivalent-dose distributions include some grains with smaller values than those of the majority of grains (Extended Data Fig. 9), which we interpret as evidence of small-scale disturbance of the deposit; some of the OSL samples were collected in 5-cm-diameter tubes, which will also result in some time-averaging (approximately 1,250 years at an average sedimentation rate of about 4 cm kyr⁻¹; see Supplementary Information). The OSL ages show a general pattern of increasing age with depth (Fig. 3 and Extended Data Fig. 8c–f), with consistent estimates obtained for both the replicate

and 1989 samples (Extended Data Fig. 10). The ages are also in good agreement with the ¹⁴C chronology (Extended Data Fig. 8g). Both chronologies support previous inferences^{16,22,30}, and the additional lines of evidence presented above, for limited post-depositional disturbance of the Pleistocene deposits and vertical displacement of associated artefacts.

We developed a Bayesian model based on the OSL chronology (Fig. 3) to estimate the start and end ages for the three dense bands of artefacts. The lowest dense band—the zone of first occupation—has modelled mean start and end ages of 65.0 ± (3.7, 5.7) and 52.7 ± (2.4, 4.3) kyr, respectively; the first and second error terms are the modelled age uncertainties at 95.4% probability, excluding and including the total systematic error, respectively (see Supplementary Information). These ages give a mean sediment accumulation rate of 4.1 ± 0.8 cm kyr⁻¹ for the lowest dense band. The middle dense band has modelled start and end ages of 26.7 ± (2.2, 2.8) and 13.2 ± (1.0, 1.3) kyr, corresponding to a mean accumulation rate of 4.4 ± 0.4 cm kyr⁻¹, and the upper dense band has a modelled start age of 7.1 ± (1.0, 1.1) kyr. This new chronology confirms the stratigraphic integrity of Australia's oldest known archaeological site and extends the timing of first occupation to around 65 ka, with more precise ages than those that have been obtained previously^{13,15,16}; the total age uncertainties are only 3–4 kyr (68.2% confidence interval) for the OSL samples associated with the lowest dense band of artefacts.

Discussion and implications

The new excavations have yielded a much larger and more diverse artefact assemblage than those reported previously^{13,22}, with more than 10,000 artefacts recovered *in situ* from the zone of first occupation. The improved chronological resolution for the site allows firmer conclusions to be drawn about the global significance of the earliest artefacts. The first occupants used elaborate lithic technology, ochre 'crayons' and other pigments—including one of the oldest known examples in the world of the use of reflective (micaceous) pigment (Fig. 2i, k–m). They also collected and processed plant foods, as revealed by macrofossils and artefact residues. Artefacts in the lowest dense band show traces of Australia's earliest evidence of seed grinding and pigment processing, together with the world's oldest known edge-ground hatchets^{37,38} (Fig. 2a).

The settlement of Madjedbebe around 65 ka (conservatively 59.3 ka, calculated as 65.0 ka minus the age uncertainty of 5.7 kyr at 95.4% probability) sets a new minimum age for the human colonization of Australia and the dispersal of modern humans out of Africa and across south Asia. The final stages of this journey took place at a time of lower sea level, when northern Australia was cooler and wetter. Our chronology places people in Australia more than 20 kyr before continent-wide extinction of the megafauna^{9–11} and supports an age of more than 60 kyr for the incorporation of Neanderthal and Denisovan DNA into the modern human genome^{1–7}. It also extends the period of overlap of modern humans and *Homo floresiensis* in eastern Indonesia to at least 15 kyr (ref. 39) and, potentially, with other archaic hominins—such as *Homo erectus*⁴⁰—in southeast Asia and Australasia.

Online Content Methods, along with any additional Extended Data display items and Source Data, are available in the online version of the paper; references unique to these sections appear only in the online paper.

Received 30 November 2016; accepted 19 May 2017.

1. Mallick, S. *et al.* The Simons Genome Diversity Project: 300 genomes from 142 diverse populations. *Nature* **538**, 201–206 (2016).
2. Malaspinas, A.-S. *et al.* A genomic history of Aboriginal Australia. *Nature* **538**, 207–214 (2016).
3. Pagani, L. *et al.* Genomic analyses inform on migration events during the peopling of Eurasia. *Nature* **538**, 238–242 (2016).
4. Reich, D. *et al.* Genetic history of an archaic hominin group from Denisova Cave in Siberia. *Nature* **468**, 1053–1060 (2010).
5. Sankararaman, S., Patterson, N., Li, H., Pääbo, S. & Reich, D. The date of interbreeding between Neandertals and modern humans. *PLoS Genet.* **8**, e1002947 (2012).

6. Fu, Q. *et al.* Genome sequence of a 45,000-year-old modern human from western Siberia. *Nature* **514**, 445–449 (2014).
7. Kuhlwilm, M. *et al.* Ancient gene flow from early modern humans into Eastern Neanderthals. *Nature* **530**, 429–433 (2016).
8. Bird, M. I. *et al.* Humans, megafauna and environmental change in tropical Australia. *J. Quat. Sci.* **28**, 439–452 (2013).
9. Saltré, F. *et al.* Climate change not to blame for late Quaternary megafauna extinctions in Australia. *Nat. Commun.* **7**, 10511 (2016).
10. Johnson, C. N. *et al.* What caused extinction of the Pleistocene megafauna of Sahul? *Proc. R. Soc. B* **283**, 20152399 (2016).
11. van der Kaars, S. *et al.* Humans rather than climate the primary cause of Pleistocene megafaunal extinction in Australia. *Nat. Commun.* **8**, 14142 (2017).
12. Hamm, G. *et al.* Cultural innovation and megafauna interaction in the early settlement of arid Australia. *Nature* **539**, 280–283 (2016).
13. Roberts, R. G., Jones, R. & Smith, M. A. Thermoluminescence dating of a 50,000-year-old human occupation site in northern Australia. *Nature* **345**, 153–156 (1990).
14. Roberts, R. G. *et al.* The human colonisation of Australia: optical dates of 53,000 and 60,000 years bracket human arrival at Deaf Adder Gorge, Northern Territory. *Quat. Sci. Rev.* **13**, 575–583 (1994).
15. Roberts, R. G. & Jones, R. Luminescence dating of sediments: new light on the human colonisation of Australia. *Aust. Aborig. Stud.* **1994**, 2–17 (1994).
16. Roberts, R. G. *et al.* Single-aliquot and single-grain optical dating confirm thermoluminescence age estimates at Malakunanja II rockshelter in northern Australia. *Anc. TL* **16**, 19–24 (1998).
17. Turney, C. S. M. *et al.* Early human occupation at Devil's Lair, southwestern Australia 50,000 years ago. *Quat. Res.* **55**, 3–13 (2001).
18. Bowler, J. M. *et al.* New ages for human occupation and climatic change at Lake Mungo, Australia. *Nature* **421**, 837–840 (2003).
19. O'Connell, J. F. & Allen, J. Dating the colonization of Sahul (Pleistocene Australia–New Guinea): a review of recent research. *J. Archaeol. Sci.* **31**, 835–853 (2004).
20. Allen, J. & O'Connell, J. F. Both half right: updating the evidence for dating first human arrivals in Sahul. *Aust. Archaeol.* **79**, 86–108 (2014).
21. O'Connell, J. F. & Allen, J. The process, biotic impact, and global implications of the human colonization of Sahul about 47,000 years ago. *J. Archaeol. Sci.* **56**, 73–84 (2015).
22. Clarkson, C. *et al.* The archaeology, chronology and stratigraphy of Madjedbebe (Malakunanja II): a site in northern Australia with early occupation. *J. Hum. Evol.* **83**, 46–64 (2015).
23. Veth, P. *et al.* Early human occupation of a maritime desert, Barrow Island, north-west Australia. *Quat. Sci. Rev.* **168**, 19–29 (2017).
24. Kamminga, J. & Allen, H. *Alligator Rivers Environmental Fact Finding Study: Report of the Archaeological Survey* (Australian Government, Canberra, 1973).
25. Roberts, R. G., Jones, R. & Smith, M. A. Stratigraphy and statistics at Malakunanja II: reply to Hiscock. *Archaeol. Ocean.* **25**, 125–129 (1990).
26. Hiscock, P. How old are the artefacts at Malakunanja II? *Archaeol. Ocean.* **25**, 122–124 (1990).
27. Bowdler, S. 50,000 year-old site in Australia—is it really that old? *Aust. Archaeol.* **31**, 93 (1990).
28. O'Connell, J. F. & Allen, J. When did humans first arrive in greater Australia and why is it important to know? *Evol. Anthropol.* **6**, 132–146 (1998).
29. Jones, R. Dating the human colonization of Australia: radiocarbon and luminescence revolutions. *Proc. Br. Acad.* **99**, 37–65 (1999).
30. Roberts, R. G. & Jones, R. in *Humanity from African Naissance to Coming Millennia: Colloquia in Human Biology and Palaeoanthropology* (eds Tobias, P. V., Raath, M. A., Moggi-Cecchi, J. & Doyle, G. A.) 239–248 (Firenze Univ. Press & Witwatersrand Univ. Press, 2001).
31. Marwick, B., Hayes, E., Clarkson, C. & Fullagar, R. Movement of lithics by trampling: an experiment in the Madjedbebe sediments, northern Australia. *J. Archaeol. Sci.* **79**, 73–85 (2017).
32. Bird, M. I. *et al.* Radiocarbon dating of “old” charcoal using a wet oxidation, stepped-combustion procedure. *Radiocarbon* **41**, 127–140 (1999).
33. Bird, M. I. *et al.* The efficiency of charcoal decontamination for radiocarbon dating by three pre-treatments — ABOX, ABA and hypy. *Quat. Geochronol.* **22**, 25–32 (2014).
34. Huntley, D. J., Godfrey-Smith, D. I. & Thewalt, M. L. W. Optical dating of sediments. *Nature* **313**, 105–107 (1985).
35. Jacobs, Z. & Roberts, R. G. Advances in optically stimulated luminescence dating of individual grains of quartz from archeological deposits. *Evol. Anthropol.* **16**, 210–223 (2007).
36. Roberts, R. G. *et al.* Optical dating in archaeology: thirty years in retrospect and grand challenges for the future. *J. Archaeol. Sci.* **56**, 41–60 (2015).
37. Geneste, J.-M. *et al.* Earliest evidence for ground-edge axes: 35,400±410 cal BP from Jawoyn Country, Arnhem Land. *Aust. Archaeol.* **71**, 66–69 (2010).
38. Hiscock, P., O'Connor, S., Balme, J. & Maloney, T. World's earliest ground-edge axe production coincides with human colonisation of Australia. *Aust. Archaeol.* **82**, 2–11 (2016).
39. Sutikna, T. *et al.* Revised stratigraphy and chronology for *Homo floresiensis* at Liang Bua in Indonesia. *Nature* **532**, 366–369 (2016).
40. Mondal, M. *et al.* Genomic analysis of Andamanese provides insights into ancient human migration into Asia and adaptation. *Nat. Genet.* **48**, 1066–1070 (2016).

Supplementary Information is available in the online version of the paper.

Acknowledgements The authors are grateful to the custodians of Madjedbebe, the Mirarr Senior Traditional Owners (Y. Margarula and M. Nango) and our research partners (Gundjeihmi Aboriginal Corporation) for permission to carry out this research and publish this paper. We are also grateful to J. O'Brien and D. Vadivelloo for assistance in the field. This research was funded through Australian Research Council grants and fellowships to C.C., B.M., L.W., R.F., M.Sm. (DP110102864), B.M. (FT140100101), Z.J. (DP1092843, FT150100138), R.G.R. (FL130100116), T.Ma. (DE150101597) and L.J.A. (FT130100195), and through Australian Postgraduate Awards to X.C., E.H., S.A.F. and K.L. B.M. was also supported by a DAAD Fellowship (A/14/01370), a UW-UQ Trans-Pacific Fellowship, and UW Royalty Research Fellowship (65-4630). S.A.F. was also supported by an AINSE Postgraduate Research Award (11877) and a Wenner Gren Dissertation Fieldwork Grant (Gr.9260). Radiocarbon analyses were partly funded by Australian Institute of Nuclear Science and Engineering grants 13/003 and 15/001 to C.C., X.C., S.A.F. and K.N. We acknowledge financial support from the Australian Government's National Collaborative Research Infrastructure Strategy (NCRIS) for the Centre for Accelerator Science at the Australian Nuclear Science and Technology Organisation. A L'Oréal Australia For Women in Science Fellowship to Z.J. supported the re-dating of the original sediment samples. Part of this work was undertaken on the powder diffraction beamline at the Australian Synchrotron. We thank E. Grey, R. MacPhail, S. Mentzer, C. Miller, M. Svob, and X. Villagran for assistance with geoarchaeological analysis, T. Lachlan and Y. Jafari for help with OSL dating and related illustrations, and C. Matheson and J. Field for assistance with residue analysis.

Author Contributions C.C., B.M., R.F., L.W. and M.Sm. obtained funding and conducted the excavation. Z.J. performed the OSL dating and Bayesian modelling. L.J.A. conducted the blind OSL dating study. Q.H. conducted ¹⁴C dating. C.C. and B.M. analysed the stone artefacts. J.M. performed the refitting. B.M. and K.L. conducted geoarchaeological investigations. T.Ma. performed vertebrate faunal identification. D.C. analysed the ground ochre assemblage. R.F. and E.H. analysed the stone artefact usewear and residues. S.A.F., X.C. and A.F. analysed the archaeobotanical assemblage. K.C. performed microscopy on ART9 mica. K.N. made the map in Fig. 1 and performed analysis of marine transgression for the study region. J.H. conducted the pXRF analyses. J.H. and H.E.A.B. collected and analysed the pigment samples using synchrotron powder XRD. J.S. summarized palaeoclimate data for northern Australia. L.L., M.Sa., M.P., G.P. and T.Mu. performed isotopic and sediment analyses. C.P. performed skeletal analysis and assisted with in-field excavation processing. C.C., Z.J., B.M. and R.G.R. wrote the main text with specialist contributions from other authors.

Author Information Reprints and permissions information is available at www.nature.com/reprints. The authors declare no competing financial interests. Readers are welcome to comment on the online version of the paper. Publisher's note: Springer Nature remains neutral with regard to jurisdictional claims in published maps and institutional affiliations. Correspondence and requests for materials should be addressed to C.C. (c.clarkson@uq.edu.au) and Z.J. (zenobia@uow.edu.au).

Reviewer Information *Nature* thanks R. Dennell, C. Marean, E. J. Rhodes and J.-L. Schwenninger for their contribution to the peer review of this work.

METHODS

Excavation methods. Excavation took place in 1×1 m squares in 2–5 cm spits within stratigraphic layers. Twenty 1×1 m squares were excavated adjacent to and enclosing the original 1973 and 1989 excavations (Fig. 1c). Eight squares were dug to 2.75 m depth (B1, C1–3, D1–3, E2), while five squares were dug to 3 m depth (B5, B6, C4–6) and two squares (B2, B3) to 3.4 m depth in 2012 and 2015. One square was dug to 4.3 m depth in 1989 (B4), with the remaining squares discontinued at 1.3–1.5 m depth to maintain baulks and site stability (E1, E3, E4, D4). The deeper squares were excavated in 72 spits, with spits averaging 4–5 cm deep in the upper deposit where dense shell midden was present, and averaging 2.5 cm deep from 2–3 m depth. All artefacts larger than 2 cm were piece-plotted *in situ* with a total station and bagged separately with a unique identifying number. Artefacts were identified during the excavation, where possible, and coded by type (lithic, haematite, bone, human bone, axe, axe flake, grinding stone, and so on). Sedimentary features (abbreviated as SF) were outlined and contours plotted with a total station. The latter included human burial cuts, hearths, pits and intrusive features such as root casts, burrows and postholes. All sediments were passed through nested 3 and 7 mm mesh sieves and a 100 g sediment sample was retained from each spit. Munsell colour and pH values were obtained for each spit and all sieve residue was bagged and transported to the University of Queensland archaeology laboratories for sorting. Sediments were extensively sampled for pollen, geoarchaeology and phytoliths, and blocks were taken from the walls for soil micromorphology. Bulk sediment samples were also collected from two columns (see 'Archaeobotanical analysis methods'). The site was backfilled with the original sediment and all human bone was reinterred after analysis at the completion of the excavation in 2016.

Artefact analysis methods. All stone artefacts were counted and weighed according to raw material, artefact type (core, flake, retouched flake, flaked piece) and typology. A complete list is provided in the Supplementary Information for select squares. The number of artefacts per spit was divided by litres excavated to calculate artefact frequencies (density per spit). Plotted artefacts were left unwashed. Heat-affected artefacts were identified by high lustre, crenated fracture, crazing, irregular heat-exfoliation surfaces and pot-lid scarring. Ground and retouched artefacts were initially inspected under low magnification and selected items were analysed for functional traces, including usewear and residues. Haematite pieces were classified as ground and unground, and counted and weighed. Ground haematite was analysed in detail for the number of ground facets, quality and colour, and selected pieces were further analysed under high magnification for usewear and residues.

Radiocarbon dating of charcoal. Charcoal samples were submitted for analysis to two different radiocarbon laboratories—Waikato (Wk) and ANSTO (OZ) in New Zealand and Australia, respectively. Samples were collected during the 2012 and 2015 excavation seasons and were carefully recorded and plotted using a total station. The samples were collected from a number of different squares (B3–E3, C4, C5 and E4). The relevant squares are shaded in grey in Extended Data Fig. 8a and the sample codes, contexts and chemical pretreatments are provided in Supplementary Table 2. Samples were taken from depths of between 8 cm and 200 cm below the ground surface.

Samples submitted to Waikato were first physically cleaned of any adhering sediment and loose material, and then crushed. This was followed by an acid–base–acid (ABA) chemical pretreatment, in which samples were washed in hot HCl, rinsed, treated with NaOH and rinsed again, and then treated with hot HCl, rinsed and dried. The pretreated samples were then combusted to CO₂ by oxidation at 800 °C using CuO. The CO₂ was purified in the presence of silver wire to absorb any SO_x and NO_x produced. The CO₂ was then reduced to graphite with H₂ at 550 °C using an iron catalyst. The pressed graphite targets were sent to the Keck Radiocarbon Dating Laboratory at the University of California, Irvine and the Center for Applied Isotope Studies, University of Georgia for accelerator mass spectrometry (AMS) measurements.

Samples submitted to ANSTO were pretreated using either the ABA procedure (for samples younger than around 20 kyr) or the acid–base wet-oxidation (ABOx) procedure (for samples older than around 20 kyr). The ABOx pretreatment included washes in acid (2 M HCl at 60 °C for 2 h), alkali (1% NaOH at 60 °C for 1 h) and acid (0.1 M K₂Cr₂O₇ at 60 °C for 24 h), with Milli-Q water rinses between each step or until the solutions were clear. The pretreated samples were oven-dried at 60 °C for two days before being combusted to CO₂ using the sealed-tube technique, after which the CO₂ was reduced to graphite using the H₂/Fe method⁴¹. A portion of graphite was used to determine the $\delta^{13}\text{C}$ value, for the isotopic fractionation correction, using a Vario Microcube elemental analyser and an IsoPrime isotope-ratio mass spectrometer. AMS measurements of ¹⁴C content were carried out using the STAR facility at ANSTO⁴².

The ¹⁴C ages and related information, including age calibration performed using the SHCal13 calibration curve⁴³ and the OxCal version 4.2 program⁴⁴, are provided in Supplementary Table 2.

Single-grain OSL dating. OSL dating provides a means of determining the burial ages for sediments and associated artefacts and fossils^{34–36}. The time that has elapsed since mineral grains were last exposed to sunlight can be determined from measurements of the OSL signal—from which the equivalent dose (D_e) is estimated—together with determinations of the radioactivity of the sample and the material surrounding it to a distance of around 30 cm (the environmental dose rate). Fifty-two samples were collected for OSL dating from the upper 2.9 m of deposit during the 2012 and 2015 excavation seasons and from four different excavated profiles (Extended Data Fig. 8). Individual grains of quartz (180–212 μm diameter) were obtained from the samples and measured for their D_e values, using standard procedures and tests (for example, ref. 45). To obtain an estimate of the environmental dose rate for each sample, an internal alpha dose rate of 0.032 ± 0.010 Gy kyr⁻¹ was assumed and beta dose rates were measured using a GM-25-5 beta counter⁴⁶ and the procedures described in ref. 47. Gamma dose rates were measured directly by *in situ* gamma spectrometry, and cosmic-ray dose rates were calculated using published equations^{48,49}. Beta dose rates were corrected for grain-size attenuation and the beta, gamma and cosmic-ray dose rates were adjusted using a water content of $5 \pm 2\%$ (68.2% confidence interval) to obtain estimates of the total environmental dose rate. The burial time of the grains in calendar years before present is calculated as the D_e divided by the environmental dose rate. Age uncertainties are given at the 68.2% confidence level and were estimated by combining, in quadrature, all known and estimated sources of random and systematic error. Details of the preparation, measurement and analysis of single grains, the determination of D_e values and dose rates, and the resulting OSL age estimates are provided in the Supplementary Information.

Independent estimates of single-grain D_e values and dose rates were obtained for four samples (SW13A, 11A, 7A and 5A) at the University of Adelaide by L.J.A. In addition, the single-grain D_e values for four samples reported in the original thermoluminescence dating study of Madjedbebe¹³ (KTL158, 162, 164 and 165) were re-measured and their environmental dose rates re-calculated using the same procedures as for the other samples in this study. Details are given in the Supplementary Information and the results are shown in Extended Data Fig. 10.

Single-grain OSL ages were put into a Bayesian statistical model on the OxCal platform (OxCal version 4.2.4)^{44,50} (Fig. 3). The samples measured from the NE sample column (Extended Data Fig. 8e) were not included in the model, because there is a slope from the back of the site to the front and the depth offset with the samples collected from the SW and NW sequences is not known with sufficient precision. The model included the two single-grain ages obtained for KTL162 and KTL164 (ref. 16)—re-calculated here using updated dose rate information (Extended Data Fig. 10f)—and the four replicate ages for SW13A, 11A, 7A and 5A obtained independently by L.J.A.

Each OSL age was input as a C_date in calendar years before AD 1950 with an associated uncertainty (the standard error of the mean). Only the random errors (listed in parentheses in Supplementary Table 5) were included in the model, because OSL ages do not have fully independent uncertainties^{51,52}. As prior information, we used the depths associated with changes in artefact technology and stone tool raw materials, and the peaks and dips in artefact concentration (Extended Data Fig. 2). The entire sequence was modelled as a series of seven phases (Fig. 3), assuming that the measured ages are unordered and uniformly distributed within a phase, and the stratigraphically lowest phase is older than those above. A 'boundary' was placed at the start and end of each phase. A General *t*-type Outlier Model⁵³ was used to assess the likelihood of each age being consistent with the fitted model. Each age was assigned a prior outlier probability of 5%. Further details of the Bayesian modelling, together with the modelled OSL data and model code, are provided in the Supplementary Information.

Archaeobotanical analysis methods. Sixty litres of sediment for each excavation unit (approximately 100% of a 4 cm spit) was collected from two columns (C3/1–27 and C2/28–57; C6/1–15 and C5/16–72) as a bulk sediment sample, allowing a continuous sequence of archaeobotanical recovery through the deposit. In addition, all hearths and other features were collected in their entirety for flotation. The recovery of archaeobotanical material at Madjedbebe was aided by the use of a cascading 'Ankara-style' flotation tank^{54,55}, which facilitated swift and comprehensive processing. Archaeobotanical samples were sorted and weighed. The wood charcoal was separated from the other macrobotanical remains, both examined separately by X.C. and S.A.F. The wood charcoal was taxonomically identified following the criteria of the International Association of Wood Anatomists and with the assistance of a comprehensive wood reference collection for the region collected by X.C. with the assistance of the George Brown Darwin Botanic Gardens^{56,57}. Sampling protocols were in accordance with those outlined by Asouti and Austin⁵⁸. The other macrobotanical remains were sorted using standard archaeobotanical procedures. High-powered light microscopy and scanning electron microscope imaging was used to compare the anatomical and morphological features of the archaeological specimens to modern reference material from the region (collected

by S.A.F. in conjunction with the Gundjeihmi Aboriginal Corporation, Mirarr traditional owners and the Northern Territory Herbarium). We used the criteria proposed by Fairbairn⁵⁹ and Hather^{60,61} to identify *Pandanus* sp. drupes and vegetative parenchyma, respectively.

Artefact associations and refitting. Refitting attempts were made on all plotted and 7-mm-sieve silcrete artefacts as well as all 3-mm-sieve silcrete artefacts from squares C2–C4 ($n = 778$). A traditional approach to refitting was combined with high resolution, objective measurements of artefact colour to determine potential matches between similarly coloured artefacts. This method used a portable, wireless colour scanner (NODE+ Chroma 2.1 by Variable Inc.) that communicates with handheld iOS and Android devices. An application program interface for each device was produced to allow the collection of identification-tied data, and a project-specific.net application that allowed transparent statistical analysis and colour grouping of data was also produced⁶². Refits were first attempted between all artefacts grouped by similar colour, and then across colour grades. Scans were restricted to a section of the lithic artefact where NODE+ either sits flush with the surface or on a slight concavity that rises to meet the aperture. This maintained a standard measurement distance during each scan. A minimum of three suitable scanning areas was identified on each artefact, with five scans taken from each sample area. Five scans were taken to minimize the potential of any human error during positioning of the device. For banded or variably coloured artefacts, each area of colour was treated as a separate sample area. Potential matching artefacts were analysed for similarity under 10 \times and 20 \times magnification using an Olympus SZX16 stereoscope with NIS Elements Advanced Research version 4, following the methodology outlined by Wilkins⁶³.

Granulometry. Hand-grab bulk samples were taken from squares B2, C4, and E2 at 5 cm intervals from the surface, dry sieved through a 2-mm screen and macroscopic organic materials were removed by hand. For each sample, three trials of five sub-samples were analysed with a Horiba LA-950 Laser Particle Size Analyser at the University of Washington, Department of Materials Science and Engineering, resulting in 15 measurements per sample.

Carbon isotopes. Hand-grab bulk samples were collected from square B2, following the procedure for granulometry. A 2 g sub-sample was then ground to a fine powder and treated with 2 M HCl for 24 h to remove inorganic carbon. The samples were then rinsed in de-ionized water, the water separated from the sediments using a centrifuge, and the samples dried at 60 °C for 24 h and then measured using a Costech Elemental Analyser on a Finnigan 253 Mass Spectrometer at the IsoLab in the University of Washington, Department of Earth and Space Sciences.

Micromorphology. Intact blocks of sediment were extracted from squares B2 and E2, and the hearth at C4/36A, by encasing the blocks in plaster bandages to ensure their integrity. The blocks were air-dried at 40 °C for seven days, then impregnated with Reichhold Polylyte polyester resin, styrene and hardened with methyl ethyl ketone peroxide using a ratio of 7:3:0.025. After curing for several weeks, thick sections were cut from the blocks with a diamond saw and sent to Spectrum Petrographics to prepare thin sections for microscopic analysis. Thin sections were analysed under different magnifications and different lights (plane polarized, cross-polarized and fluorescent) with stereo petrographic microscopes at the University of Tübingen and the University of Washington. Whole-slide scans were taken with a flat-bed document scanner.

Magnetic susceptibility. Magnetic susceptibility (χ) was measured at both low (460 Hz) and high (4,600 Hz) frequencies for the stratigraphic units within the sedimentary sequence in squares B2 and C3. As observed in other sandstone rock shelters^{64,65}, samples are weakly magnetic in the culturally sterile layers. The lower susceptibility values measured in the deepest deposits were often close to the sensitivity limit of the Bartington Instrument MS2B sensor, resulting in a higher percentage loss of the low-frequency measurements (χ fd%), with averages of around 16%; these data were discarded.

Pigment characterization. *X-ray fluorescence.* Non-invasive elemental characterizations were undertaken to investigate the inorganic chemical composition of pigments. Data were collected using a Bruker S1 Titan 800 portable X-ray fluorescence (pXRF) instrument, equipped with a silicon drift detector, Rh target X-ray tube (maximum voltage 50 kV, default to 150 °C with ultralene window) and five-position motorized filter changer. Two beam phases were run sequentially, each collecting for 90 analytic seconds. Phase 1 parameters: 45 kV, 10.45 μ A with a filter (Ti 25 μ m, Al 300 μ m) in the beam path. Phase 2 parameters: 15 kV, 31.55 μ A without a filter. Spectra were collected on suitable artefact surfaces, where attenuation could be minimized or avoided⁶⁶. Relative abundance concentrations for 27 elements reported derive from the manufacturer's fundamental parameters calculation.

Synchrotron powder diffraction. Powder pigments were collected using a micro-drill, two from ART9 with an additional 75 samples taken from ochre nodules by milling the outside of the specimens and then drilling to a depth of around 5 mm

to sample their internal structure. Powders were homogenized (manually ground with mortar and pestle), placed into 0.3-mm-diameter borosilicate capillaries and mounted on the beamline. Diffraction data were collected at the Australian Synchrotron at a wavelength of 0.77412 Å, calibrated using a NIST SRM 660b, from 5–85° 2Theta, with a Mythen microstrip detector with an inherent step size of 0.002°, using two detector positions and a collection time of 5 min per position. Samples were rotated at around 1 Hz during data collection to ensure good powder averaging. Phase identifications of selected samples were undertaken using Panalytical Highscore with the ICDD PDF4 database.

Usewear and residues. All potential grinding stones and fragments ($n = 91$) from the 2012 excavations were examined for wear and residue traces. Stones were visually scanned under low and high magnification on the ground and unground surfaces, using stereo and metallographic microscopes with low-angled oblique light and vertical incident light sources, respectively. The unground surfaces were documented to evaluate residues and traces that might be linked to handling or anvil positioning during use, and to identify traces that mimic usewear, such as micro-fractures of quartz grains on non-used surfaces. The latter are probably caused by friction between sediment and artefacts, either during use or after discard and burial within the sediments. All complete, near-complete and broken edge-ground hatchets ($n = 10$), and a selection of flakes from edge-ground axe margins, were also examined under the same stereo and metallographic microscopes.

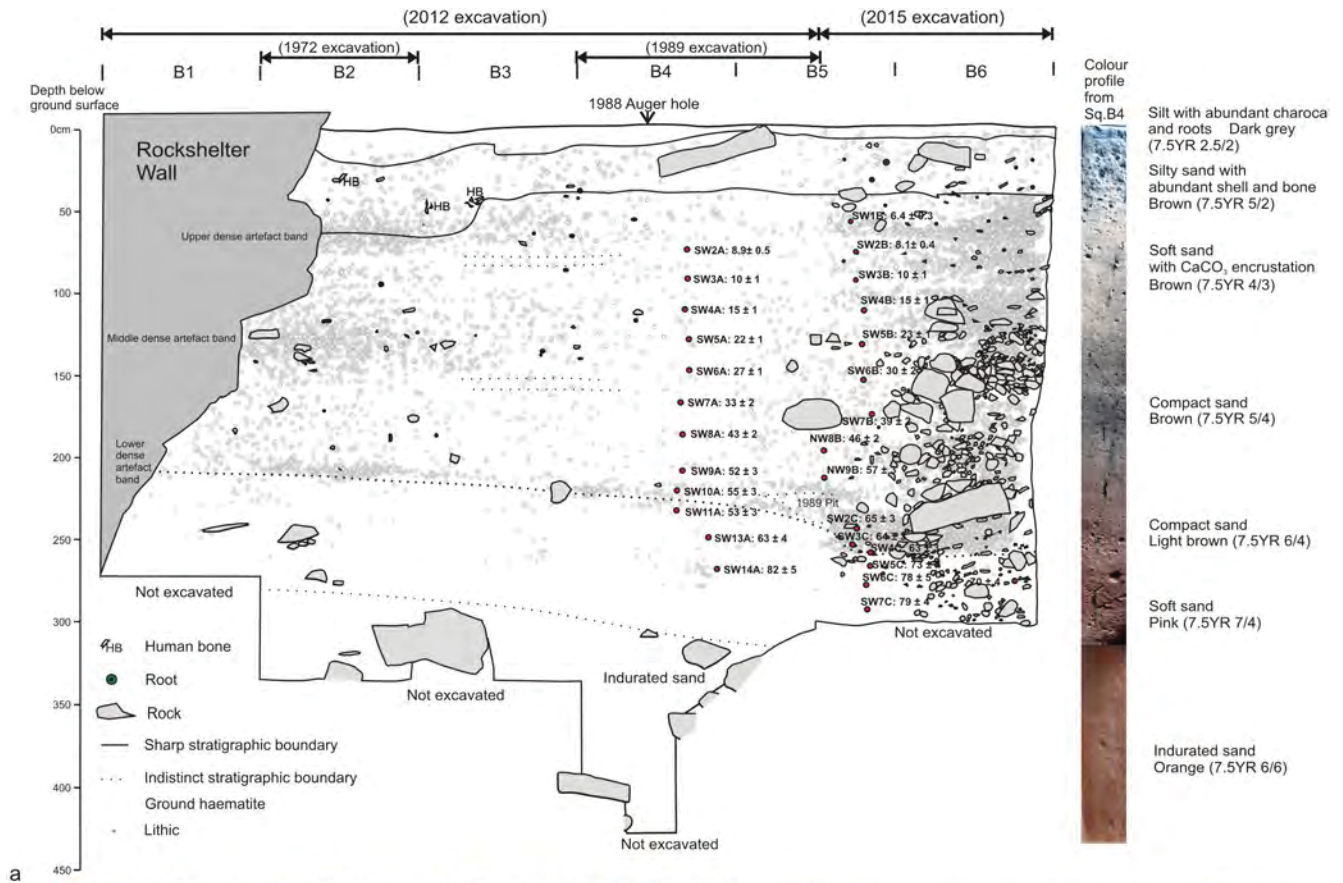
Residue distributions were documented across each of the tool surfaces and characterized using a range of techniques, following removal with a solvent mixture of water, ethanol and acetonitrile (up to 50 μ l extracted with an adjustable pipette). Residue extractions were characterized using: (1) high-magnification transmitted light microscopy and various biochemical stains to test for and distinguish plant and animal tissues; (2) absorbance spectroscopy and biochemical tests for the detection of protein, carbohydrates, fatty acids, starch and ferrous iron (see ref. 67 and Supplementary Information for specific methods for each test); and (3) gas chromatography mass spectrometry. A selection of grinding stones ($n = 12$) had additional residues removed by ultrasonication. Tools were completely or partially submerged in distilled water and ultrasonicated for 2 min. Density separation of the extracted residue mixtures isolated starch grains and other plant microfossils (phytoliths, raphides, pollen), when present.

Code availability. The computer code used to generate the Bayesian age model for the site is provided in full in the Supplementary Information, together with information about the program and version used. The R code used to analyse and visualize the geochronological and stone artefact data is archived online at <https://doi.org/10.6084/m9.figshare.4652536>.

Data availability. All elements necessary to allow interpretation and replication of results, including full datasets and detailed experimental procedures are provided in the Supplementary Information. All geochronological and stone artefact data files are archived online at <https://doi.org/10.6084/m9.figshare.4652536>. Archaeological material generated in this study will be kept in the Archaeology Laboratories of the University of Queensland until 2018. It will then be deposited in a Gundjeihmi Aboriginal Corporation keeping place. The material will be publicly accessible upon request with permission from Gundjeihmi Aboriginal Corporation and the corresponding author. Archaeological materials from the 1973 and 1989 excavations are stored in the Museum and Art Gallery of the Northern Territory and can be publicly accessed with permission from the museum director.

- Hua, Q. *et al.* Progress in radiocarbon target preparation at the Antares AMS Centre. *Radiocarbon* **43**, 275–282 (2001).
- Fink, D. *et al.* The ANTARES AMS facility at ANSTO. *Nucl. Instrum. Methods Phys. Res. B* **223–224**, 109–115 (2004).
- Hogg, A. G. *et al.* SHCal13 Southern Hemisphere calibration, 0–50,000 years cal BP. *Radiocarbon* **55**, 1889–1903 (2013).
- Bronk Ramsey, C. & Lee, S. Recent and planned developments of the program OxCal. *Radiocarbon* **55**, 720–730 (2013).
- Wood, R. *et al.* Towards an accurate and precise chronology for the colonization of Australia: the example of Riwil, Kimberley, Western Australia. *PLoS ONE* **11**, e0160123 (2016).
- Bøtter-Jensen, L. & Mejdahl, V. Assessment of beta dose-rate using a GM multicounter system. *Int. J. Rad. Appl. Instrum. D* **14**, 187–191 (1988).
- Jacobs, Z. & Roberts, R. G. An improved single grain OSL chronology for the sedimentary deposits from Diepkloof Rockshelter, Western Cape, South Africa. *J. Archaeol. Sci.* **63**, 175–192 (2015).
- Prescott, J. R. & Hutton, J. T. Cosmic ray contributions to dose rates for luminescence and ESR dating: large depths and long-term time variations. *Radiat. Meas.* **23**, 497–500 (1994).
- Smith, M. A., Prescott, J. R. & Head, M. J. Comparison of ¹⁴C and luminescence chronologies at Puritjarra rock shelter, central Australia. *Quat. Sci. Rev.* **16**, 299–320 (1997).
- Bronk Ramsey, C. Bayesian analysis of radiocarbon dates. *Radiocarbon* **51**, 337–360 (2009).

51. Rhodes, E. J. *et al.* Bayesian methods applied to the interpretation of multiple OSL dates: high precision sediment ages from Old Scatness Broch excavations, Shetland Isles. *Quat. Sci. Rev.* **22**, 1231–1244 (2003).
52. Galbraith, R. F. & Roberts, R. G. Statistical aspects of equivalent dose and error calculation and display in OSL dating: an overview and some recommendations. *Quat. Geochronol.* **11**, 1–27 (2012).
53. Bronk Ramsey, C. Dealing with outliers and offsets in radiocarbon dating. *Radiocarbon* **51**, 1023–1045 (2009).
54. French, D. H. An experiment in water-sieving. *Anatol. Stud.* **21**, 59–64 (1971).
55. Nesbitt, M. Plants and people in Ancient Anatolia. *Biblic. Archaeol.* **58**, 68–81 (1995).
56. Wheeler, E. A., Baas, P. & Gasson, P. E. IAWA list of microscopic features for hardwood identification. *IAWA Bull.* **10**, 219–332 (1989).
57. Richter, H. G., Grosser, D., Heinz, I. & Gasson, P. E. IAWA list of microscopic features for softwood identification. *IAWA J.* **25**, 1–70 (2004).
58. Asouti, E. & Austin, P. Reconstructing woodland vegetation and its exploitation by past societies, based on the analysis and interpretation of archaeological wood charcoal macro-remains. *Environ. Archaeol.* **10**, 1–18 (2005).
59. Summerhayes, G. R. *et al.* Human adaptation and plant use in highland New Guinea 49,000 to 44,000 years ago. *Science* **330**, 78–81 (2010).
60. Hather, J. G. in *Tropical Archaeobotany: Applications and New Developments* (ed. Hather, J. G.) 51–64 (Routledge, 1994).
61. Hather, J. G. *Archaeological Parenchyma* (Archetype Publications, 2000).
62. McNeil, J.-L., Marginson, A., Mackay, A. & Clarkson, C. Colour Signature Analysis: Using objective colour quantification techniques towards refitting lithic assemblages. 80th Annual Meeting of the Society for American Archaeology (2015).
63. Wilkins, J. R. *Prepared Core Technology at Kudu Koppie, South Africa and the Modern Human Behaviour Debate*. MA thesis, Univ. Calgary (2008).
64. Lowe, K. M. *et al.* Using soil magnetic properties to determine the onset of Pleistocene human settlement at Gledswood Shelter 1, northern Australia. *Geoarchaeology* **31**, 211–228 (2016).
65. Lowe, K. M., Mentzer, S. M., Wallis, L. A. & Shulmeister, J. A multi-proxy study of anthropogenic sedimentation and human occupation of Gledswood Shelter 1: exploring an interior sandstone rockshelter in Northern Australia. *Archaeol. Anthropol. Sci.* <http://dx.doi.org/10.1007/s12520-016-0354-8> (2016).
66. Huntley, J. Taphonomy or paint recipe? *In situ* portable X-ray fluorescence analysis of two anthropomorphic motifs from the Woronora plateau, New South Wales. *Aust. Archaeol.* **75**, 78–94 (2012).
67. Fullagar, R. *et al.* Evidence for Pleistocene seed grinding at Lake Mungo, south-eastern Australia. *Archaeol. Oceania* **50**, 3–19 (2015).



a



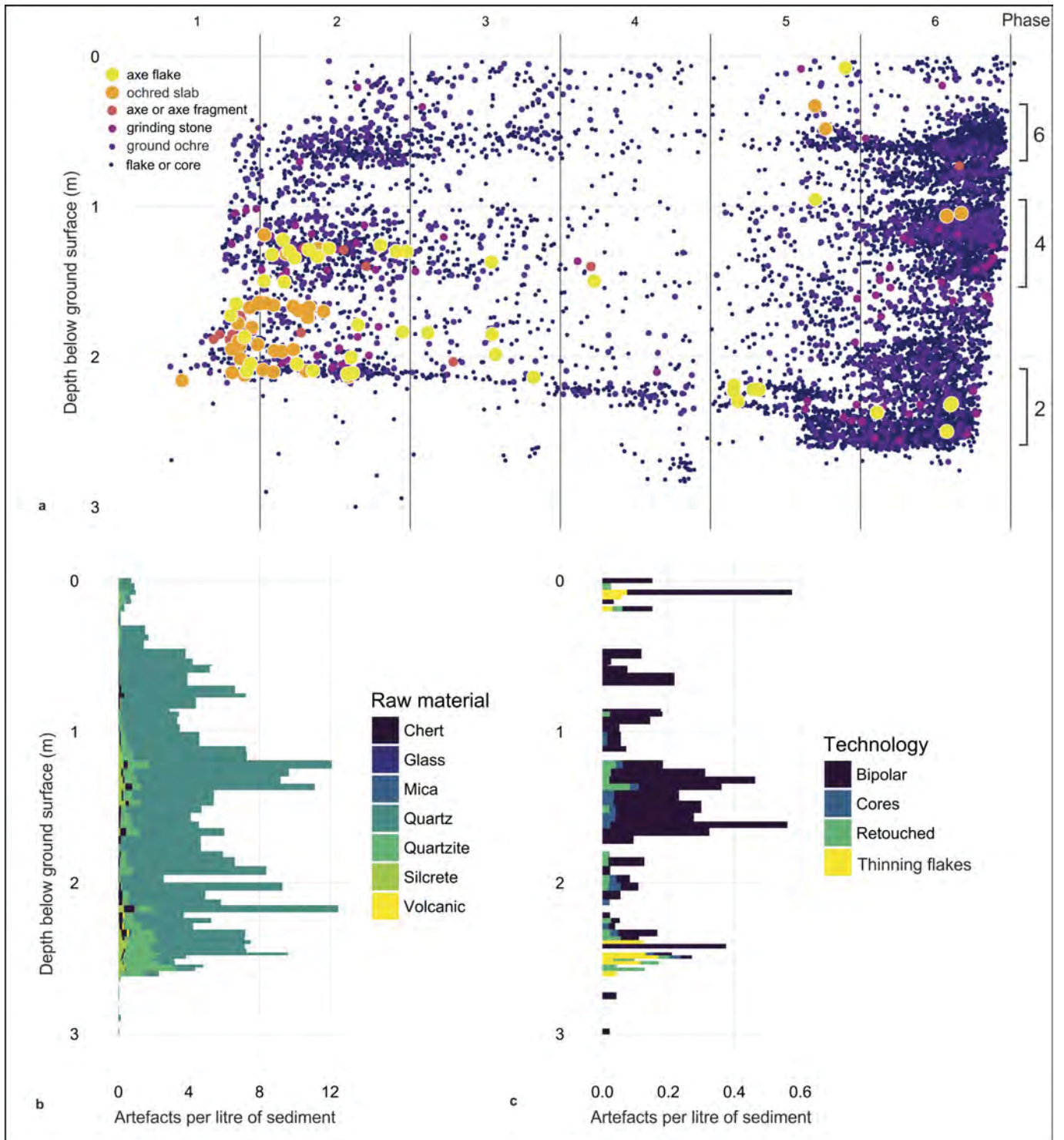
b



c

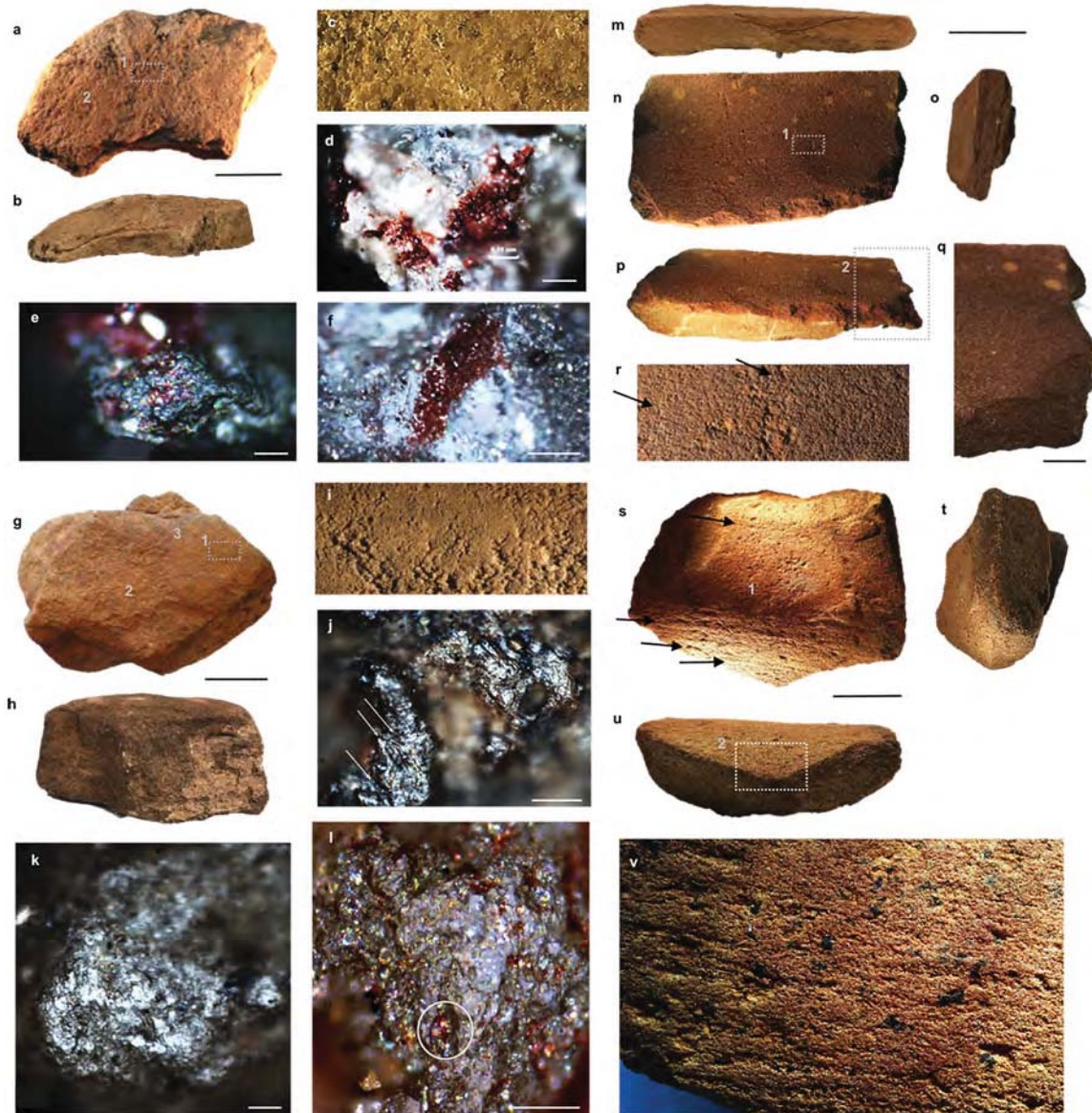
Extended Data Figure 1 | Madjedbebe rock shelter. a, Section drawing of the southwest profile wall, showing major stratigraphic divisions and sediment descriptions, and the location of the 1973, 1989, 2012 and 2015

excavation trenches. Light grey dots show plotted artefacts. b, Photograph of the site during the 2015 excavation. c, Detail of the site ground surface during ground penetrating radar survey, before the 2012 excavation.



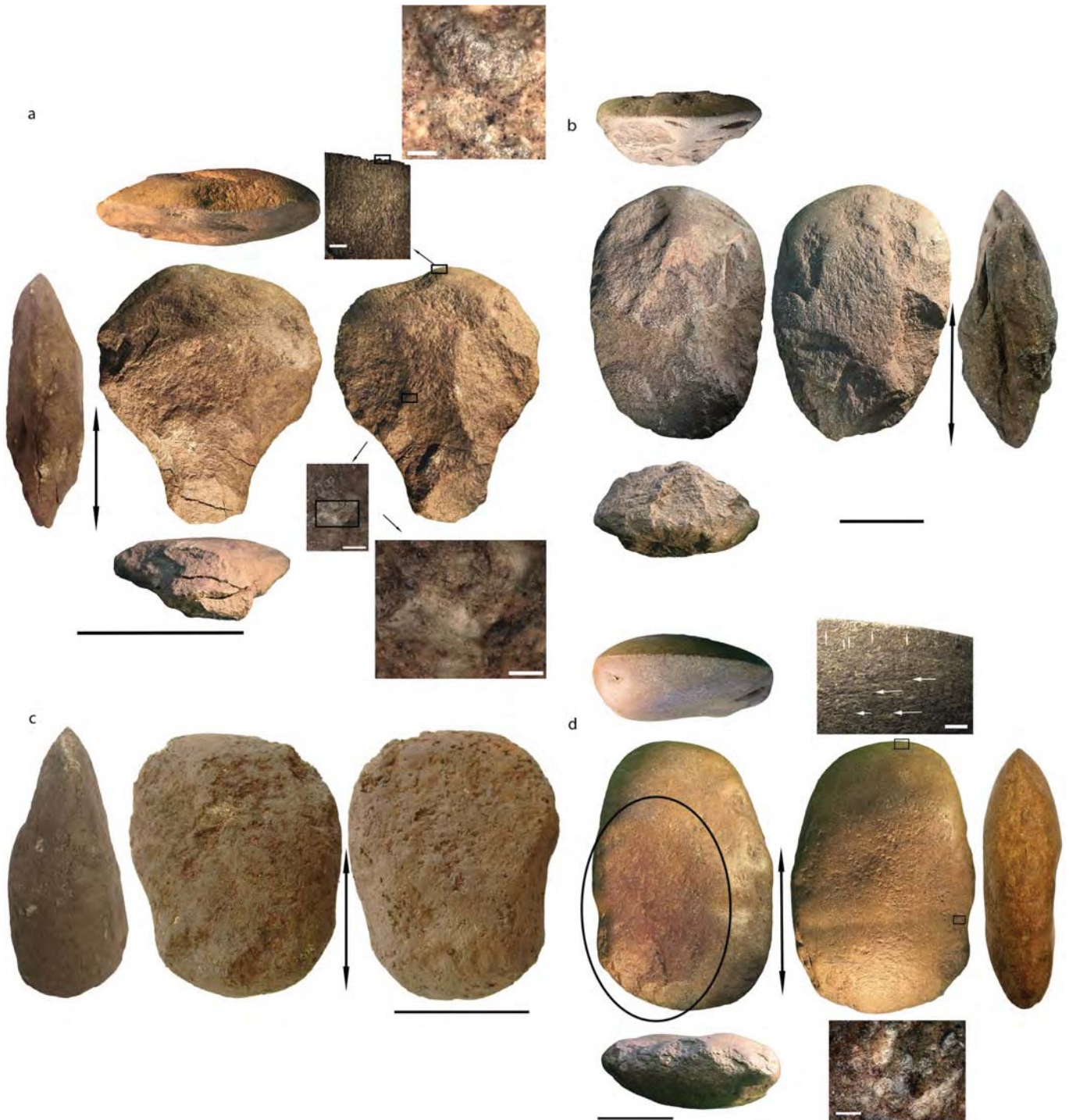
Extended Data Figure 2 | Plot of artefact densities and assemblage composition as a function of depth below ground surface. **a**, Plot of density of artefacts found during the 2012 and 2015 excavation seasons in squares from the C and B rows. Artefacts are shown by type (axe flake, ochred slab, axe or axe fragment, grinding stone, ground ochre, and flake or core) superimposed on the southwest profile wall (Extended Data Fig. 1).

Phases represent the three dense artefact bands (see text and Supplementary Information). **b**, Plot of artefact density and raw material type with depth, based on plotted artefacts and residue found in the 7-mm sieves for square B6. **c**, Plot of technological changes with depth, based on plotted artefacts and residue found in the 7-mm sieves for square B6.



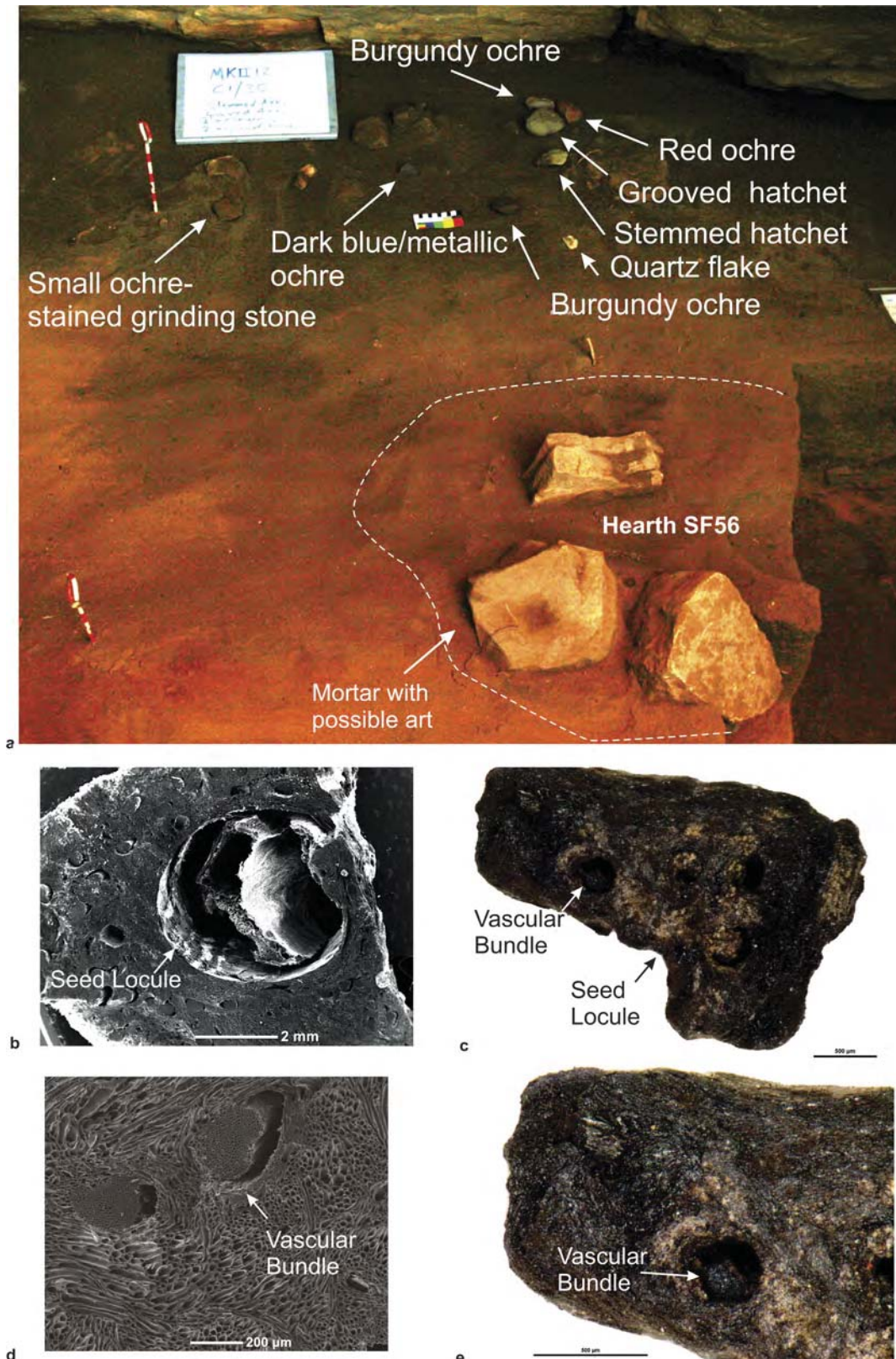
Extended Data Figure 3 | Grinding stones, residues and usewear of specimens collected from phase 2 at Madjedbebe. **a–f**, Specimen UPGS36 (from 2012 spit 44) and residues from processing of red pigment. **a**, Ground surface. Scale bar, 2 cm. **b**, Plan view. **c**, Ground surface at low magnification (location 1 in **a**) showing levelled grains. **d–f**, Red pigment residues at high magnification. **d**, Location 2 in **a**. Scale bar, 0.5 mm. **e**, **f**, Location 2 in **a**. Scale bars, 0.02 mm. **g–k**, Specimen GS39 (from 2012 spit 37) and usewear, used for processing of seeds. **g**, Ground surface. Scale bar, 4 cm. **h**, Plan view. **i**, Ground surface at low magnification (location 1 in **g**) showing levelled and rounded grains. **j**, Bright use-polish with striations (arrows, location 2 in **g**). Scale bar, 0.1 mm. **k**, Bright, reticulated use-polish (location 3 in **g**). Scale bar, 0.05 mm. **l**, Specimen GS73 (from

2015 spit 52): bright, undulating use-polish, with red pigment residues in the lowest regions of the grains (circle, location 1 in **s**). Scale bar, 0.05 mm. **m–r**, Specimen GS79 (from 2015 spit 54) used for the manufacture and sharpening of stone hatchets. **m**, Plan view. Scale bar, 5 cm. **n**, Ground surface. **o**, Side view. **p**, Angled view, upper surface is ground, note the flake margins. **q**, Location 2 in **p** showing flake scars. **r**, Ground surface at low magnification (location 1 in **n**) showing levelled grains and deep striations (arrows). **s–v**, Fragment of GS73 with deep partial grooves: **s**, Ground surface. Scale bar, 5 cm. **t**, Side view. **u**, Plan view. **v**, Ground surface at low magnification, note the deep striations and red surface staining (location 2 in **u**).



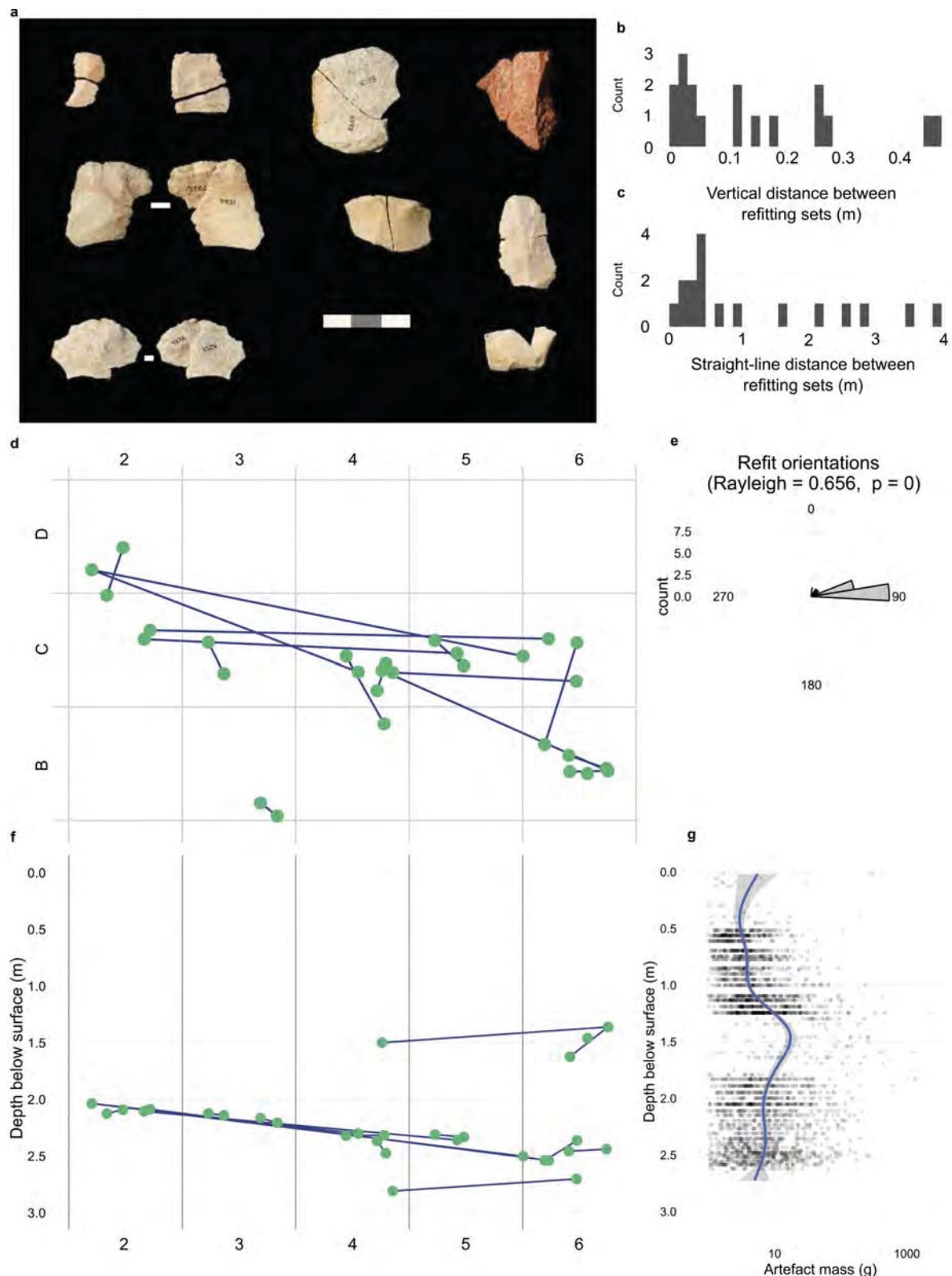
Extended Data Figure 4 | Dolerite edge-ground hatchet heads showing plan and end views. Main scale bars are 5 cm. Vertical double-ended arrows indicate the haft zones. **a**, EGH7 from unit C1/35 (base of phase 3) with shouldered or stemmed design for a haft. Two upper insets show (left; scale bar, 2 mm) striations from grinding and (right; scale bar, 0.2 mm) polish from use. The lower insets show (left; scale bar, 0.2 mm) wear from haft movement and (right; scale bar, 0.01 mm) detail of the polish (smooth white zones) and possible resin (red smears with black

spots). **b**, EGH1 from unit C1/33 (phase 4) with large flake scarring and cracks within the haft zone. **c**, EGH8 from unit C1/38 (base of phase 3) with a slight waist design for a haft. **d**, EGH6 from C1/33 (phase 3) with grooved design for a haft and red stain from mixing pigment (ellipse). The upper inset (scale bar, 2 mm) shows traces of use (vertical arrows) and grinding (horizontal arrows). The lower inset (scale bar, 0.2 mm), from inside the groove, shows polish from haft movement.



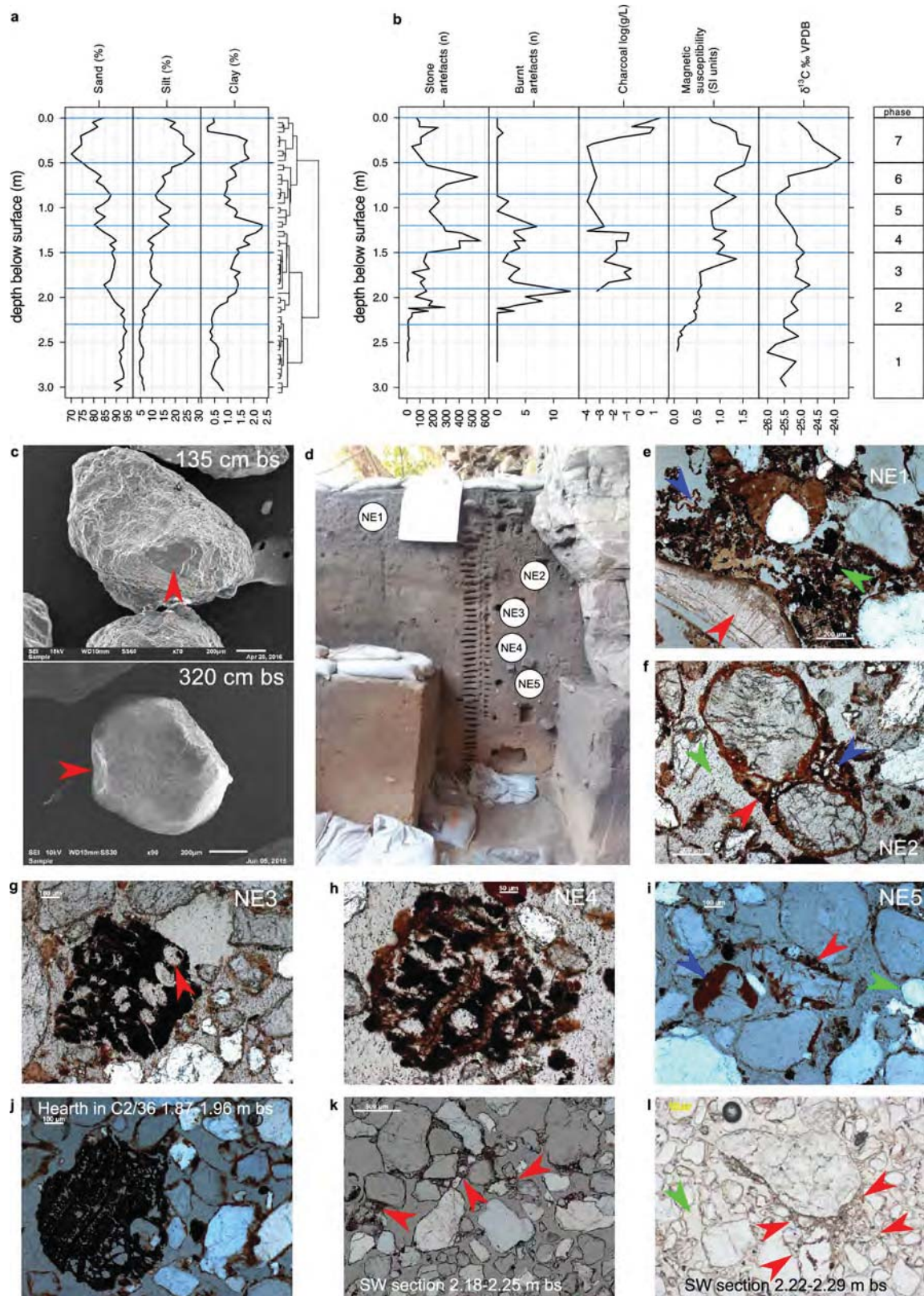
Extended Data Figure 5 | Hearth SF56 with grindstones and carbonized *Pandanus* drupe from a hearth in spit C2/41. **a**, Photograph of hearth pit SF56 in C4/35 (phase 3) showing *in situ* grinding stones in a hearth with elevated magnetic susceptibility readings, and a probable cache of ground ochre, grindstones and hatchet heads against the back wall.

b, d, Scanning electron microscope images of modern reference specimen 2639, *Pandanus spiralis* drupe (13× and 90× magnifications, respectively). **c, e**, Photographs of archaeological specimen C2/41(1), *Pandanus* sp. drupe. Note the seed locule, vascular bundles and flaring ground tissue apparent on both modern reference and archaeological specimens.



Extended Data Figure 6 | Summary of Madjedbebe silcrete artefact refitting analysis. **a**, Selection of refitting and conjoining artefacts; scale bar intervals, 10 mm. **b**, Histogram showing the distribution of vertical distances between refitting artefact fragments. The median vertical refit distance is 0.10 m, with a median absolute deviation of 0.13 m. **c**, Histogram showing the distribution of straight-line distances between refitted artefact fragments. The median straight-line refit distance is 0.44 m, with a median absolute deviation of 0.47 m. **d**, Plan view showing the refitted artefacts at the locations where they were found at the time of excavation. Blue lines connect refitted pieces. Annotations on the

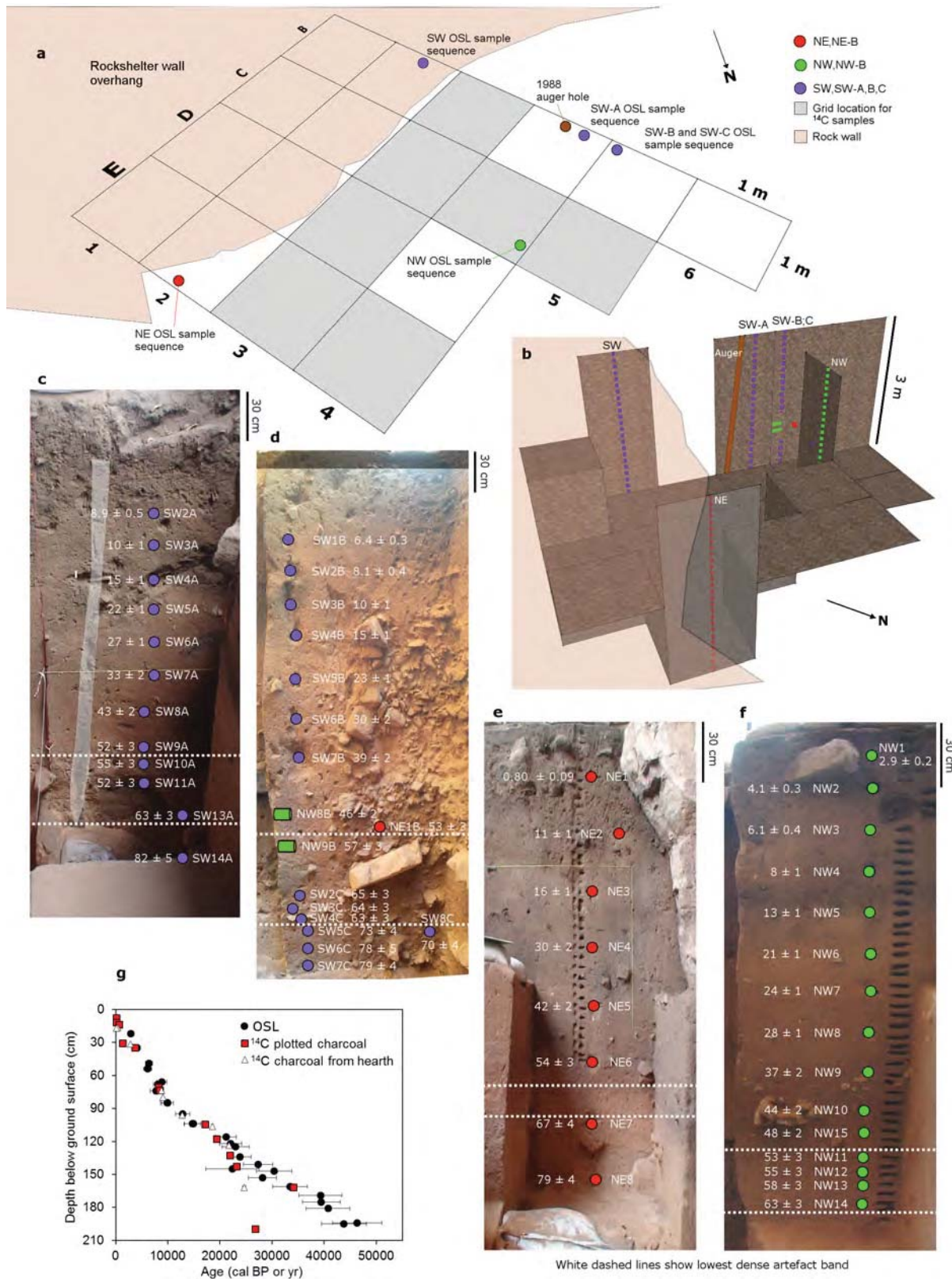
axes show the excavation grid coordinates. **e**, Polar plot of horizontal orientations of the vector between pairs of refitted pieces. The Rayleigh test result indicates a significantly non-random distribution. For most refits, both artefacts in the refit pair were recovered from the same horizontal plane. **f**, Section view showing the refitted artefacts at the locations where they were found at the time of excavation. Blue lines connect refitted pieces. **g**, Plot of artefact mass by depth in square B6: each point represents one artefact, the blue line is a robust locally weighted regression, and the grey band is the 95% confidence region for the LOWESS regression line.



Extended Data Figure 7 | See next page for caption.

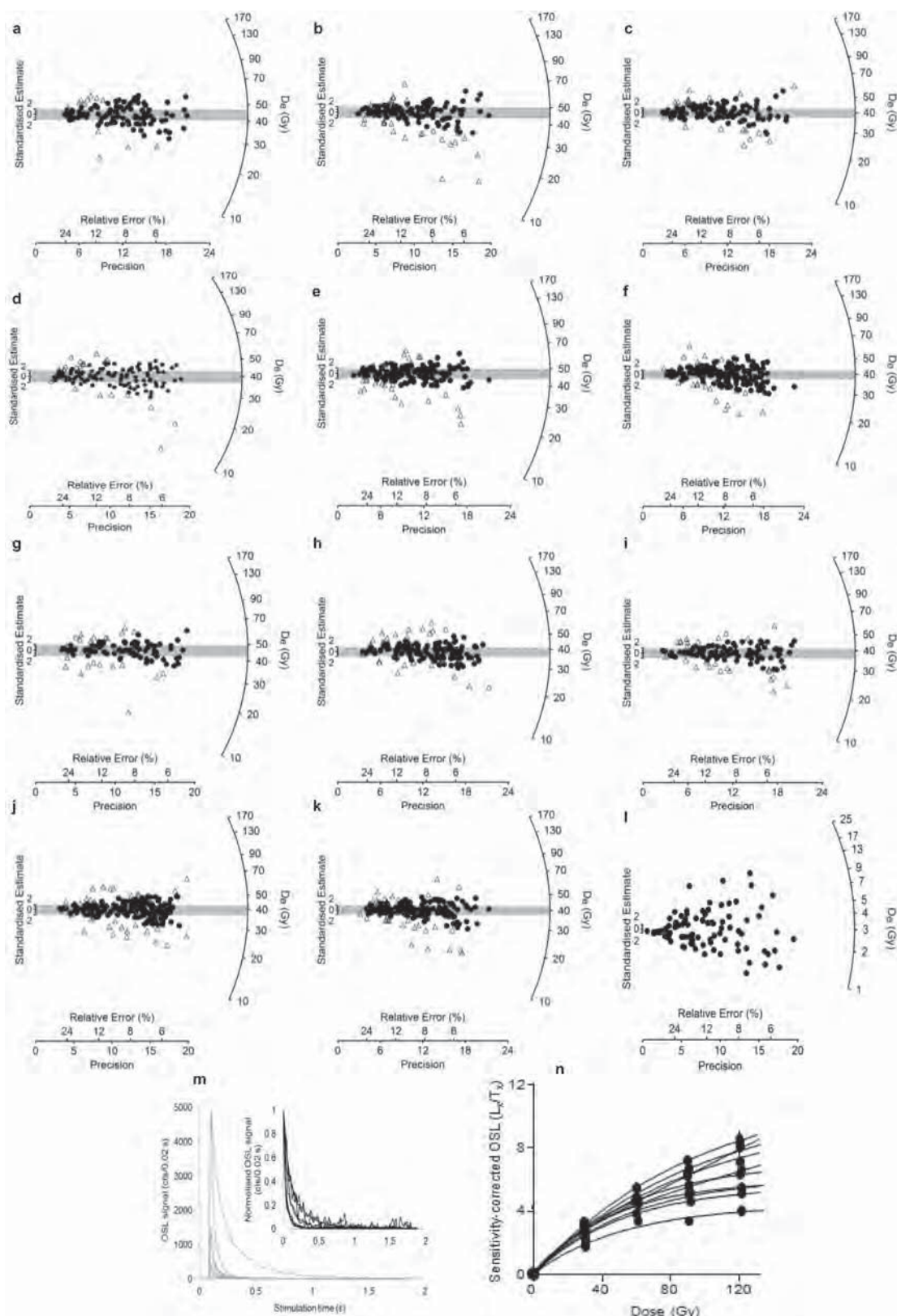
Extended Data Figure 7 | Summary of Madjedbebe geoaerchaeological analysis. **a**, Particle size distributions of bulk samples extracted from the southwest wall of square D3 (left) and constrained cluster analysis dendrogram (right). Blue horizontal lines indicate the artefact discard phases, calibrated for squares C3 and D3. **b**, Distributions of key geoaerchaeological variables measured on bulk samples extracted from the southwest wall of square D3. Magnetic susceptibility units are $10^{-7} \text{ m}^3 \text{ kg}^{-1}$; VPDB is Vienna Pee Dee Belemnite, an international reference standard for $\delta^{13}\text{C}$ analysis. **c**, Scanning electron microscope images of sand grains from 1.35 m (top) and 3.20 m (bottom) depth below surface (bs). **d**, Photograph of the northeast section of the 2012 excavation area. Labels in white circles indicate locations of micromorphology samples. **e**, Micromorphology sample NE1 from the midden deposit showing shell fragment (red arrow), charcoal (green arrow) and root fragment (blue arrow). **f**, Micromorphology sample NE2 from the lower

midden deposits showing linked-capped grains (red arrow), silt (blue arrow) and voids (green arrow). **g**, Micromorphology sample NE3 from below the midden showing weathered charcoal fragment with clay infill (red arrow). **h**, Micromorphology sample NE4 showing an extensively weathered charcoal fragment. **i**, Micromorphology sample NE5 showing grain with silty coating (red arrow), grain with clay coating (blue arrow) and grain with no coating (green arrow). **j**, Micromorphology sample from the C2/36 hearth feature showing a well-preserved charcoal fragment. **k**, Micromorphology sample from the southwest section of square D3 (2.18–2.25 m depth below surface) showing linked-capped grains (red arrows), similar to sample NE2. **l**, Micromorphology sample from the southwest section of square D3 (2.22–2.29 m depth below surface) showing packing voids (green arrow) and a polymineral grain with linked-capping joining it with smaller grains (red arrows).



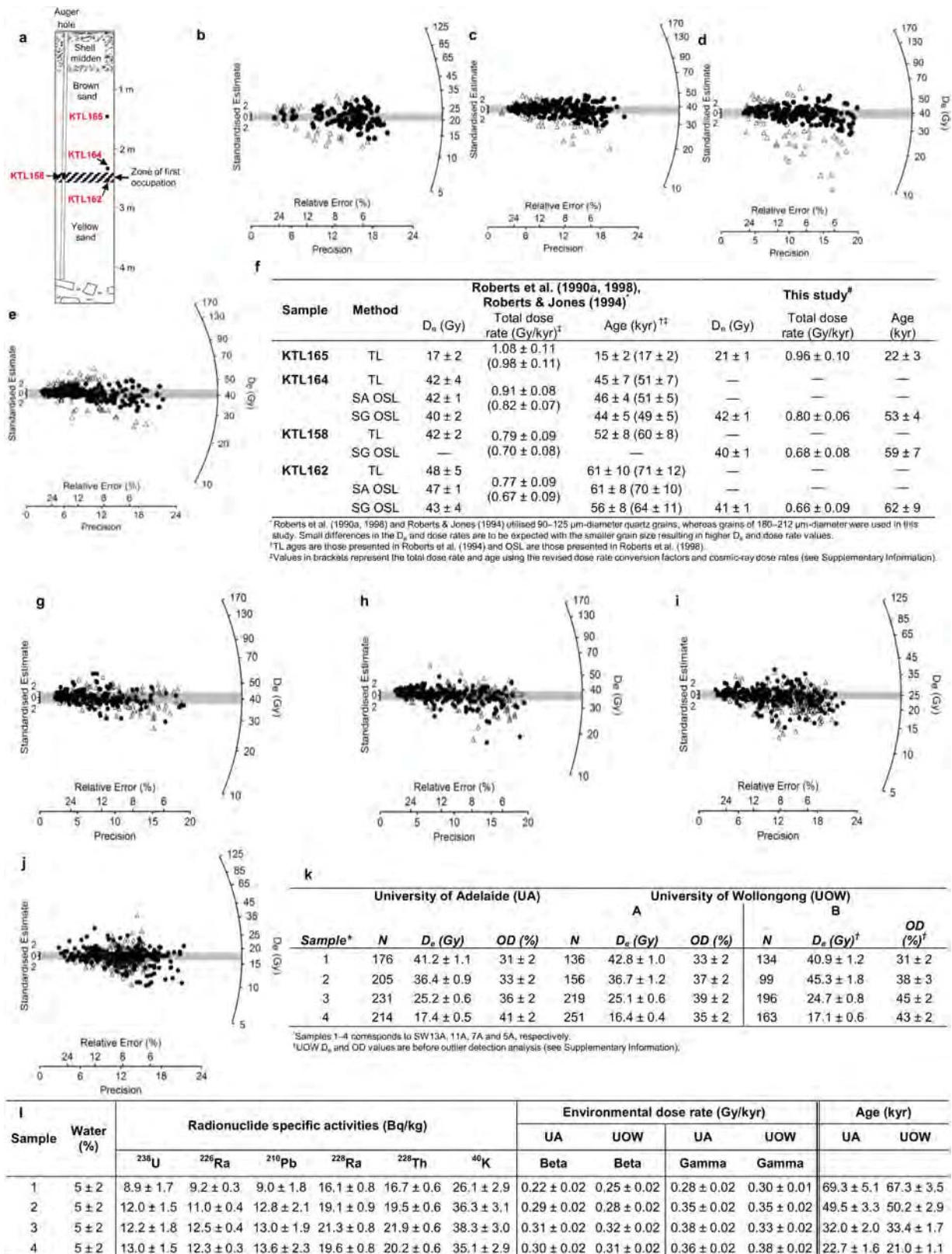
Extended Data Figure 8 | Site plan, OSL sample locations and ages.
a, Two-dimensional site plan of excavated squares, showing the locations of the OSL sample series. Grey-shaded squares represent squares from which charcoal samples were collected for ¹⁴C dating. **b**, Three-dimensional site plan, showing both horizontal and vertical positions of the OSL sample series. Samples shown in the same colour were taken from section walls with the same orientation. **c–f**, Photographs of the

sedimentary deposit for each of the walls from which OSL samples were collected, together with the OSL ages (uncertainties at 68.2% confidence level) and the lowest dense artefact band (phase 2) demarcated by the stippled lines. **c**, Southwest wall of square B5. **d**, Southwest wall of square B6. **e**, Northeast wall of square E2. **f**, Northwest wall of square C4. **g**, Comparison of ¹⁴C and OSL ages (uncertainties at 95.4% confidence level) obtained in this study from the upper 2 m of deposit.



Extended Data Figure 9 | OSL data for individual sand-sized grains of quartz. **a–k**, Radial plots of single-grain D_e values for each sample within the lowest dense artefact band (phase 2). **a**, SW4C; **b**, SW3C; **c**, NW14; **d**, SW13A; **e**, SW2C; **f**, NW13; **g**, SW11A; **h**, NW12; **i**, NW11; **j**, SW10A; **k**, NW9B. **l**, Radial plot of D_e values for single grains of sample NE1, collected from the shell midden at the top of the sequence. The grey bands in each plot are centred on the weighted mean D_e

determined for each dose population using the central age model, after the rejection of outliers (shown as open triangles). **m**, OSL decay curves for a representative sample of grains from SW13A that span the range of observed luminescence sensitivities (that is, their relative brightness). The inset plot shows the same curves on a normalized y axis. **n**, Corresponding dose response curves for the grains shown in **m**.



Extended Data Figure 10 | See next page for caption.

Extended Data Figure 10 | Verification of previous luminescence ages and inter-laboratory comparison. **a**, Schematic diagram of square B4 (modified after ref. 13) showing the relative positions of four samples for which ages have been reported previously^{13,15,16} and that were re-measured and evaluated in this study. **b–e**, Radial plots of single-grain D_e values measured in this study for these four samples. **b**, KTL165; **c**, KTL164; **d**, KTL158; **e**, KTL162. The grey bands in each plot are centred on the weighted mean D_e determined for each dose population using the central age model, after the rejection of outliers (shown as open triangles). **f**, Previously published D_e values, total dose rates and ages, together with the revised dose rates and ages (values in parentheses; see Supplementary Information for explanation) and the new single-grain OSL D_e values (based on the data shown in **b–e**) and ages obtained in this study. **g–j**, Radial plots of single-grain D_e values for the four samples measured independently in two laboratories (University of Wollongong,

UOW; University of Adelaide, UA). **g**, Sample 1 (SW13A); **h**, Sample 2 (SW11A); **i**, Sample 3 (SW7A); **j**, Sample 4 (SW5A). Filled circles and open triangles are D_e values obtained at UA and UOW, respectively. The grey bands in each plot are centred on the weighted mean D_e determined using the central age model for each dose population measured at UA. **k**, Comparison of weighted mean D_e and overdispersion (OD) values for the same samples measured at UA and UOW ('A') using a preheat combination of 260 °C for 10 s (PH₁) and 220 °C for 0 s (PH₂), and at UOW ('B') using a preheat combination of 220 °C for 10 s (PH₁) and 160 °C for 5 s (PH₂). **l**, High-resolution gamma-ray spectrometry results obtained at UA and the beta and gamma dose rates and OSL ages calculated from these data, compared to the beta and gamma dose rates and OSL ages obtained independently at UOW (using preheat combination 'A' for D_e determination).

SI section 1:

Supplementary Discussion | Previous chronologies

Supplementary Table 1 | Published ages obtained for charcoal, shell and sediment samples collected at Madjedbebe in 1973 and 1988/89.

SI section 2:

Supplementary Table 2 | Radiocarbon (^{14}C) ages for charcoal samples collected in this study from Madjedbebe.

SI section 3:

Supplementary Discussion | Optically stimulated luminescence (OSL) dating

Supplementary Table 3 | Dose recovery test results

Supplementary Table 4 | Single grain OSL rejection information

Supplementary Table 5 | Dose rate data, equivalent doses (D_e), overdispersion (OD) values, and OSL ages for samples from the front of the cave

Supplementary Table 6 | Dose rate data, equivalent doses (D_e), overdispersion (OD) values, and OSL ages for samples from the back of the cave

Supplementary Table 7 | Weighted mean D_e values and OD values under two different scenarios

Supplementary Table 8 | Revised dose rate and ages for samples previously reported by Roberts et al. (1990a, 1998) and Roberts and Jones (1994)

Supplementary Table 9 | OSL measurements procedures used at the University of Adelaide (UA)

Supplementary Table 10 | Single grain OSL rejection information for samples measured at UA

Supplementary Table 11 | Bayesian model outputs and ages

Supplementary Table 12 | Bayesian model code

SI section 4:

Supplementary Discussion | Artefact analysis

Supplementary Table 13 | Stone artefact counts for B6

Supplementary Table 14 | Stone artefacts counts for C4

Supplementary Table 15 | Chi square test on raw materials

SI section 5:

Supplementary Discussion | Usewear and residues

Supplementary Table 16 | Edge ground hatchet heads

Supplementary Table 17 | Micro-wear and edge residues on edge ground hatchet heads

SI section 6:

Supplementary Discussion | Archaeobotanical analysis and hearths

Supplementary Table 18 | Taxonomic composition

Supplementary Table 19 | Ages, taxonomy and sample size

SI section 7:

Supplementary Discussion | Pigment characterisation

Supplementary Table 20 | pXRF spectra from subsurface sandstone slab residues

Supplementary Table 21 | Mineral identifications for lower ochres, Square C4 and Art 9

SI section 8:

Supplementary Discussion | Palaeoclimate 65 kyr ago

SI section 9:

Supplementary Discussion | Ground pigment from Phase 2

Supplementary Table 22 | Ground pigment counts and weights, Squares C4 and B6

SI section 10:

Supplementary Discussion | Geoarchaeology

References

SI SECTION 1

Previous chronologies

A total of 28 numerical age determinations have been published previously for Madjedbebe (Supplementary Table 1); the ages reported in this table supersede those listed in Table 1 of Clarkson et al. (2015).

Three radiocarbon (^{14}C) ages have been reported for estuarine shells from the Holocene midden (Gillespie and Temple, 1977; Clarkson et al., 2015) and eleven ^{14}C ages for charcoal fragments from depths of up to 2.6 m below the ground surface (Gillespie and Temple, 1976, 1977; Roberts et al., 1990a, 1990b; Bird et al., 2002; Clarkson et al., 2015). Ten thermoluminescence (TL) ages have been published for quartz grains extracted from sediment samples collected from depths of up to 4.6 m (Roberts et al., 1990a, 1990b; Roberts and Jones, 1994), and two of these samples (KTL162 and KTL164) were dated subsequently using single aliquot and single grain optically stimulated luminescence (OSL) procedures for quartz (Roberts et al., 1998), which were then in their infancy.

Four of the ^{14}C samples (SUA-263, -264C, -264/S1 and -265) were collected in 1973 during a test excavation by Kamminga and Allen (1973). The remaining ^{14}C samples, and all of the TL and OSL samples, were collected by R.G.R., M.A.S. and Rhys Jones in 1988 by hand auger or during their subsequent excavation of the site in 1989. The elevation of the ground surface in 1973 and 1988/1989 relative to surface as surveyed in 2012 and 2015 is not known exactly, but could differ by one to two decimetres based on the depths below surface measured in 2012 for three of the TL samples collected in 1989.

The ^{14}C samples have been prepared using a variety of pretreatment procedures, and measured using beta-counting (SUA- and ANU- samples) or accelerator mass spectrometry (ANUA- samples) techniques. For pretreatment details of the SUA- and ANU- samples, we consulted the original sample submission and age reporting sheets, as well as the published literature. The shell samples were scrubbed, cleaned of surface dirt (using a dental drill in the case of ANU-7003), then etched at room temperature in HCl acid to remove the surface carbonate (SUA-264/S1) or washed in water in an ultrasonic bath water, rinsed and dried (ANU-7002 and -7003); the shell remaining was then crushed for analysis. The charcoal samples were washed in hot HCl acid (SUA-263, -264C and -265, and ANU-7006, -7007 and -7115) or were given an acid–base–acid (ABA) pretreatment of hot HCl, NaOH and a further wash in hot HCl for the NaOH-insoluble fraction (ANU-7004 and -7005).

The three ANUA- charcoal samples were given a more aggressive acid–base wet-oxidation (ABOx) pretreatment regime, together with stepped combustion (SC) to remove contaminants at the lower-temperature steps (Bird et al., 1999a). This procedure has previously been shown to remove modern carbon contaminants better than ABA or acid-only pretreatments, especially with the inclusion of stepped combustion (e.g., Bird and Ascough, 2012; Wood et al., 2016; Bird et al., 2014; Tomiyama et al., 2016). The ages obtained at the highest combustion temperature are usually considered the most reliable. For the Madjedbebe study, however, Bird et al. (2002) did not have access to hand-picked pieces of charcoal, so they instead used flotation to concentrate the fine-grained (<125 µm) size fraction from the sediments, using a sodium polytungstate solution with a density of 1.8 g/cm³. Such finely comminuted charcoal fragments can potentially be displaced after deposition and/or contain contaminants of microbial origin (Bird et al., 1999b), so the resulting ¹⁴C ages should be treated with caution (Bird et al., 2002).

The measured ¹⁴C ages have been calibrated using OxCal program v.4.2 (Bronk Ramsey, 2009a; Bronk Ramsey and Lee, 2013) and the SHCal13 data set (which includes an age offset for the Southern Hemisphere; Hogg et al., 2013), with the age ranges in Supplementary Table 1 expressed at the 95.4% confidence interval. Gillespie and Temple (1977) reported a negligible difference in age between the charcoal and *Pitar* shell samples from the base of the midden (SUA-264C and -264/S1, respectively), so none of the shell ages have been corrected for any marine reservoir effect.

Five sediment samples (asterisked in Supplementary Table 1) were collected in 1988 by hand augering of the sand apron at Madjedbebe, and a further 4 samples were collected in opaque plastic tubes of 5–6 cm diameter during the 1989 excavation. The uppermost 1–2 cm of the sand apron was also sampled to ascertain the extent to which sediments deposited recently in the rock shelter had been exposed to sufficient sunlight to bleach the light-sensitive TL traps. In the laboratory, each sample was split into 3 portions that were used for (1) grain size, porosity and moisture content measurements, (2) radionuclide analyses and (3) equivalent dose (D_e) determinations. The latter portions were used to extract quartz grains for TL dating and, subsequently, for OSL dating.

Sample preparation was conducted under low-intensity yellow or red (KTL162, KTL164 and KTL167) illumination. The sediments were chemically pretreated to disaggregate any clays and destroy any carbonates and organic matter, and heavy minerals were removed using a sodium polytungstate solution with a density of 2.74 g/cm³. Quartz grains of 90–125 µm in diameter were then isolated by dry sieving and etched in 40%

hydrofluoric acid for 40 min to remove the alpha-irradiated coat of each grain and dissolve any feldspar grains. The purified quartz grains were then analysed using multiple-aliquot additive and regenerative dose TL procedures (reviewed by Lian and Roberts, 2006), in which each aliquot consists of several thousand grains, and later by regenerative dose OSL procedures for single aliquots (~800 grains per aliquot) and individual grains (Roberts et al., 1998).

High-resolution gamma-ray spectrometry was used to measure the activities of radionuclides in the ^{238}U , ^{235}U and ^{232}Th decay chains, and of ^{40}K . These activities were converted to beta and gamma dose rates using conversion factors current at that time, and adjusted for an estimated long-term sample water content of ~5% (the same value as used in the present study). A small internal alpha dose rate (~2% of the total dose rate) and a cosmic-ray dose rate of 0.15 ± 0.025 Gy/kyr were also included in the total dose rate for each sample. This fixed cosmic-ray value does not take into account the actual depth of each sample or the thickness of rock shielding behind and above the deposit, so corrections for these have been implemented in this study (see below).

The ages published by Roberts et al. (1990a) and Roberts and Jones (1994) showed acceptable agreement between the ^{14}C and TL chronologies, as illustrated by the two ^{14}C ages of 14.9–17.4 (ANU-7006) and 17.8–18.6 (ANU-7007) cal kyr BP (Table OSL_S1) that stratigraphically bracket KTL165 (15 ± 2 kyr with the uncertainty expressed at 1σ). The latter is also consistent with the ^{14}C age obtained for the highest temperature ABOx-SC analysis of finely comminuted charcoal extracted from this sediment sample: 14.9–16.2 cal kyr BP (ANUA-9914). Likewise, the two ^{14}C ages of 18.4–29.5 (ANU-7115) and 21.0–22.5 (SUA-265) cal kyr BP are also stratigraphically consistent with the age of KTL97 (24 ± 4 kyr), bearing in mind the large depth intervals of both SUA-265 and KTL97. The only ^{14}C sample dated from deeper in the stratigraphy (ANUA-9915) yielded an anomalously young age (12.1–13.1 cal kyr BP) compared to those of the five overlying ^{14}C samples and four TL samples, which we attribute to chemical alteration (after Bird et al., 2002) and/or physical displacement of the finely comminuted charcoal.

The TL ages for KTL162 and KTL164 are also consistent with the corresponding single aliquot and single grain OSL ages, determined using procedures that had only just been developed (Murray and Roberts, 1997, 1998). D_e values were estimated for 24 single aliquots and 85–86 individual grains of each sample. Both of the single grain ages were calculated from fewer than 20 grains and only one grain in each sample had a D_e estimate substantially smaller than the other D_e values, which Roberts et al. (1998) interpreted as evidence for a

lack of significant post-depositional disturbance. The concordance between the TL and OSL ages for these two samples further suggests that the grains were exposed to sufficient sunlight at the time of deposition to effectively bleach the light-sensitive electron traps. The OSL ages are based on the most easily bleached traps in quartz, whereas the TL ages are based primarily on the traps associated with the hard-to-bleach 375°C glow peak. Agreement between the two pairs of ages implies, therefore, that even these TL traps were adequately bleached (Roberts et al., 1998), an inference supported by the young TL age (~200 years) obtained for the near-surface sample (Roberts et al., 1990a).

The ^{14}C , TL and OSL ages in Supplementary Table 1 increase steadily with depth below surface. Roberts et al. (1990b) plotted the TL ages for the nine Pleistocene samples as a function of depth and showed that they all lie within experimental error of the 95.4% confidence limits about the fitted least-squares regression line. This result is consistent with a constant rate of sedimentation at Madjedbebe between about 110 and 15 kyr ago (Roberts et al., 1990b), but the TL ages have uncertainties that are sufficiently large that interruptions of several millennia in duration may be concealed within this overall trend. Clarkson et al. (2015) conducted a Bayesian change point analysis of the ^{14}C , TL and OSL ages listed in their Table 1 to identify any changes in sedimentation rate. Different accumulation rates were detected, but no obvious breaks in sedimentation. To test alternative models of sand apron development at Madjedbebe requires a larger number of samples collected at higher spatial resolution, combined with ages measured with higher precision.

The TL and OSL chronologies constrain the ‘zone of first occupation’ (as defined by Roberts et al., 1990a; Extended Data Fig. 2a) to between 52 ± 8 and 61 ± 10 kyr (TL ages for KTL158 and KTL162, respectively). More conservative age estimates for the level of the lowest artefacts (2.6 m) are 51 ± 5 kyr based on the regression model for the TL ages (Roberts et al., 1990b) and 55.5 ± 8.2 kyr (single grain OSL age for KTL162). Clarkson et al. (2015) reanalysed the stone artefact assemblage excavated in 1989 and identified artefacts from levels as deep as 2.8 m; these are underlain by culturally sterile sediments dated by TL to 65 ± 11 kyr (KTL141) or 57 ± 5 kyr based on the regression model of Roberts et al. (1990b). In sum, therefore, previous chronologies for Madjedbebe have suggested that initial occupation occurred after 65 ± 11 kyr and before 51 ± 5 kyr.

Supplementary Table 1: Published ages obtained for charcoal, shell and sediment samples collected at Madjedbebe in 1973 and 1988/89.

Sample code ^a	Depth (cm) ^b	Method ^c	Material dated	Laboratory procedure(s) ^d	Age (years) ^e	Calibrated age range (cal years BP) ^f	Reference source
KTL-156	1–2	TL	Quartz	E	200 ± 1200		Roberts et al., 1990a; Roberts & Jones, 1994
SUA-263	~10	¹⁴ C	Charcoal (from burial pit)	B	450 ± 80	550–305	Gillespie & Temple, 1976
ANU-7002	10–16	¹⁴ C	Shell (<i>Cerithidea obtusa</i>)	A	3810 ± 80	4411–3925	Clarkson et al., 2015
ANU-7003	54–60	¹⁴ C	Shell (<i>Telescopium</i> sp.)	A	6290 ± 90	7415–6933	Clarkson et al., 2015
SUA-264/S1	65–78	¹⁴ C	Shell (<i>Pitar</i> sp.)	B	6360 ± 100	7430–6985	Gillespie & Temple, 1977
SUA-264C	65–88	¹⁴ C	Charcoal	B	6355 ± 250	7672–6651	Gillespie & Temple, 1976, 1977
ANU-7004	91–95	¹⁴ C	Charcoal	C	7300 ± 230	8538–7664	Clarkson et al., 2015
ANU-7005	107–116	¹⁴ C	Charcoal	C	10,470 ± 120	12,658–11,841	Clarkson et al., 2015
ANU-7006	142–147	¹⁴ C	Charcoal	B	13,390 ± 400	17,375–14,880	Roberts et al., 1990a
KTL-165	149–155	TL	Quartz	E	15,000 ± 2000		Roberts et al., 1990a; Roberts & Jones, 1994
ANUA-9913	149–155	¹⁴ C	Charcoal (<125 µm fraction)	D (340°C)	10,330 ± 150	12,555–11,405	Bird et al., 2002
ANUA-9914	149–155	¹⁴ C	Charcoal (<125 µm fraction)	D (650/880°C)	13,050 ± 210	16,232–14,934	Bird et al., 2002
ANU-7007	151–161	¹⁴ C	Charcoal	B	14,990 ± 150	18,556–17,838	Roberts et al., 1990b
ANU-7115	168–174	¹⁴ C	Charcoal	B	18,810 ± 2090	29,539–18,428	Clarkson et al., 2015
SUA-265	188–215	¹⁴ C	Charcoal	B	18,040 ± 300	22,461–21,011	Gillespie & Temple, 1976
KTL97 *	190–209	TL	Quartz	E	24,000 ± 4000		Roberts et al., 1990a; Roberts & Jones, 1994
KTL164	230–236	TL	Quartz	E	45,000 ± 7000		Roberts et al., 1990a; Roberts & Jones, 1994
	230–236	OSL	Quartz	F	45,700 ± 4100		Roberts et al., 1998

Sample code ^a	Depth (cm) ^b	Method ^c	Material dated	Laboratory procedure(s) ^d	Age (years) ^e	Calibrated age range (cal years BP) ^f	Reference source
	230–236	OSL	Quartz	G	44,200 ± 4700		Roberts et al., 1998
KTL158 *	241–254	TL	Quartz	E	52,000 ± 8000		Roberts et al., 1990a; Roberts & Jones, 1994
KTL162	254–259	TL	Quartz	E	61,000 ± 10,000		Roberts et al., 1990a; Roberts & Jones 1994
	254–259	OSL	Quartz	F	60,700 ± 7500		Roberts et al., 1998
	254–259	OSL	Quartz	G	55,500 ± 8200		Roberts et al., 1998
ANUA-9915	254–259	¹⁴ C	Charcoal (<125 μm fraction)	D (340/650°C)	10,810 ± 200	13,078–12,072	Bird et al., 2002
KTL141 *	295–315	TL	Quartz	E	65,000 ± 11,000		Roberts et al., 1990a; Roberts & Jones, 1994
KTL167 *	339–362	TL	Quartz	E	82,000 ± 13,000		Roberts et al., 1990b; Roberts & Jones, 1994
KTL116 *	390–411	TL	Quartz	E	86,000 ± 14,000		Roberts et al., 1990a; Roberts & Jones, 1994
KTL163	452–458	TL	Quartz	E	107,000 ± 16,000		Roberts et al., 1990a; Roberts & Jones, 1994

^a Asterisks denote TL samples collected from the auger hole in 1988.

^b Depth below ground surface as cited in the original publications. The elevation of the ground surface in 1973 (SUA samples) and 1988/89 (all other samples) relative to that in 2012/15 is not known exactly.

^c ¹⁴C, radiocarbon; TL, thermoluminescence; OSL, optically stimulated luminescence.

^d A – Surfaces cleaned and rinsed with water; no chemical pretreatment.

B – Pretreatment with hot HCl acid (charcoal) or HCl acid at room temperature (shell).

C – Acid–base–acid (ABA) pretreatment.

D – Acid–base wet-oxidation (ABOX) pretreatment with stepped combustion (SC) at temperature(s) in parentheses

E – Multiple aliquots, additive and regenerative dose procedures

F – Single aliquots, regenerative dose procedure

G – Single grains, regenerative dose procedure

^e TL and OSL ages are expressed in calendar years; the associated uncertainties are at 1σ, where the random and systematic errors are added in quadrature. The ¹⁴C ages and standard errors are expressed in radiocarbon years before present (BP), where the present is defined as AD 1950.

^f ¹⁴C age ranges at the 95.4% confidence interval, calibrated using OxCal program v.4.2 and the SHCal13 data set (i.e., incorporating the Southern Hemisphere offset). The shell ages are not corrected for any marine reservoir effect.

SI SECTION 2

Supplementary Table 2: Radiocarbon (^{14}C) ages for charcoal samples collected in this study from Madjedbebe. Measured ages have been calibrated using the SHCal13 dataset in OxCal program v.4.2 (Bronk Ramsey, 2009a; Bronk Ramsey and Lee, 2013; Hogg et al., 2013), with the age ranges shown in at the 95.4% confidence interval. Sample pretreatments are acid–base–acid (ABA) or acid–base wet-oxidation (ABOX).

Lab ID	Depth (cm)	Square/spit	Feature*	Chemical pretreatment	$\delta^{13}\text{C}$ (‰)	Conventional ^{14}C age (yrs BP)	Error (1σ)	Calibrated age range (cal yrs BP)
OZQ464	7.8	C3/4	Plotted charcoal	ABA	-25.1	145	20	260 – 0
OZT582	12.0	C4/5	Plotted charcoal	ABA	-24.8	170	25	280 – 0
OZQ471	13.9	B3/5	Plotted charcoal	ABA	-24.4	775	20	720 – 650
OZQ460	16.5	E4/6A	Charcoal from hearth	ABA	-25.8	330	20	450 – 300
Wk43609	17.0	E3/5A	Charcoal from hearth	ABA		98	20	240 – 7
OZR149	31.0	D3/9	Plotted charcoal	ABA	-23.3	1555	25	1470 – 1300
Wk43604	31.4	C4/9A	Charcoal from hearth	ABA		2757	20	2860 – 2760
OZT583	35.1	C4/9	Plotted charcoal	ABA	-25.3	3550	25	3870 – 3690
OZQ472	70.7	D3/16	Plotted charcoal	ABA	-25.5	7485	35	8360 – 8180
Wk43607	73.6	D3/16B	Charcoal from hearth	ABA		7806	20	8600 – 8460
OZT584	73.7	C3/17	Plotted charcoal	ABA	-27.2	7935	35	8980 – 8590
Wk43603	79.8	C3/18A	Charcoal from hearth	ABA		8170	20	9130 – 9000
Wk43610	96.0	E3/20A	Charcoal from hearth	ABA		10943	23	12810 – 12710
Wk43606	101.7	D2/21A	Charcoal from hearth	ABA		8282	28	9398 – 9034
OZT586	104.7	C4/23	Plotted charcoal	ABOX	-25.0	14160	50	17420 – 16970
Wk43611	106.3	E4/22A	Charcoal from hearth	ABA		15323	35	18690 – 18410
OZQ510	118.0	C3/25	Plotted charcoal	ABA	-24.3	16130	40	19580 – 19240
OZT587	123.5	C4/26A	Charcoal from hearth	ABOX	-24.4	17990	60	21950 – 21520
OZT590	133.0	C4/28	Plotted charcoal	ABOX	-24.6	18130	60	22180 – 21690
OZT591	142.9	C4/31	Plotted charcoal	ABOX	-22.7	19290	70	23470 – 22940
Wk43605	161.9	C4/36A	Charcoal from hearth	ABA		20511	69	24970 – 24340
OZT592	161.9	C5/38	Plotted charcoal	ABOX	-24.2	30100	140	34430 – 33820
OZT593	199.9	C5/45	Plotted charcoal	ABOX	-24.1	22570	80	27160 – 26530

* Plotted charcoal refers to an isolated piece of charcoal that was recorded and plotted *in situ*, but that did not come from an identifiable hearth feature.

SI SECTION 3

Optically stimulated luminescence (OSL) dating

OSL dating provides a means of determining burial ages for sediments and associated artefacts and fossils (Huntley et al., 1985; Aitken, 1998; Duller, 2004; Jacobs and Roberts, 2007; Wintle, 2014; Roberts et al., 2015). The method is based on the time-dependent increase in the number of trapped electrons induced in mineral grains (such as quartz) by low levels of ionising radiation from the decay of natural uranium, thorium and potassium in the surrounding deposits, and from cosmic rays. The time elapsed since the light-sensitive electron traps were emptied can be determined from measurements of the OSL signal – from which the equivalent dose (D_e) is estimated – together with determinations of the radioactivity of the sample and the material surrounding it to a distance of ~30 cm (the environmental dose rate). The OSL ‘clock’ is reset by just a few seconds of exposure to sunlight. The D_e divided by the environmental dose rate gives the burial time of the grains in calendar years before present.

Sample collection and preparation

Fifty-two samples were collected for OSL dating from the upper ~3 m of deposit during the 2012 and 2015 excavation seasons (Extended Data Fig. 8). All samples were collected in light-tight plastic tubes (~5 cm in diameter and 15 cm in length) or stainless steel tubes (2 cm diameter and 10 cm long) to prevent inadvertent exposure of the sediment to sunlight, which would have reset the luminescence ‘clock’. All samples were packed in light-safe black plastic bags and transported to the laboratory at the University of Wollongong. A sub-sample of sediment was collected from the back of each tube hole for measurement of the prevailing moisture contents and for laboratory-based radioactivity measurements.

Samples were collected from 4 different excavated profiles – the southwest face of square B4 (“SW-A” OSL samples), the southwest face of squares B5 and B6 (“SW-B” and “SW-C” OSL samples), the northwest face of square C4 (“NW” OSL samples) and the northeast face of square F2 (“NE” OSL samples). Two samples (NW8B and NW9B) were collected from the NW face of square B4 in line with the “SW-B” and “SW-C” sample series. We also collected samples from the SW face close to the rock wall in square B2; analysis of this sample set has yet to be completed. All sample locations are indicated in Extended Data Fig. 8. Samples collected from section walls with the same direction are shown in the same colour (e.g., all samples collected from SW section walls are shown in purple, whereas those collected from NW section walls are shown in green and NE section walls in red). The

squares from which individual samples were collected are shown in Extended Data Fig. 8a, a plan of the site, with the sampled squares indicated using the nomenclature above. Extended Data Fig. 8b shows a three-dimensional model of the site, with the section walls annotated with the OSL sample sequences. We concentrated our sampling efforts towards the front of the excavated area (rows 4 to 6), in the area excavated most recently (squares C5, and B5 and B6) and in the squares closest to the earlier excavations by Jones, Smith and Roberts (B4 and part of B5); the latter facilitates comparison with the previous thermoluminescence (TL) and OSL chronologies for Madjedbebe (Roberts et al., 1990a, 1998; Roberts and Jones, 1994).

There is a discernable downward slope in the deposits from the back to the front of the rock shelter. The magnitude of the slope is not accurately known, but is thought to be in the order of ~30 cm over 5 m. This slope, however, is less in the upper ~1 m of the deposit, so the NE sample series is treated separately from other samples because their exact depth relationship is not known. Some of the samples reported in Roberts et al. (1990a) and Roberts and Jones (1994) were collected from an auger hole made in 1988 (location shown in Extended Data Fig. 8a,c) and the additional samples collected by them using sample tubes were collected from between the auger hole and the SW-A sample column.

Along each face, samples were collected in a column at regular depth intervals; the mid-point depth below surface of each sample tube is provided in Supplementary Table 5 and 6. Some of the samples are related to 3 discrete and dense artefact bands (Extended Data Fig. 2). The lowest dense artefact band (2.60–2.15 m below surface) immediately overlies an archaeologically sterile sand unit, and the other two dense artefact bands (1.55–0.95 m and 0.70–0.35 m below surface) are separated by bands of comparatively lower archaeological visibility (Extended Data Fig. 2). Samples were collected at higher resolution within the lowest dense artefact band to constrain the start date of human occupation at Madjedbebe as tightly as possible. The individual sample positions are shown on photographs of each of the sediment walls in Extended Data Fig. 8c–f. The samples associated with the lowest dense artefact band, between 2.60 and 2.15 m depth below surface at the front of the site, occur between the stippled lines in these photographs.

Single grain OSL measurements and experimental details

In the OSL dating laboratory, the sample tubes were opened under dim red light. Quartz grains of 180–212 μm in diameter were extracted from the sampled sediments and purified using hydrochloric (HCl) acid and hydrogen peroxide. The sand-sized grains were then etched in 48% hydrofluoric acid for 40 min to remove the external α -dosed layer (~10 μm) of each

grain and to destroy any feldspar grains present in the sample. Samples were then rinsed in HCl acid to remove any precipitated fluorides, and dried and sieved again to the lower sieve size (180 μm).

D_e values were estimated for individual grains (180–212 μm in diameter) for all samples, and standard Risø single grain aluminium discs (Bøtter-Jensen et al., 2000) were used for measurement of individual grains. All measurements were made in an identical manner and with the same equipment, using the single aliquot regenerative dose (SAR) procedure described elsewhere (e.g., Murray and Wintle, 2000; Jacobs et al., 2008). The SAR procedure involves measuring the OSL signals from the natural (burial) dose (L_N) and from a series of regenerative doses (L_x) given in the laboratory by means of a calibrated $^{90}\text{Sr}/^{90}\text{Y}$ beta source. A range of regenerative doses were given to the quartz grains to adequately bracket the D_e estimated from the measured natural signal and each regenerative dose was preheated prior to optical stimulation by an intense green (532 nm) laser beam for 2 s at 125°C. The resulting ultraviolet OSL emissions were detected by an Electron Tubes Ltd 9235QA photomultiplier tube fitted with Hoya U-340 filters. A fixed test dose of ~ 10 Gy was given after each natural and regenerative dose, and the induced OSL signals (T_N or T_x) were used to correct for any sensitivity changes during the SAR sequence. A duplicate regenerative dose was included in the procedure, to check on the adequacy of this sensitivity correction, and a ‘zero dose’ measurement was made to monitor the extent of any ‘recuperation’ induced by the preheat. As a check on possible contamination of the acid-etched quartz grains by feldspar grains or inclusions, we also applied the OSL IR depletion ratio test (Duller, 2003) to each grain at the end of the SAR sequence, using an infrared exposure of 40 s at 50°C.

L_N , L_x , T_N and T_x values were estimated from the first 0.22 s of OSL decay, with the mean count recorded over the last 0.3 s subtracted as background. Sensitivity-corrected (L_x/T_x) dose response curves were then constructed from the L_x and T_x OSL signals, using a linear (for very young samples) or a single saturating-exponential function of the form $I = I_0(1 - \exp^{-D/D_0})$ (see Extended Data Fig. 9n). In this function, I is the L_x/T_x value at regenerative dose D , I_0 is the saturation value of the exponential curve and D_0 is the characteristic saturation dose; I_0 and D_0 are estimated from the data. The sensitivity-corrected natural OSL signal (L_N/T_N) was then projected on to the fitted dose response curve to obtain the D_e by interpolation. The uncertainty on the D_e estimate of each grain (from photon counting statistics, curve fitting uncertainties, and an allowance of 2% per OSL measurement for instrument irreproducibility) was determined by Monte Carlo simulation, using the procedures described by Duller (2007). The

final age uncertainty also includes a further 2% to allow for any bias in the beta source calibration; this systematic error is added in quadrature to the sum of the random errors.

Dose recovery tests

We conducted a series of dose recovery tests on seven of the samples to determine the optimum preheat (PH) temperatures to accurately construct dose response curves for individual grains in the laboratory. All grains were exposed to natural sunlight for at least 2 sunny days to empty their light-sensitive electron traps, and were then given a known laboratory dose (~40 Gy). Four different PH combinations were initially tried, where PH₁ is that given prior to measurement of L_N and L_x, and PH₂ is that given prior to measurement of T_N and T_x. The results are provided in Supplementary Table 3. Apart from a combination of PH₁ = 160°C/10 s and PH₂ = 160°C/5 s, none of the other PH combinations produced dose recovery ratios (i.e., ratios of measured to given dose) that deviated by more than 10% from unity. We used a PH₁ (220°C for 10 s) and PH₂ (160°C for 5 s) combination to measure the D_e values for all our samples, and made occasional checks on some samples using a PH₁ (260°C for 10 s) and PH₂ (160°C or 220°C for 5 s) combination for comparison of D_e values.

Rejection of grains

Using the experimental conditions described above, a total of 25,700 grains were measured from the 52 samples collected in 2012 and 2015 from Madjedbebe. Grains unsuitable for D_e determination were rejected using the quality assurance criteria described and tested previously (Jacobs et al., 2006). Supplementary Table 4 provides details of how many grains were rejected for each sample and the reasons for their rejection. After applying the rejection criteria, a total of 9,784 grains (38.1% of the total number measured) remained for D_e determination.

OSL decay curve and dose response curve characteristics of accepted grains

Extended Data Fig. 9m shows a selection of 10 decay curves from one sample (SW13A), following the test dose of ~10 Gy in the natural dose cycle, and a PH₂ temperature of 160°C for 5 s. The T_N decay curves represent the whole range of sensitivities and shapes observed for all 52 samples measured from Madjedbebe. The decay curves exhibit a range of shapes, but they are generally quite reproducible and decay rapidly to instrumental background, with less than about 5–10% of the signal remaining after 0.3 s of optical stimulation. Extended

Data Fig. 9n shows the corresponding dose response curves for the same 10 grains. The majority of these curves are very similar up to a dose of ~ 40 Gy – which is the dose range of interest for samples from Madjedbebe – after which some of the curves continue to grow with increasing dose while others begin to saturate.

Equivalent dose (D_e) determination and results

Information about the number of grains measured and used, the overdispersion (OD) values calculated for the D_e distributions, and the final D_e value $\pm 1\sigma$ error are presented in Supplementary Table 5 for each sample from the SW and NW sample series (in depth order). The corresponding information for the NE samples is presented in Supplementary Table 6.

The D_e values for grains from each of the samples ($N = 11$) associated with the lowest dense archaeological band and, hence, first phase of human occupation (between 2.60 and 2.15 m depth below surface) are displayed as radial plots in Extended Data Fig. 9a–k. D_e distributions for all samples from Madjedbebe have similar patterns (except for samples from the upper 30 cm, which show significant dispersion), as illustrated by sample NE1 in Extended Data Fig. 9l and are spread more widely than can be explained by measurement uncertainties alone. The single grain D_e distributions are overdispersed by between $27 \pm 2\%$ (NE8) and $90 \pm 7\%$ (NW1), but the samples associated with the lowest dense layer of artefacts have a much tighter distribution of D_e values, with OD values of between $31 \pm 2\%$ (SW10A) and $38 \pm 3\%$ (SW11A) (Supplementary Tables 5 and 6). We interpret the spread in D_e values to be predominantly the result of disturbance by soil fauna and flora, which may mix sediment through burrowing and root penetration; plant roots of various sizes are present throughout the deposit. In addition, the D_e values may be dispersed due to treadage by people to a depth of 5–10 cm, as observed at Madjedbebe from trampling experiments (Marwick et al., 2017) and the artefact refits reported in this paper (Methods and Extended Data Fig. 5), and as reported for other sites in the vicinity of Madjedbebe (Roberts et al., 1990b), in addition to micro-scale differences in the beta dose rate received by individual grains. We note that the deposits are fairly homogeneous, with little to no heavy minerals, feldspars or soil carbonates. There is no evidence in any of the D_e distributions for large-scale mixing or continuous, deep mixing of the sand grains over prolonged periods of time, as might be expected if, for example, termites had disturbed the deposit to a significant extent. It appears that the majority of sand grains have remained in primary deposition for most of their burial history. The central age model (CAM) was used to calculate the weighted mean D_e values for age determination, except for samples NW1 and NE1 (Extended Data Fig. 9l) that were both collected from the shell midden; the

minimum age model (MAM) was applied to the full D_e distributions of these two samples. The CAM (Galbraith et al., 1999; Galbraith and Roberts, 2012) assumes that the D_e values for all grains are centred on some average value of D_e (similar to the median) and the estimated standard error takes account of any D_e overdispersion (hence, the greater the overdispersion, the larger the error).

As some grains with both higher and lower D_e values might have been reworked after deposition (for the reasons given above), their D_e values could be removed from the datasets before calculating the weighted mean D_e values to improve the accuracy of the OSL ages. We used the median absolute deviation as a means of screening data for outliers (e.g., Rousseeuw and Croux, 1993; Rousseeuw et al., 2006). It attaches equal importance to positive and negative deviations from the sample median. After converting the D_e values (in Gy) to natural logarithms (Galbraith and Roberts, 2012), we calculated the normalised median absolute deviations (nMADs) using 1.4826 as the appropriate correction factor for a normal distribution, and rejected log D_e values with nMADs greater than 1.5 (Powell et al., 2002; Storey et al., 2012; Wood et al., 2016). The D_e values so identified as statistical outliers are shown as open triangles in each of the radial plots in Extended Data Fig. 9a–k; they amount to between about 25% (SW3A and SW2B) and 10% (NE4, NW13, SW14A and SW5B) of the total number of D_e values in each sample. Omitting these outliers can increase or decrease the weighted mean D_e values for the samples, but typically by up to a few percent only. The CAM D_e and outlier-rejected CAM D_e values are listed in Supplementary Table 7 for each sample, together with the ratios of these two values. The ratios range between 0.83 ± 0.04 (NW5) and 1.10 ± 0.06 (SW8C), with an average for all samples of 0.99 and standard deviation of 0.07; only sample NE1, collected from the late Holocene levels of the shell midden in the NE sample sequence, has a ratio that falls outside this range (0.32 ± 0.04).

A consequence of detecting and rejecting outliers is that the OD value for each sample is reduced. OD values including all D_e values for samples with scattered D_e distributions range between $27 \pm 2\%$ (NE8) and $90 \pm 7\%$ (NW1) (Supplementary Table 7), while the OD values for these same D_e distributions are reduced to between $14 \pm 1\%$ (SW13A) and $55 \pm 5\%$ (NW1) after excluding outliers. For samples from the lowest dense artefact layer, the OD values range from $14 \pm 1\%$ (SW13A) to $25 \pm 2\%$ (NW13 and SW4C) after outlier rejection (Supplementary Table 7), so the weighted mean D_e values are, consequently, more precise. This same approach was applied to the samples from Riwi rockshelter in the Kimberley region of Western Australia, where exceptional independent age control is provided by ^{14}C dating of charcoal from intact combustion features (Wood et al., 2016). It is worth noting that the D_e distributions for the

samples from the lowest dense artefact layer at Madjedbebe have similar or smaller OD values than those from the oldest levels at Riwi (~45 kyr), for which excellent agreement between OSL and ^{14}C ages was obtained. This comparison supports our case that the sediments at Madjedbebe have not been mixed significantly after deposition. We also note that where charcoal was collected from dating contexts other than combustion features at Riwi, significant dating anomalies were observed (Wood et al., 2016). This observation provides a cautionary reminder of the potential hazards involved in ^{14}C chronologies from isolated pieces of charcoal recovered from sandy deposits, in particular.

We also tested whether the MAM (Galbraith et al., 1999) could be applied to any of the D_e distributions after outlier rejection. This application represents a very conservative approach, in which artefacts are associated with the smallest- D_e grains in the distribution. This association may be true when artefacts or human activity (e.g., hearths or burials) are interred into the dated sediments. The 3-parameter MAM was run (after adding an additional 10% overdispersion to the standard error of each individual D_e value), and could be optimised for only 4 of the 52 samples measured. These 4 samples (NW2, NW3, SW3A and SW3B) are all from the upper ~85 cm of deposit, the p parameters of between 0.40 and 0.60 (representing the fraction of grains in each sample that is consistent with the minimum D_e value). We calculated the MAM D_e values for these samples, and they are presented alongside the CAM D_e values in Supplementary Table 5. As the ages obtained for these samples using the CAM or MAM D_e values are younger than 10 kyr, they have no influence on our estimate of age for the lowest two dense artefact layers.

Dose rate determination and results

The total environmental dose rate consists of contributions from beta, gamma and cosmic radiation external to the grains, plus a small alpha dose rate due to the radioactive decay of U and Th inclusions inside sand-sized grains of quartz. To calculate the OSL ages, we have assumed that the measured radionuclide activities and dose rates have prevailed throughout the period of sample burial. Secular equilibrium in the U and Th decay series was previously demonstrated by Roberts et al. (1990a) for sediment samples from the 1988 auger hole and adjacent 1989 excavation.

An internal alpha dose rate of 0.032 ± 0.010 Gy/kyr was assumed for all samples in this study. This is similar to the value calculated and used by Roberts et al. (1990a). We estimated the beta dose rates directly by low-level beta counting of dried, homogenised and powdered sediment samples in the laboratory, using a Risø GM-25-5 multi-counter system (Bøtter-Jensen

and Mejdahl, 1988). We prepared and measured samples, analysed the resulting data, and calculated the beta dose rates and their uncertainties following the procedures described and tested in Jacobs and Roberts (2015); six sub-samples were measured for each sample. For all samples, allowance was made for the effect of sample moisture content (Aitken, 1985), grain size (Mejdahl, 1979) and hydrofluoric acid etching (Bell and Zimmerman, 1978) on beta-dose attenuation. The beta dose rates are provided in Supplementary Tables 5 and 6 for all samples; they range between 0.20 ± 0.02 (NE5, NE7 and NE8) and 0.39 ± 0.02 (SW8C) Gy/kyr.

Gamma dose rates were measured directly by *in situ* gamma spectrometry to take into account any spatial heterogeneity in the gamma radiation field within 30 cm of each OSL sample (as gamma rays can penetrate this distance through most sediments and rocks). Counts were collected for 30 min with a 1-inch NaI(Tl) crystal, with a few samples measured for longer periods of time. The detectors were calibrated using the concrete blocks at Oxford University (Rhodes and Schwenninger, 2007) and the gamma dose rates were determined using the ‘threshold’ technique (Mercier and Falguères, 2007). This approach gives an estimate of the combined dose rate from gamma-ray emitters in the U and Th chains and from ^{40}K . We did not measure the gamma dose rate at every sampling location, because many of the samples were taken within 30 cm of each other. For samples situated between measurement locations, the weighted mean value of the two closest samples was used. The gamma dose rates are provided in Supplementary Tables 5 and 6 for all samples and range between 0.26 ± 0.01 (SW4A and SW14A) and 0.39 ± 0.02 (SW8C) Gy/kyr.

Account was also taken of the cosmic-ray contribution, which was adjusted for the average site altitude (~ 30 m), geomagnetic latitude (-23.5°), and the density and thickness of rock and sediment overburden (Prescott and Hutton, 1994); allowance was also made for the configuration of the rockshelter on the angular distribution of the cosmic-rays (Smith et al., 1993). Cosmic-ray dose rates range from 0.035 ± 0.005 Gy/kyr (for samples that are deepest and closest to the rock wall: Supplementary Table 6) to 0.091 ± 0.014 Gy/kyr (for samples that are shallowest and with little to no overhanging rock at the sample location: Supplementary Table 5). Owing to low beta and gamma dose rates, the cosmic-ray dose rate forms an unusually significant contribution to the total dose rate: $\sim 6\%$ for samples closest to the rock wall (NE sample series) and about 10–11% for samples near the front of the excavated area. Accordingly, calculations were made for each sample.

The beta, gamma and cosmic-ray dose rates were corrected for long-term water contents. We used a moisture content of $5 \pm 2\%$ for all samples. The field values current at the time of sample collection during the dry season are listed in Supplementary Tables 5 and 6,

and range from <1% to ~5%. The value used here is consistent with that used by Roberts et al. (1990a), who measured the sample porosity to estimate the saturated water content ($25 \pm 5\%$) of sediment samples from the site and assumed that they were saturated for $20 \pm 20\%$ of the period of burial, based on the duration of the wet season and the drainage characteristics of the sandy sediments. Taking these factors into account, an estimate of $5 \pm 1\%$ (i.e., a relative uncertainty of $\pm 20\%$ at 1σ) was adopted by Roberts et al. (1990a). In this study we used a more conservative estimate of $5 \pm 2\%$. The calculated total dose rates decrease, and the calculated OSL ages increase, by ~1% for each 1% increase in water content, so the ages are relatively insensitive to plausible variations in the long-term water content.

The total dose rates for the Madjedbebe samples show only a modest amount of variation, ranging between 0.57 ± 0.03 (SW14A) and 0.90 ± 0.04 (SW8C) Gy/kyr, with the samples from the lowest dense artefact layer near the front of the cave ranging between 0.64 ± 0.03 and 0.74 ± 0.03 Gy/kyr (Tables OSL_S5 and S6).

Age estimates and comparisons

The final OSL ages for all samples are listed in Supplementary Tables 5 and 6, together with the supporting D_e and dose rate estimates. Uncertainties on the ages are given at 1σ (the standard error on the mean) and were estimated by combining, in quadrature, all known and estimated sources of random and systematic error. Ages are also displayed on the photographs in Extended Data Fig. 8c–f. Reliable ages could be obtained for all 52 samples, ranging from <1 kyr to ~80 kyr for samples near the top and base of the excavated deposits, respectively. Ages for the ~45 cm-thick sediment layer (~2.15–2.60 m below surface) associated with the lowest dense artefact concentration near the front of the site (i.e., SW and NW sections) range from 65 ± 4 (SW2C) to 52 ± 3 (SW11A) kyr. In the NE section wall, the lowest dense artefact layer is bracketed by two samples with ages of 67 ± 4 (NE7) and 54 ± 3 (NE6) kyr, consistent with the age range for the SW and NW sequences (see Extended Data Fig. 8).

Single grain OSL and ^{14}C age comparisons

Extended Data Fig. 8g shows a comparison of OSL and ^{14}C ages obtained in this study for samples collected from the uppermost ~2 m of deposit. The calibrated ^{14}C ages for plotted pieces of charcoal are shown as red squares and those for charcoal collected from hearths as white triangles. The OSL ages are shown as black circles. All ages are plotted with their 2σ errors or 95.4% confidence intervals; for most of the ^{14}C ages, the symbols are the same size as or, larger than, the 95.4% confidence intervals.

Only three ^{14}C ages are available for deposits deeper than 1.45 m. The calibrated age range of 27.2–26.5 cal kyr BP for the deepest ^{14}C sample (OZT593), collected from a depth of 2 m, is significantly younger than the OSL age of 43.8 ± 2.1 kyr for sample NW10, which was collected from a similar depth (1.95 m) in the same square (C5). Sample OZT593 represents an isolated piece of charcoal not related to any hearth feature, and it was collected from a part of the deposit identified in the field as possibly disturbed. The two other deep samples (OZT592 and Wk43605) were collected from a depth of 1.62 m in adjacent squares (C5 and C4); they were pretreated using ABOx and ABA procedure, respectively and measured in different laboratories (Supplementary Table 2). OZT592 represents an isolated piece of charcoal and gave a calibrated age range of 34.4–33.8 cal kyr BP, which is consistent with OSL ages of 32.0 ± 2.0 and 33.4 ± 1.7 kyr for sample SW7A, collected from the same depth and adjacent square, and measured in two independent laboratories (UA and UOW: Extended Data Fig. 10l). Wk43605 was collected from a deep pit filled with charcoal (represented by one species of wood) and very large and steeply angled heat retainers and grindstones. The orientations of these rocks indicate that this hearth was part of a deep feature (pit) as rocks are not normally inclined vertically at Madjedbebe. Wk43605 gave an age range of 25.0–24.3 cal kyr BP, which is inconsistent with the age of OZT592 and the two OSL ages from the same depth. It is likely, therefore, that the age obtained for Wk43605, and the pit feature from which it was collected, represents charcoal derived from the overlying, younger deposits.

For samples between about 1.45 and 0.35 m depth, which span the period between about 27 and 4 kyr, there are no significant differences between the ^{14}C and OSL ages. In the uppermost 0.35 m of the deposit, few OSL samples were collected and the ^{14}C ages range between ~ 3 cal kyr BP and historical times. It can be seen from Extended Data Fig. 8g, that ^{14}C and OSL ages are in excellent agreement for the upper ~ 1.6 m of deposit, with only the two anomalous ^{14}C ages from the deeper deposits giving underestimates of the true age, for the reasons discussed above.

We refrain here from comparing the ^{14}C and OSL ages obtained in this study with the ^{14}C ages obtained from the 1973 and 1988/1989 studies, because the elevations of the ground surface relative to 2012/2015 are not known exactly and because the dating procedures used in the present study are an improvement on those used previously. Three of the charcoal samples dated previously were pretreated using ABOx-SC procedures, but only the fine charcoal fraction ($<125 \mu\text{m}$) was processed (Bird et al., 2002). Based on our observations and those of Wood et al. (2016) that isolated pieces of charcoal can move through the stratigraphy, we view the ABOx-pretreatment ages for fine-grained charcoal as unreliable.

A re-assessment of sediment samples dated previously from the lowest dense artefact layers

We re-measured the D_e values for four of the sediment samples examined by Roberts et al. (1990a, 1998) and Roberts and Jones (1994)—KTL165, KTL164, KTL158 and KTL162—which were retrieved from the archives at the University of Wollongong. The latter three samples had been collected from the so-called ‘zone of first occupation’ (Extended Data Fig. 10a), which coincides with the lowest dense artefact layer identified in the current study (Extended Data Fig. 3). Roberts et al. (1990a) reported TL ages for all four samples and later updated the age uncertainties (Roberts and Jones, 1994). Roberts et al. (1998) reported single aliquot and single grain OSL ages for two of these samples (KTL162 and KTL164). The D_e values were obtained from 90–125 μm -diameter quartz grains, whereas we have measured grains of 180–212 μm diameter in this study. A small difference ($\sim 2\text{--}3\%$) should be expected, therefore, for the D_e and dose rate values between the two studies, with the smaller grain-size having a higher D_e and corresponding dose rate because less of the beta dose is attenuated by the grains.

The single grain D_e distributions of the 4 samples re-measured in this study are shown in Extended Data Fig. 10b–e. They resemble the D_e distributions obtained for the other samples measured in this study (Extended Data Fig. 9a–l), so they have been treated analytically in an identical way to determine the final D_e values for age estimation; grains identified as statistical outliers using the nMAD criterion are shown as open triangles. Dose recovery test results for KTL162 are provided in Supplementary Table 3; the number of grains rejected for each of the samples is listed in Supplementary Table 4, along with the reasons for their rejection, and the final D_e and OD values calculated before and after outlier rejection are listed in Supplementary Table 7. We note the large ‘smear’ of smaller D_e values present in the D_e distribution of sample KTL158 (Extended Data Fig. 10d), which was collected using an auger; these grains are identified as statistical outliers (open triangles). We consider the lower D_e values to represent grains that were displaced by the auger as it was pushed down the hole and then dragged back up.

The TL, single aliquot OSL and single grain OSL D_e values obtained for these 4 samples by Roberts et al. (1990a, 1998) and Roberts and Jones (1994) are compared with the corresponding single grain OSL D_e values obtained in this study in Extended Data Fig. 10f. It is re-assuring that after more than 20 years, we can reproduce the previous results and obtain consistent D_e values, regardless of the method of measurements or data analysis.

We also revisited the dose rate calculations for these 4 samples. We were unable to locate the original raw or powdered samples and, therefore, could not measure them using the same procedures as used in the present study. Instead, we took the high-resolution gamma spectrometry data presented in Roberts et al. (1990a) and, for consistency with the samples in this study, recalculated the gamma and beta dose rates using updated dose rate conversion factors (Guérin et al., 2011) and correction factors for moisture content (Nathan and Mauz, 2008). This resulted in a negligible reduction of the gamma and beta dose rates by about 1-2%. We also recalculated the cosmic-ray dose rates for each of the samples to be consistent with the approach used in this study. Roberts et al. (1990a) assumed a fixed cosmic-ray dose rate of 0.15 ± 0.025 Gy/kyr, which is appropriate for sandy sediment overburden of ~ 2.5 m thickness and no rock. At Madjedbebe, allowance should be made for the angular distribution of cosmic rays penetrating through the sandstone rockshelter, as well as the sediment overburden (Smith et al., 1997). The recalculated cosmic-ray dose rates are 55–60% lower than the value used by Roberts et al. (1990a), resulting in a reduction in the total dose rates of 11–14% and an increase in the ages of 12–19% (numbers in parantheses in Extended Data Fig. 10f). Importantly, the revised dose rates and ages are consistent with those calculated for these samples in this study (Extended Data Fig. 10f).

The D_e values measured in this study for the four KTL samples, together with the revised dose rates are provided in Supplementary Table 5. For completeness, Supplementary Table 8 lists the revised dose rates and ages for all KTL samples presented in Roberts et al. (1990a, 1998) and Roberts and Jones (1994), including those not remeasured in this study. Four of these samples (KTL141, KTL167, KTL116 and KTL163) were collected from sterile sand deposits below the deepest sample measured in this study. The revised ages for the KTL samples are consistent with the new single grain OSL ages (~ 80 kyr) at a depth of ~ 2.8 m, increasing to ~ 100 kyr at 4 m depth and ~ 120 kyr at 4.5 m depth, the latter sample (KTL163) consisting of sand grains among the basal rubble.

An inter-laboratory comparison

We conducted a ‘blind’ inter-laboratory comparison test with L.J.A. at the University of Adelaide (UA). He was given no prior information about the samples, other than that they consisted of quartz grains extracted from an Australian archaeological deposit. He was provided with:

- prepared and acid-etched quartz grains from 4 samples—labelled as Sample 1, Sample 2, Sample 3 and Sample 4 to de-identify the samples and the site. They correspond to samples SW13A, SW11A, SW7A and SW5A, respectively;
- prepared and acid-etched quartz grains of each sample that had been sun-bleached for dose recovery experiments;
- sub-samples of powdered sediment of each sample for measurement of the gamma and beta dose rates at UA.

The UA blind comparisons were performed using the same OSL instrumentation and quality assurance criteria detailed in Arnold et al. (2013, 2016). Multi-grain OSL signals were determined from counts recorded in the first 0.4 s of each blue LED stimulation, after subtracting a mean background count from the final 10 s of stimulation. Single-grain OSL signals were calculated using the first 0.17 s of the OSL signal, minus a mean background count obtained from the last 0.25 s of each green laser stimulation. A single saturating exponential or single saturating exponential plus linear function was fitted to individual dose response curves for D_e determination.

L.J.A. conducted dose recovery tests on both single aliquots (~220 grains per aliquot) and single grains of quartz from Samples 1 and 3. A known dose of 40 Gy was administered to each grain or aliquot, and the dose measured using the SAR procedures shown in Supplementary Table 9. A series of dose recovery tests was first conducted on multi-grain aliquots using 6 different combinations of PH_1 (following the surrogate natural and regenerative doses) and PH_2 (following the test doses), with 3 aliquots at each combination. For the first 5 combinations, PH_1 was held constant at 260°C for 10 s and the PH_2 temperature was increased from 160°C to 220°C in increments of 20°C, held for 10 s at each temperature. An additional test was conducted with $PH_1 = 240^\circ\text{C}$ for 10 s and $PH_2 = 160^\circ\text{C}$ for 10 s. The measured/given dose ratios obtained in these tests ranged between 0.95 ± 0.03 and 0.99 ± 0.02 , with ratios closest to unity obtained for a PH_1 and PH_2 combination of 260°C for 10 s and 220°C for 10 s, respectively (mean ratio of 0.99 ± 0.02). A dose recovery test was conducted subsequently on 500 single grains of Samples 1 and 3, using the latter preheat combination, yielding a measured/given dose ratio of 1.03 ± 0.02 and an OD value of $11 \pm 2\%$ for Sample 1 ($N = 107$), and a ratio of 0.97 ± 0.02 and an OD value of $9 \pm 1\%$ for Sample 3 ($N = 148$).

The natural OSL signals of 500–800 grains were then measured for all four samples using this preheat combination and the single grain SAR procedure (Supplementary Table 9). Their own set of rejection criteria were then applied (Supplementary Table 10) Between 21 and 43% of measured grains were deemed suitable for D_e determination after applying the

quality assurance criteria shown in Supplementary Table 10. The D_e distributions for all accepted grains are displayed as radial plots in Extended Data Fig. 10g–j (where the UA data are shown as filled circles). The individual D_e uncertainties for these grains have been calculated using the same approach outlined earlier for the UoW single-grain D_e data sets (see Single grain OSL measurements and experimental details), with the exception that an empirically determined instrument reproducibility term of 2.5% was assigned to each OSL measurement made using the UA single-grain reader.

Since the two laboratories (UOW and UA) used different preheat temperatures to measure the samples, we remeasured these four samples at UOW using the UA preheat combination. The resulting D_e values are shown as open triangles in Extended Data Fig. 10g–j. The spread in D_e values is very similar for the data sets generated by the two different laboratories, with no evidence of significant bias. Extended Data Fig. 10k lists the number of grains, the weighted mean D_e values and the OD values (prior to outlier detection analysis) for all four samples, including the results obtained using the preferred preheat combination at UOW ($PH_1 = 220^\circ\text{C}$ for 10 s and $PH_2 = 160^\circ\text{C}$ for 5 s; combination ‘B’) that was used for the other samples in this study. The data are consistent between the two different laboratories for 3 of the samples with both preheat combinations, but Sample 2 shows a strong dependency of D_e with preheat temperature: preheat combination ‘A’ gives a weighted mean D_e value ~20% smaller than that obtained using preheat combination ‘B’. The dose recovery results for Sample 2 (SW11A) are acceptable using either preheat combination (Supplementary Table 3), but the measured/given dose rate closest to unity was obtained using combination ‘B’ (mean ratio of 0.98 ± 0.01 and OD value of $9 \pm 1\%$).

At UA, the dose rates for the 4 samples were measured using high-resolution gamma spectrometry to obtain concentrations of the following radionuclides: ^{238}U , ^{226}Ra and ^{210}Pb in the ^{238}U series, ^{228}Ra and ^{228}Th in the ^{232}Th series, and ^{40}K (Extended Data Fig. 10l). The uncertainties associated with each of these radionuclide activities are based on counting statistics and a 2% reproducibility/fitting uncertainty. The ^{238}U and ^{232}Th chains of all 4 samples are in secular equilibrium, consistent with the high-resolution gamma spectrometry data presented in Roberts et al. (1990a) for the KTL samples, which were collected from the same square as the UA samples. The beta and gamma dose rates estimated from these radionuclide concentrations and the conversion factors of Guérin et al. (2011, 2012) are listed in Extended Data Fig. 10l together with the beta and gamma dose rates obtained at UOW using GM-25-5 beta counting and field gamma spectrometry. The results from these independent methods are concordant, providing confidence in the reliability of the dose rate estimates.

Also shown in Extended Data Fig. 10l are the corresponding ages obtained by UA and UOW using the same preheat combination 'A'. The age estimates are consistent between the two different laboratories and with the ^{14}C ages obtained in this study. Sample 3 (SW7A) was collected from the same depth (~1.61 m below surface) as two ^{14}C samples: OZT592, a plotted charcoal piece from square C5 that has a calibrated ^{14}C age range of 34435–33820 cal yr BP (95.4% confidence interval); and sample Wk43605 from a hearth in square C4, which gave a calibrated ^{14}C age range of 24965–24335 cal yr BP (95.4% confidence interval). The two ^{14}C ages are not internally consistent, but the age of sample OZT592 is consistent with the OSL age estimates obtained for sample SW7A at both UA and UOW (32.0 ± 2.0 and 33.4 ± 1.7 kyr, respectively). Sample 4 (SW5A) was collected from the same depth (~1.22 m below surface) as ^{14}C sample OZT587, which was collected from a hearth feature in square C4, spit 26A, and pretreated using ABOx procedures. This charcoal sample has an age range of 21950–21520 cal yr BP (95.4% confidence interval), which is compatible with both the UA (22.7 ± 1.6 kyr) and UOW (21.0 ± 1.1 kyr) OSL age estimates (Extended Data Fig. 10l).

A single grain OSL Bayesian model

Fifty-three single grain OSL ages were put into a Bayesian statistical model on the OxCal platform (version 4.2.4) (Bronk Ramsey, 2009a; Bronk Ramsey and Lee, 2013); the measured ages are shown in light grey in Fig. 3. We did not include the samples measured from the NE sample column (Extended Data Fig. 8e), because there is a slope from the back of the site to the front, and the depth off-set with the samples collected from the SW and NW sequences is not known with sufficient precision for purposes of fitting a Bayesian model. The model included the two single grain ages obtained by Roberts et al. (1998) for KTL162 and KTL164 (recalculated using updated dose rate information; Extended Data Fig. 10f), which are shown in green, as well as the four ages for samples SW5A, SW7A, SW11A and SW13A obtained independently at UA, shown in blue.

Each OSL age was input as a C_date in calendar years before AD 1950 with an associated 1σ error; these are the so-called likelihood estimates. We treated the 4 replicate samples run at both UOW and UA as independent age estimates. These ages are truly independent: there are no correlated measurement parameters and they were obtained on different sets of grains from the same bulk sample. Ages should only be combined if they are true replicates. The statistics underpinning these arguments are presented in Ward and Wilson (1978) and Wilson and Ward (1981). OSL ages do not have fully independent uncertainties as many of the errors are common to all of the OSL ages (i.e., systematic errors). When combining

ages, only the random errors (given in parentheses in Supplementary Table 5) should be included in the model (Rhodes et al., 2003).

In the Bayesian model, the likelihood estimates are analysed with respect to prior information and the posterior distributions (i.e., modelled estimates) are estimated. A sequence of stratigraphic layers is often used as prior information. In the absence of clear stratigraphic layers at Madjedbebe, we instead used the depths associated with changes in artefact technology and peaks and dips in artefact concentration (Extended Data Fig. 2). The artefacts occur in 3 dense bands, with the intervening deposits containing few artefacts. Each band corresponds to a change in stone tool raw material and technology (Extended Data Fig. 2), and shows good internal stratigraphic integrity. The model was constructed using 7 separate bands, referred to as Phases in Fig. 3 (3 of the bands are associated with the dense artefact concentrations and 4 associated with the underlying, intervening and overlying deposits):

- band 1 is the archaeologically sterile sand at the base of the deposit (4.6–2.6 m depth);
- band 2 is the lowest dense artefact layer (2.6–2.15 m depth);
- band 3 represents a ~65 cm-thick layer of lower lithic abundance (2.1–1.55 m depth);
- band 4 is the middle dense artefact layer (1.55–0.95 m depth);
- band 5 represents a ~30 cm-thick layer of lowest lithic abundance (0.95–0.70 m depth);
- band 6 is the uppermost dense artefact layer (0.70–0.35 m depth) and the only phase with a similarly high lithic abundance as the lowest dense artefact layer; and
- band 7 represents the uppermost 35 cm of deposit, which consists mostly of shell midden and for which there is only a single OSL age (~2.9 kyr) from a depth of ~19 cm. The ^{14}C ages associated with the uppermost ~20 cm of deposit are all less than ~500 years, suggesting a significant break somewhere in this depth interval. We modelled bands 6 and 7 together as a single *Phase*, because of the low number of OSL samples ($N = 4$).

Each of the bands was modelled as a *Phase*, in which the measured ages associated with each of the bands are assumed to be unordered and uniformly distributed, so any mixing within an archaeological band will not influence the model. In Fig. 3, ages are presented in depth order for each of these phases, where the depth is the mid-point value for each sample. As some of the sample tubes have diameters of ~6 cm and, thus, straddle the boundary between two phases, a subjective decision was made as to which phase a sample should be assigned based on its age; a tolerance of 5–10 cm was allowed, which is similar to the likely thickness of the treadage zone (e.g., Roberts et al., 1990b; Marwick et al., 2017) and spans the entire diameter of the sample tube. The model is not sensitive to these phase-straddling sample assignments, but the

extent of convergence is higher with some assignments than others, including the final fit shown in Fig. 3.

A *Boundary* was placed at the start and end of each phase. The modelled probability distributions of these boundaries provide age estimates for the start and end date of each phase. These phases were arranged into a *Sequence*, assuming that the stratigraphically lowest phase is older than those above. A single interval, assumed to be 4000 ± 500 years in duration, was included between the end of phase 4 and the start of phase 5 to allow for a gap in the sequence, identified from the series of consistent OSL and ^{14}C ages at ~ 1.05 m depth and the pair of consistent OSL and ^{14}C ages at ~ 0.95 cm depth (Extended Data Fig. 8g). No samples were collected from the intervening ~ 10 cm. The posterior duration of the interval was modelled to be 3100–3985 years (68.2% probability) or 2655–4455 years (95.4% probability).

A *Difference* query was also included between the boundary estimates for each phase (see Supplementary Table 12) to calculate the duration of each phase in years. The purpose is to use the mean duration and corresponding 1σ uncertainty to calculate the mean sedimentation rate for each phase.

A *General t-type Outlier Model* (Bronk Ramsey, 2009b) was used to assess the likelihood of each age being consistent with the fitted model. Each age was assigned a prior outlier probability of 5%. The posterior outlier probability is calculated during the modelling process and the age down-weighted accordingly. For example, if the posterior probability is estimated as 5%, then the age is included in 95% of the model iterations; but an age with a posterior probability of 50% will be included in only 50% of the model iterations. We assigned a prior outlier probability of 100% to the single grain ages for KTL162 and KTL164 obtained by Roberts et al. (1998), which are shown in green in Fig. 3; the single grain ages for these two samples obtained in this study were included with an outlier probability of 5%. This was to prevent undue weighting on these two duplicate samples, given that the dose rates used for both sets of ages are identical. The latter does not apply to the ages for the four duplicate samples measured at the UOW and UA (shown in blue in Fig. 3), which were determined using independent estimates of D_e and dose rate.

The Bayesian modelled OSL chronology is presented in Fig. 3, with the data and model code provided in Supplementary Tables 11 and 12, respectively. All modelled age ranges were calculated at 68.2% and 95.4% posterior probability. The age likelihood (prior to modelling) and posterior (mathematically modelled) distributions are shown using pale and dark shading, respectively. The OSL ages show good consistency relative to each other and the stringent stratigraphic priors applied. The model identified only one age as having a 10% posterior

probability of being an outlier; the rest have posterior probabilities of 4–8% (Supplementary Table 11). The convergence values for all posterior distributions, including those for the start and end ages of each phase, the durations and the model as a whole, are excellent (greater than 95%).

The uncertainties associated with the start and end ages of each phase are all based on random uncertainties only (provided in parentheses in Supplementary Tables 5 and 6) and calculated using the OxCal platform. When the OSL ages for Madjedbebe are compared with independent chronologies, the total systematic uncertainty should also be included. These uncertainties are provided for individual ages in Supplementary Table 5 (i.e., those outside the parentheses). The total relative systematic uncertainty for all 52 samples is $3.35 \pm 0.03\%$ (mean \pm standard error (1σ); median is 3.37%), making up $\sim 45\%$ of the total (random plus systematic) uncertainty. To determine the total uncertainties associated with the start and end ages, we combined the total random and systematic errors in quadrature. In the discussion below, we give ages with two estimates of the total uncertainty (in parentheses) expressed at 95.4% probability: the first estimate is based on propagation of the random errors only, while the second also includes propagation of the systematic errors and is, therefore, the most appropriate value to use when comparing the OSL ages with independent chronologies.

The ^{14}C ages were not included in the Bayesian model primarily because the focus of this paper is on the lowest dense artefact band, which lies beyond the range of the ^{14}C chronology for Madjedbebe. Further modelling of the chronology for the upper phases could include the ^{14}C ages, which may result in improved confidence intervals, given the good correspondence between the ^{14}C and OSL ages for upper 1.4 m of deposit (Extended Data Fig. 8g).

An improved single grain OSL chronology for Madjedbebe

At Madjedbebe, high-resolution sampling of quartz-rich sediments for single grain OSL dating, combined with advances in OSL measurement technology and dating procedures (e.g., Jacobs and Roberts, 2007; Roberts et al., 2015), have resulted in more accurate and precise age estimates than those published previously for this site (Roberts et al., 1990a, 1998; Roberts and Jones, 1994; Clarkson et al., 2015). A ~ 2 m-thick archaeologically sterile sand unit (4.6–2.6 m below surface) underlies the first evidence for human occupation of the site. In this study, the deepest samples were collected from ~ 2.9 m below surface giving a start date for this phase of $80.2 \pm (7.2, 9.0)$ kyr, but sedimentation commenced at a depth of ~ 4.6 m below surface. The revised age estimates for the samples collected for TL dating from the basal deposits by Roberts

et al. (1990a) and Roberts and Jones (1994) (Supplementary Table 8) suggest that the sand apron started forming 121 ± 18 kyr (1σ) ago, around the time of the last interglacial. The end date of this phase was calculated to be $71.0 \pm (5.6, 7.3)$ kyr, which corresponds to a mean sediment accumulation rate of 4.0 ± 0.6 cm/kyr between 4.6 and 2.6 m depth. The uncertainty on this rate estimate is expressed at 68.2% probability and determined from the random errors only. This end date for Phase 1 also coincides with the transition from Marine Isotope Stage (MIS) 5 to 4, which may be significant as a palaeoclimatic control on the sand apron accumulation.

We found a few artefacts between about 3 and 2.6 m depth, but the first dense artefact band (Phase 2 in the Bayesian model) occurs between 2.6 and 2.15 m below surface. For this band, we obtained start and end ages of $65.0 \pm (3.7, 5.7)$ kyr and $52.7 \pm (2.4, 4.3)$ kyr, respectively, giving a mean sediment accumulation rate of 4.1 ± 0.8 cm/kyr over this depth interval. The latter was calculated from the modelled estimate of phase duration and the corresponding total random uncertainty at 68.2% probability, and the same procedure was used for all subsequent phases.

Phase 3 represents an archaeological unit, but with reduced artefact abundance. The modelled start age for this unit is of $51.6 \pm (2.4, 4.2)$ kyr, which is statistically consistent with the end age of Phase 2 and suggests no significant time gap in sediment deposition. Phase 3 ended $28.1 \pm (2.1, 2.8)$ kyr ago, suggesting a much slower rate of sediment accumulation over this period (2.6 ± 0.2 cm/kyr). The start of Phase 4 represents a slight increase in lithic abundance, but less abundant than in Phase 2. Phase 4 began $26.7 \pm (2.2, 2.8)$ kyr ago and ended $13.2 \pm (1.0, 1.3)$ kyr ago, which equates to a mean accumulation rate of 4.4 ± 0.4 cm/kyr during the lead up to and through the last glacial maximum. There appears to be a hiatus of 3.6 ± 0.9 kyr between Phases 4 and 5, coupled with a noticeable drop in artefact abundance associated with the latter, 25 cm-thick sedimentary unit (0.95–0.70 cm below surface; Extended Data Fig. 2). The modelled start and end ages for Phase 5 are $9.7 \pm (0.8, 1.1)$ and $8.0 \pm (1.0, 1.1)$ kyr, respectively, resulting in a mean sediment accumulation rate of 15.7 ± 7.4 cm/kyr over this period. Phase 6 represents a pulse of high lithic abundance in a 35 cm-thick band, which started $7.1 \pm (1.0, 1.1)$ kyr ago. Phases 6 and 7 are represented by only four relatively imprecise OSL ages, so they are not well constrained by OSL dating. However, a number of ^{14}C ages from Phase 7 suggest that this unit accumulated within the last 500 years and that a hiatus may exist between Phases 6 and 7.

Supplementary Table 3: Results for dose recovery tests using a range of different preheat (PH) combinations. Provided are the measured/given dose ratios at each PH combination for each sample, the overdispersion (OD) values calculated for each set of ratios, and the number of grains included in the estimate.

Sample	Measured/given dose ratios and overdispersion (OD) values (%)			
	PH ₁ = 160°C/10 s PH ₂ = 160°C/5 s	PH ₁ = 220°C/10 s PH ₂ = 160°C/5 s	PH ₁ = 260°C/10 s PH ₂ = 160°C/5 s	PH ₁ = 260°C/10 s PH ₂ = 220°C/5 s
SW5A	1.11 ± 0.01 OD = 6 ± 1 N = 95	0.98 ± 0.01 OD = 10 ± 1 N = 127	—	—
SW7A	—	0.99 ± 0.02 OD = 11 ± 2 N = 114	—	0.97 ± 0.02 OD = 9 ± 1 N = 96
SW9A	1.10 ± 0.01 OD = 18 ± 1 N = 207	0.98 ± 0.01 OD = 9 ± 1 N = 210	—	—
SW11A	1.14 ± 0.02 OD = 14 ± 1 N = 133	0.98 ± 0.01 OD = 9 ± 1 N = 180	0.97 ± 0.01 OD = 13 ± 1 N = 145	0.95 ± 0.01 OD = 12 ± 1 N = 152
SW13A	1.13 ± 0.02 OD = 14 ± 1 N = 154	0.98 ± 0.01 OD = 9 ± 1 N = 177	0.91 ± 0.01 OD = 8 ± 1 N = 175	1.02 ± 0.01 OD = 10 ± 1 N = 146
SW7C	1.07 ± 0.02 OD = 12 ± 1 N = 122	0.95 ± 0.01 OD = 9 ± 1 N = 145	1.00 ± 0.02 OD = 16 ± 1 N = 114	—
KTL162	1.07 ± 0.01 OD = 13 ± 1 N = 98	0.94 ± 0.01 OD = 7 ± 1 N = 129	0.95 ± 0.01 OD = 5 ± 1 N = 80	0.91 ± 0.01 OD = 0 N = 61

Supplementary Table 4: Number of single grains measured, rejected and accepted for each sample, together with the reasons for their rejection.

Sample name	No. of grains measured	T_N signal <3xBG	0 Gy dose >5% of L_N	Poor recycling ratio	No L_N/T_N intersection	Depletion by IR	Sum of rejected grains	Grains accepted for D_e determination
NE1	400	118	79	60	3	47	306	94
NE2	400	80	12	64	6	25	187	113
NE3	400	91	11	69	1	54	226	174
NE4	400	108	10	52	11	23	204	196
NE5	400	99	13	142	6	26	286	214
NE6	400	147	14	84	4	0	249	251
NE7	400	223	1	57	11	16	308	92
NE8	400	313	1	35	7	38	394	106
NW1	400	142	33	76	3	47	301	99
NW2	400	122	42	58	5	44	271	129
NW3	400	103	20	62	3	31	219	181
NW4	400	98	26	64	2	8	198	202
NW5	500	73	7	177	3	52	312	188
NW6	500	88	37	98	7	21	251	249
NW7	500	112	52	92	1	23	280	220
NW8	500	221	43	84	4	23	275	225
NW9	500	113	31	76	5	12	237	263
NW10	500	163	22	72	4	12	273	227
NW11	500	196	122	43	5	8	374	126
NW12	500	163	6	72	4	8	248	152
NW13	400	257	8	30	6	16	317	183
NW14	500	220	3	25	5	16	269	131
NW15	400	209	14	48	7	9	287	213
SW2A	400	74	31	116	5	9	235	165
SW3A	300	57	24	73	5	28	187	113
SW4A	400	69	38	93	3	20	223	177
SW5A	400	79	41	110	1	6	237	163
SW6A	300	47	26	77	4	6	160	140
SW7A	400	85	29	79	1	10	204	196
SW8A	500	184	23	67	8	24	306	194
SW9A	500	121	12	113	8	51	305	195
SW10A	500	176	6	96	7	24	309	191

Sample name	No. of grains measured	T_N signal <3 \times BG	0 Gy dose >5% of L_N	Poor recycling ratio	No L_N/T_N intersection	Depletion by IR	Sum of rejected grains	Grains accepted for D_e determination
SW11A	500	231	11	90	12	0	344	156
SW13A	500	283	5	71	7	0	366	134
SW14A	500	278	4	30	12	10	334	166
SW1B	400	85	32	83	9	11	222	178
SW2B	400	84	24	73	12	16	209	191
SW3B	400	71	46	123	6	4	250	150
SW4B	300	66	23	56	4	7	156	144
SW5B	400	118	22	52	11	15	218	182
SW6B	500	127	25	117	3	22	294	206
SW7B	500	138	26	74	5	5	248	252
SW8B	500	170	16	71	5	12	274	226
SW9B	500	176	8	76	11	47	318	182
NE1C	500	154	14	95	5	26	294	206
SW2C	500	238	6	51	8	28	331	169
SW3C	500	259	10	61	14	14	358	142
SW4C	500	233	4	100	9	42	388	112
SW5C	500	255	6	37	7	46	351	149
SW6C	500	245	5	83	8	23	364	136
SW7C	500	264	10	65	13	32	384	116
SW8C	500	310	2	65	8	23	408	92
KTL158	700	410	6	45	6	4	471	229
KTL162	1000	616	17	50	13	22	718	282
KTL164	900	527	5	61	11	16	620	280
KTL165	300	72	6	69	5	6	158	142

T_N is the OSL signal measured in response to the test dose given after measurement of the natural OSL signal.

L_N is the natural OSL signal.

Recycling ratio is the ratio of the sensitivity-corrected OSL signals measured from duplicate regenerative doses to test the efficacy of the test dose correction used in the SAR procedure. Grains are rejected if the ratio deviates from unity by more than $\pm 2\sigma$.

IR is the infrared stimulation used to empty any electron traps associated with IR-sensitive (e.g., feldspar) grains. Grains are rejected if the ratio is more than 2σ less than unity.

Supplementary Table 5: Dose rate data, equivalent doses (D_e) and overdispersion (OD) values, and OSL ages for sediment samples from the front of the site at Madjedbebe.

Sample	Depth below surface (m)	Water (%) [#]	Environmental dose rate (Gy/kyr)			D _e value (Gy) [§]	Number of grains*	OD (%) [§]	Age (kyr) [§]	
			Beta	Gamma	Cosmic					Total
SW7C	2.89	1.2	0.23 ± 0.02	0.37 ± 0.02	0.069	0.70 ± 0.03	55.4 ± 1.2	116/500 (99)	23 ± 2	79.0 ± 4.3 (3.3)
SW14A	2.75	<1	0.22 ± 0.02	0.26 ± 0.01	0.061	0.57 ± 0.03	46.8 ± 0.9	166/500 (150)	21 ± 2	81.6 ± 4.6 (3.7)
SW6C	2.74	<1	0.27 ± 0.02	0.27 ± 0.02	0.070	0.64 ± 0.03	49.8 ± 1.3	136/500 (116)	24 ± 2	77.6 ± 4.5 (3.7)
SW8C	2.71	<1	0.39 ± 0.02	0.39 ± 0.02	0.079	0.90 ± 0.04	63.2 ± 1.7	92/500 (78)	19 ± 2	70.4 ± 3.7 (2.9)
SW5C	2.62	<1	0.26 ± 0.02	0.31 ± 0.02	0.071	0.67 ± 0.03	48.5 ± 1.1	149/500 (130)	24 ± 2	72.7 ± 4.1 (3.3)
SW4C	2.54	<1	0.31 ± 0.02	0.31 ± 0.01	0.071	0.70 ± 0.03	44.1 ± 1.2	112/500 (100)	25 ± 2	62.7 ± 3.5 (2.7)
KTL162	2.52	—	0.25 ± 0.04	0.31 ± 0.05	0.063	0.66 ± 0.09	41.2 ± 0.6	282/1000 (226)	18 ± 1	62.3 ± 8.7
SW3C	2.50	<1	0.34 ± 0.02	0.30 ± 0.01	0.072	0.74 ± 0.03	47.1 ± 1.0	142/500 (116)	19 ± 2	64.0 ± 3.5 (2.5)
NW14	2.50	2.7	0.23 ± 0.02	0.31 ± 0.01	0.064	0.64 ± 0.03	40.3 ± 1.0	131/400 (108)	22 ± 2	62.8 ± 3.5 (2.7)
SW13A	2.45	<1	0.25 ± 0.02	0.31 ± 0.01	0.063	0.64 ± 0.03	39.8 ± 0.9	133/500 (114)	21 ± 2	62.6 ± 3.3 (2.6)
KTL158	2.44	—	0.27 ± 0.04	0.32 ± 0.04	0.064	0.68 ± 0.08	40.0 ± 0.7	229/700 (181)	23 ± 1	58.6 ± 7.2
SW2C	2.39	<1	0.30 ± 0.02	0.32 ± 0.01	0.073	0.72 ± 0.03	47.0 ± 0.9	169/500 (145)	20 ± 2	64.9 ± 3.3 (2.3)
NW13	2.37	4.0	0.26 ± 0.02	0.33 ± 0.01	0.068	0.69 ± 0.03	40.2 ± 0.9	183/500 (163)	25 ± 2	58.2 ± 3.1 (2.4)
NW12	2.29	<1	0.27 ± 0.02	0.33 ± 0.01	0.069	0.70 ± 0.03	38.7 ± 0.7	152/400 (128)	20 ± 2	55.5 ± 2.9 (2.2)
SW11A	2.28	<1	0.28 ± 0.02	0.35 ± 0.02	0.064	0.73 ± 0.03	46.0 ± 1.0	156/500 (121)	16 ± 2	63.4 ± 3.3 (2.6)
KTL164	2.28	—	0.32 ± 0.03	0.38 ± 0.03	0.066	0.80 ± 0.06	38.3 ± 0.7†	280/900 (240)	16 ± 2	51.7 ± 2.6 (2.0)
NW11	2.20	<1	0.29 ± 0.02	0.35 ± 0.02	0.072	0.74 ± 0.03	42.1 ± 0.6	126/500 (101)	21 ± 1	52.6 ± 4.4
SW10A	2.16	<1	0.32 ± 0.02	0.32 ± 0.01	0.065	0.73 ± 0.03	38.8 ± 0.8	191/500 (160)	17 ± 2	52.6 ± 2.7 (2.0)
NW9B	2.10	<1	0.25 ± 0.02	0.35 ± 0.02	0.075	0.71 ± 0.03	40.3 ± 0.6	182/500 (151)	18 ± 1	55.3 ± 2.6 (1.9)
NW15	2.07	<1	0.31 ± 0.03	0.35 ± 0.02	0.071	0.76 ± 0.03	40.0 ± 0.7	213/500 (175)	29 ± 1	56.7 ± 3.0 (2.3)
SW9A	2.03	<1	0.30 ± 0.02	0.33 ± 0.01	0.066	0.73 ± 0.03	36.8 ± 0.6	195/500 (164)	20 ± 1	48.4 ± 2.5 (1.9)
NE1B	2.02	1.1	0.26 ± 0.02	0.36 ± 0.02	0.085	0.73 ± 0.03	37.9 ± 0.7	206/500 (176)	21 ± 1	51.9 ± 2.6 (2.0)
NW10	1.95	<1	0.30 ± 0.02	0.36 ± 0.02	0.074	0.77 ± 0.03	38.7 ± 0.8	227/500 (196)	24 ± 2	53.0 ± 2.6 (1.9)
NW8B	1.94	<1	0.29 ± 0.02	0.34 ± 0.01	0.076	0.74 ± 0.03	33.5 ± 0.5	226/500 (194)	21 ± 1	43.8 ± 2.1 (1.6)
SW8A	1.81	<1	0.28 ± 0.02	0.33 ± 0.01	0.067	0.71 ± 0.03	34.3 ± 0.6	194/500 (166)	22 ± 1	46.3 ± 2.3 (1.8)
							30.4 ± 0.6		23 ± 1	42.8 ± 2.1 (1.6)

Sample	Depth below surface (m)	Water (%) [#]	Environmental dose rate (Gy/kyr)			D _e value (Gy) [§]	Number of grains*	OD (%) [§]	Age (kyr) ^{§§}
			Beta	Gamma	Cosmic				
NW9	1.75	<1	0.29 ± 0.02	0.36 ± 0.02	0.076	0.76 ± 0.03	263/500 (214)	24 ± 1	36.5 ± 1.8 (1.3)
SW7B	1.69	<1	0.24 ± 0.02	0.34 ± 0.01	0.079	0.70 ± 0.03	252/500 (208)	26 ± 1	39.3 ± 2.1 (1.6)
SW7A	1.61	<1	0.32 ± 0.02	0.33 ± 0.02	0.069	0.75 ± 0.03	196/400 (165)	26 ± 1	33.5 ± 1.6 (1.2)
NW8	1.53	4.7	0.33 ± 0.02	0.38 ± 0.02	0.078	0.82 ± 0.03	225/500 (187)	21 ± 1	28.1 ± 1.4 (1.1)
SW6B	1.47	<1	0.29 ± 0.03	0.37 ± 0.02	0.080	0.77 ± 0.04	206/500 (171)	24 ± 2	30.4 ± 1.7 (1.4)
KTL165	1.47	—	0.39 ± 0.05	0.46 ± 0.05	0.070	0.95 ± 0.10	142/300 (114)	29 ± 2	22.5 ± 2.6
SW6A	1.41	1.3	0.29 ± 0.02	0.37 ± 0.02	0.070	0.76 ± 0.03	140/300 (113)	21 ± 2	27.3 ± 1.4 (1.1)
NW7	1.34	4.6	0.33 ± 0.02	0.38 ± 0.02	0.079	0.82 ± 0.03	221/500 (184)	23 ± 1	23.8 ± 1.1 (0.9)
SW5B	1.25	<1	0.27 ± 0.02	0.37 ± 0.02	0.083	0.75 ± 0.03	182/400 (166)	42 ± 2	23.0 ± 1.3 (1.0)
SW5A	1.22	2.5	0.31 ± 0.02	0.37 ± 0.02	0.072	0.79 ± 0.03	163/400 (134)	23 ± 2	22.0 ± 1.1 (0.8)
NW6	1.16	<1	0.29 ± 0.02	0.37 ± 0.02	0.081	0.77 ± 0.03	249/500 (201)	23 ± 1	21.2 ± 1.0 (0.7)
SW4B	1.04	<1	0.25 ± 0.02	0.35 ± 0.02	0.085	0.72 ± 0.03	144/300 (122)	28 ± 2	14.7 ± 0.8 (0.6)
SW4A	1.04	<1	0.22 ± 0.02	0.26 ± 0.01	0.073	0.58 ± 0.03	177/400 (151)	29 ± 2	14.9 ± 0.9 (0.7)
NW5	0.95	4.5	0.24 ± 0.02	0.36 ± 0.02	0.083	0.71 ± 0.03	188/500 (156)	32 ± 2	12.8 ± 0.7 (0.5)
SW3B	0.85	<1	0.28 ± 0.02	0.33 ± 0.01	0.087	0.73 ± 0.04	150/400 (121)	21 ± 2	11.3 ± 0.7 9.9 ± 0.6 (0.5)
SW3A	0.85	1.1	0.23 ± 0.02	0.33 ± 0.01	0.075	0.67 ± 0.03	113/300 (86)	20 ± 2	11.2 ± 0.6 9.9 ± 0.5 (0.4)
NW4	0.74	2.9	0.22 ± 0.02	0.26 ± 0.01	0.085	0.59 ± 0.03	202/400 (176)	27 ± 2	8.7 ± 0.7 (0.6)
SW2B	0.68	<1	0.28 ± 0.02	0.33 ± 0.01	0.088	0.73 ± 0.03	191/400 (145)	35 ± 2	8.1 ± 0.4 (0.3)
SW2A	0.66	1.1	0.23 ± 0.02	0.32 ± 0.01	0.076	0.66 ± 0.03	165/400 (133)	22 ± 2	8.9 ± 0.5 (0.4)
NW3	0.54	3.0	0.24 ± 0.02	0.35 ± 0.01	0.087	0.71 ± 0.03	181/400 (150)	28 ± 2	7.9 ± 0.4 (0.3) 6.1 ± 0.4 (0.3)
SW1B	0.49	<1	0.30 ± 0.02	0.36 ± 0.02	0.090	0.78 ± 0.03	178/400 (144)	33 ± 2	6.4 ± 0.3 (0.3)
NW2	0.33	1.6	0.32 ± 0.02	0.35 ± 0.02	0.089	0.79 ± 0.03	129/400 (102)	27 ± 2	5.5 ± 0.3 4.1 ± 0.3 (0.3)
NW1	0.19	4.4	0.32 ± 0.02	0.38 ± 0.02	0.091	0.83 ± 0.03	96/400 (81)	55 ± 5	2.9 ± 0.2 (0.2)

[#] Current measured water contents of the sediment samples. A value of 5 ± 2% was used for all samples as an estimate of the long-term water content in calculations of dose rate.

[§]D_e values for all samples were obtained using the central age model (CAM, C), except for NW1, NW2, NW3, SW3A and SW3B where the minimum age model (MAM, M) values are also provided.

^{§§}Number of grains accepted for De determination / total number of grains measured. Numbers in brackets represent the number of grains included in the CAM D_e value after identification and rejection of outlier grains using the normalised median absolute deviation (nMAD) criterion.

[&]The D_e and OD values are for the D_e distributions after outlier rejection. The corresponding D_e and OD values for the samples including these outliers are provided in Supplementary Table 7.

[†]This sample was measured using a preheat combination of 260°C for 10 s (PH_1) and 220°C for 0 s (PH_2); see text in Supplementary Information for details.

[#]Ages in italics are the preferred ages.

[§]The uncertainties provided in parentheses are the random-only uncertainties; those provided after the \pm symbol represent the full (random plus systematic) uncertainty at 1σ .

[!]Samples for which gamma dose rates were not directly measured in the field.

Supplementary Table 6: Dose rate data, equivalent doses (D_e) and overdispersion (OD) values, and OSL ages for sediment samples from the NE sample series at Madjedbebe.

Sample	Depth below surface (m)	Water (%) [§]	Environmental dose rate (Gy/kyr)			D_e value (Gy) ^{#,&}	Number of grains*	OD (%) ^{&}	Age (kyr) [†]
			Beta	Gamma	Cosmic				
NE8	-2.4	1.1	0.20 ± 0.02	0.31 ± 0.01	0.035	0.58 ± 0.03	106/400 (84)	16 ± 2	78.6 ± 4.2 (3.4)
NE7	-2.10	<1	0.20 ± 0.02	0.31 ± 0.01	0.036	0.58 ± 0.03	92/400 (77)	24 ± 2	67.1 ± 4.0 (3.4)
NE6	-1.80	3.0	0.25 ± 0.02	0.34 ± 0.01	0.037	0.66 ± 0.03	251/400 (212)	20 ± 1	53.6 ± 2.6 (2.0)
NE5	-1.50	<1	0.20 ± 0.02	0.33 ± 0.01	0.039	0.60 ± 0.03	214/400 (182)	21 ± 1	41.6 ± 2.3 (1.7)
NE4	-1.2	<1	0.27 ± 0.02	0.33 ± 0.01	0.040	0.67 ± 0.03	196/400 (173)	32 ± 2	30.4 ± 1.6 (1.4)
NE3	-0.90	<1	0.28 ± 0.02	0.34 ± 0.01	0.041	0.69 ± 0.03	174/400 (152)	42 ± 3	16.1 ± 0.9 (0.8)
NE2	-0.60	<1	0.28 ± 0.02	0.35 ± 0.02	0.043	0.70 ± 0.03	113/400 (91)	33 ± 3	10.9 ± 0.6 (0.5)
NE1	-0.30	2.8	0.34 ± 0.02	0.37 ± 0.02	0.044	0.78 ± 0.03	93/400 (93)	94 ± 6	0.80 ± 0.09 (0.08)

[#] Current measured water contents of the sediment samples. A value of 5 ± 2% was used for all samples as an estimate of the long-term water content in calculations of dose rate.

[§] D_e values for all samples were obtained using the central age model (CAM), except for NE1 where the minimum age model (MAM) was applied to the full D_e distribution.

* Number of grains accepted for D_e determination / total number of grains measured. Numbers in brackets represent the number of grains included in the CAM D_e value after identification and rejection of outlier grains using the normalised median absolute deviation (nMAD) criterion.

[&] The D_e and OD values are for the D_e distributions after outlier rejection. The corresponding D_e and OD values for the samples including these outliers are provided in Supplementary Table 7.

[†] The uncertainties provided in brackets are the random-only uncertainties; those provided after the ± symbol represent the full (random plus systematic) uncertainty at 1 σ .

Supplementary Table 7: Weighted mean D_e and overdispersion (OD) values for each sample under two different scenarios: (a) including all D_e values for each sample, or (b) after rejecting D_e values identified as statistical outliers based on them having $\log D_e$ values with normalised median absolute deviations (nMADs) greater than 1.5. Also provided in the final column is the ratio of the latter to the former weighted mean D_e values.

Sample	(a) All values included			(b) After outlier rejection			D_e ratios (b)/(a)
	N	D_e (Gy)	OD (%)	N	D_e (Gy)	OD (%)	
NE8	106	44.9 ± 1.3	27 ± 2	84	45.7 ± 1.0	16 ± 2	1.02 ± 0.04
NE7	92	39.4 ± 1.6	37 ± 3	77	39.2 ± 1.2	24 ± 2	0.99 ± 0.05
NE6	251	34.4 ± 0.7	32 ± 2	212	35.2 ± 0.5	20 ± 1	1.02 ± 0.03
NE5	214	24.6 ± 0.5	30 ± 2	182	24.9 ± 0.4	21 ± 1	1.01 ± 0.03
NE4	196	20.1 ± 0.7	44 ± 2	173	20.5 ± 0.5	32 ± 2	1.02 ± 0.04
NE3	174	12.3 ± 0.5	55 ± 3	152	11.2 ± 0.4	42 ± 3	0.91 ± 0.05
NE2	113	8.9 ± 0.5	60 ± 4	91	7.6 ± 0.3	33 ± 3	0.86 ± 0.06
NE1	93	1.9 ± 0.2	94 ± 6	93	0.6 ± 0.1	94 ± 6	0.32 ± 0.04
NW14	131	41.1 ± 1.4	36 ± 2	108	40.3 ± 1.0	22 ± 2	0.98 ± 0.04
NW13	183	39.6 ± 1.1	38 ± 2	163	40.2 ± 0.9	25 ± 2	1.02 ± 0.04
NW12	152	39.9 ± 1.2	34 ± 2	128	38.7 ± 0.7	20 ± 1	0.97 ± 0.03
NW11	126	38.4 ± 1.1	32 ± 2	101	38.8 ± 0.8	17 ± 2	1.01 ± 0.04
NW15	213	35.7 ± 0.9	35 ± 2	175	36.8 ± 0.6	20 ± 1	1.03 ± 0.03
NW10	227	32.4 ± 0.7	33 ± 2	196	33.5 ± 0.5	21 ± 1	1.03 ± 0.03
NW9	263	27.2 ± 0.7	43 ± 2	214	27.7 ± 0.5	24 ± 1	1.02 ± 0.03
NW8	225	22.6 ± 0.5	35 ± 2	187	23.2 ± 0.4	21 ± 1	1.03 ± 0.03
NW7	221	19.1 ± 0.5	38 ± 2	184	19.5 ± 0.3	23 ± 1	1.02 ± 0.03
NW6	249	16.1 ± 0.4	41 ± 2	201	16.3 ± 0.3	23 ± 1	1.01 ± 0.03
NW5	188	11.0 ± 0.5	57 ± 3	156	9.2 ± 0.2	32 ± 2	0.83 ± 0.04
NW4	202	7.5 ± 0.2	42 ± 2	176	7.0 ± 0.2	27 ± 2	0.93 ± 0.04
NW3	181	6.5 ± 0.3	57 ± 3	150	5.6 ± 0.1	27 ± 2	0.86 ± 0.04
NW2	129	4.5 ± 0.3	62 ± 4	102	4.4 ± 0.1	26 ± 2	0.97 ± 0.06
NW1	96	2.2 ± 0.2	90 ± 7	81	2.4 ± 0.2	55 ± 5	1.07 ± 0.12

Sample	(a) All values included				(b) After outlier rejection				D_e ratios (b)/(a)
	N	D_e (Gy)	OD (%)	N	D_e (Gy)	OD (%)	D_e ratios (b)/(a)		
SW14A	166	47.6 ± 1.2	31 ± 2	150	46.8 ± 0.9	21 ± 2	0.98 ± 0.03		
SW13A	134	40.9 ± 1.2	31 ± 2	114	39.8 ± 0.9	21 ± 2	0.97 ± 0.04		
SW11A	156	36.7 ± 1.2	37 ± 2	121	38.3 ± 0.7	16 ± 2	1.03 ± 0.04		
SW10A	191	39.9 ± 0.9	31 ± 2	160	40.3 ± 0.6	18 ± 1	1.01 ± 0.03		
SW9A	195	36.1 ± 1.0	36 ± 2	164	37.9 ± 0.7	21 ± 1	1.05 ± 0.03		
SW8A	194	29.5 ± 0.8	36 ± 2	166	30.4 ± 0.6	23 ± 1	1.03 ± 0.03		
SW7A	196	24.7 ± 0.8	45 ± 2	165	25.1 ± 0.5	26 ± 2	1.02 ± 0.04		
SW6A	140	21.4 ± 0.7	37 ± 2	113	20.8 ± 0.4	21 ± 2	0.97 ± 0.04		
SW5A	163	17.1 ± 0.6	43 ± 2	134	17.4 ± 0.4	23 ± 2	1.02 ± 0.04		
SW4A	177	9.6 ± 0.3	45 ± 2	151	8.7 ± 0.2	29 ± 2	0.91 ± 0.04		
SW3A	113	8.1 ± 0.3	44 ± 3	86	7.6 ± 0.2	20 ± 2	0.93 ± 0.05		
SW2A	165	6.9 ± 0.2	45 ± 3	133	6.5 ± 0.1	22 ± 2	0.94 ± 0.04		
SW7C	116	52.3 ± 1.9	49 ± 3	99	55.4 ± 1.2	23 ± 2	1.06 ± 0.04		
SW6C	136	46.0 ± 1.8	44 ± 3	116	49.8 ± 1.3	24 ± 2	1.08 ± 0.05		
SW8C	92	57.4 ± 3.0	47 ± 4	78	63.2 ± 1.7	19 ± 2	1.10 ± 0.06		
SW5C	149	46.5 ± 1.5	36 ± 2	130	48.5 ± 1.1	24 ± 2	1.04 ± 0.04		
SW4C	112	44.6 ± 1.6	36 ± 3	100	44.1 ± 1.2	25 ± 2	0.99 ± 0.04		
SW3C	142	43.9 ± 1.5	38 ± 2	116	47.1 ± 0.9	19 ± 2	1.07 ± 0.04		
SW2C	169	44.4 ± 1.3	36 ± 2	145	47.0 ± 0.9	20 ± 2	1.06 ± 0.04		
NW9B	182	39.1 ± 1.1	36 ± 2	151	40.0 ± 0.7	20 ± 1	1.02 ± 0.03		
NE1B	206	35.7 ± 1.1	41 ± 2	176	38.7 ± 0.8	24 ± 2	1.08 ± 0.04		
NW8B	226	34.4 ± 0.8	34 ± 2	194	34.3 ± 0.6	22 ± 1	1.00 ± 0.03		
SW7B	252	27.0 ± 0.7	43 ± 2	208	27.4 ± 0.5	26 ± 1	1.02 ± 0.03		
SW6B	206	23.4 ± 0.7	41 ± 2	171	23.4 ± 0.5	24 ± 2	1.00 ± 0.04		
SW5B	182	18.3 ± 0.7	51 ± 3	166	17.3 ± 0.6	42 ± 2	0.95 ± 0.05		
SW4B	144	11.7 ± 0.5	48 ± 3	122	10.5 ± 0.3	28 ± 2	0.90 ± 0.04		
SW3B	150	9.4 ± 0.3	42 ± 3	121	8.2 ± 0.2	21 ± 2	0.87 ± 0.04		
SW2B	191	8.0 ± 0.3	54 ± 3	145	7.2 ± 0.2	35 ± 2	0.90 ± 0.05		

Sample	(a) All values included			(b) After outlier rejection			D_e ratios (b)/(a)
	N	D_e (Gy)	OD (%)	N	D_e (Gy)	OD (%)	
SW1B	178	6.1 ± 0.3	69 ± 4	144	5.0 ± 0.1	32 ± 2	0.82 ± 0.05
KTL162	282	43.3 ± 1.0	36 ± 2	226	41.2 ± 0.6	18 ± 1	0.95 ± 0.03
KTL158	229	36.8 ± 1.4	57 ± 3	181	40.0 ± 0.7	23 ± 1	1.09 ± 0.05
KTL164	280	41.3 ± 0.9	33 ± 2	240	42.1 ± 0.6	21 ± 1	1.02 ± 0.03
KTL165	142	20.8 ± 0.8	45 ± 3	114	21.4 ± 0.6	29 ± 2	1.03 ± 0.05

Supplementary Table 8: Dose rate data, equivalent dose (D_e) values and revised age estimates and depths for samples presented in Roberts et al. (1990a, 1998) and Roberts and Jones (1994).

Sample	Depth below surface (m)	Environmental dose rate (Gy/kyr)			Total	D_e value (Gy) [#]	Age (kyr)
		Beta	Gamma	Cosmic			
KTL165	1.44–1.50	0.42 ± 0.05	0.46 ± 0.05	0.073	0.98 ± 0.11	17 ± 2 (TL)	17 ± 3
KTL97	1.86–2.05	0.35 ± 0.05	0.40 ± 0.05	0.070	0.86 ± 0.10	24 ± 3 (TL)	28 ± 5
KTL164	2.24–2.31	0.34 ± 0.03	0.38 ± 0.03	0.066	0.82 ± 0.07	42 ± 4 (TL) 42 ± 1 (SA OSL) 40 ± 2 (SG OSL)	51 ± 7 51 ± 4 49 ± 5
KTL158	2.38–2.51	0.28 ± 0.04	0.32 ± 0.04	0.064	0.70 ± 0.08	42 ± 4 (TL)	60 ± 9
KTL162	2.50–2.55	0.27 ± 0.04	0.31 ± 0.05	0.063	0.67 ± 0.09	48 ± 5 (TL) 47 ± 1 (SA OSL) 43 ± 4 (SG OSL)	71 ± 12 70 ± 10 64 ± 11
KTL141	2.91–3.10	0.34 ± 0.05	0.31 ± 0.05	0.062	0.74 ± 0.11	56 ± 6 (TL)	76 ± 14
KTL167	3.26–3.57				0.80 ± 0.10 [§]	75 ± 8 (TL)	94 ± 15
KTL116	3.86–4.05	0.38 ± 0.05	0.39 ± 0.05	0.055	0.86 ± 0.10	85 ± 9 (TL)	99 ± 16
KTL163	4.47–4.55	0.50 ± 0.05	0.51 ± 0.06	0.050	1.09 ± 0.11	132 ± 13 (TL)	121 ± 18

[#]TL, thermoluminescence; SA OSL, single-aliquot OSL; SG OSL, single-grain OSL.

[§]The dose rate for this sample was not measured. It represents the mean of the dose rates for samples KTL141 and KTL116.

Supplementary Table 9: Single-aliquot regenerative-dose (SAR) procedures used for dose-recovery measurements and D_e determination at the University of Adelaide. Each of these SAR measurement cycles was repeated for the natural dose, 5 different sized regenerative doses and a 0 Gy regenerative dose (to measure OSL signal recuperation). Both the smallest and largest non-zero regenerative doses were repeated as additional measurement cycles at the end of the SAR procedure to assess the suitability of the test-dose sensitivity correction. In the case of the single-grain OSL SAR procedure, the smallest regenerative dose was repeated a second time as an additional measurement cycle, with the inclusion of step 2 to check for the presence of feldspar contaminants using the OSL–IR depletion ratio of Duller (2003).

Multi-grain single-aliquot OSL SAR procedure			Single-grain OSL SAR procedure		
Step	Treatment	Signal	Step	Treatment	Signal
1	Dose (Natural or laboratory)		1	Dose (Natural or laboratory)	
2	IRSL stimulation (50°C for 60 s)		2 ^a	IRSL stimulation (50°C for 60 s)	
3	PH ₁ (x°C for 10 s)		3	PH ₁ (260°C for 10 s)	
4	OSL stimulation (125°C for 60 s)	L _N or L _x	4	Single-grain OSL stimulation (125°C for 2 s)	L _N or L _x
5	Test dose (5 Gy)		5	Test dose (5 Gy)	
6	IRSL stimulation (50°C for 60 s)		6	PH ₂ (220°C for 10 s)	
7	PH ₂ (x°C for 10 s)		7	Single-grain OSL stimulation (125°C for 2 s)	T _N or T _x
8	OSL stimulation (125°C for 60 s)	T _N or T _x	8	Repeat measurement cycle for different sized regenerative doses	
9	Repeat measurement cycle for different sized regenerative doses				

^a Step 2 is only included in the single-grain SAR procedure when measuring the OSL – IR depletion ratio (Duller, 2003).

Supplementary Table 10: Grain classification statistics for the blind comparison samples measured at the University of Adelaide. The number and proportion of grains rejected prior to D_e estimation are listed for each of the SAR quality assurance criteria applied in this study. These criteria were applied to each single-grain measurement in the order listed. T_n = natural test-dose signal response; L_n/T_n = sensitivity-corrected natural signal response; L_x/T_x = sensitivity-corrected regenerative-dose signal response; I_{max} = saturation OSL intensity of the fitted dose response curve.

Sample number	Sample 1	Sample 1	Sample 2	Sample 3	Sample 3	Sample 4
SAR measurement type	D_e	Dose-recovery	D_e	D_e	Dose-recovery	D_e
Total number of measured grains (n)	800	500	800	600	500	500
Reason for rejecting grains prior to D_e analysis (% measured grains):						
$T_n < 3\sigma$ background	38	40	30	12	9	7
Low-dose recycling ratio $\neq 1$ at $\pm 2\sigma$	18	15	17	22	26	23
High-dose recycling ratio $\neq 1$ at $\pm 2\sigma$	10	8	12	16	14	13
OSL IR depletion ratio < 1 at $\pm 2\sigma$	4	5	4	4	5	4
0 Gy $L_x/T_x > 5\% L_n/T_n$	<1	<1	<1	3	2	6
Non-intersecting grains ($L_n/T_n > \text{dose response curve } I_{max} \text{ at } \pm 2\sigma$)	0	0	<1	<1	0	0
Saturated grains ($L_n/T_n = \text{dose response curve } I_{max} \text{ at } \pm 2\sigma$)	<1	0	<1	<1	0	0
Extrapolated grains ($L_n/T_n > \text{highest } L_x/T_x \text{ on dose response curve at } \pm 2\sigma$)	<1	<1	<1	0	0	0
Anomalous dose response / unable to perform Monte Carlo fit	8	10	10	4	14	4
Sum of rejected grains (%)	78	79	74	62	70	57
Sum of accepted grains (%)	22	21	26	39	30	43

Supplementary Table 11: OSL age ranges and modelled age estimates (years ago) at 68.2% and 95.4% probabilities using OxCal program v.4.2.4 and model parameters. The modelled durations (years) for Phases 2–5 are shown in italics.

Sample name	Unmodelled age range (yrs)				Modelled age range (yrs)				Outlier data		Convergence
	68.2% probability from	68.2% probability to	95.4% probability from	95.4% probability to	68.2% probability from	68.2% probability to	95.4% probability from	95.4% probability to	prior	posterior	
End of Phase 7					3,100	1,430	3,410	-1,710			99.6
NW1	3,110	2,690	3,310	2,490	3,160	2,730	3,400	2,490	5	5	99.7
NW2	4,350	3,840	4,610	3,590	4,360	3,840	4,630	3,570	5	4	99.6
NW1B	6,630	6,100	6,890	5,840	6,560	6,050	6,830	5,780	5	4	99.6
NW3	6,440	5,800	6,760	5,490	6,400	5,780	6,700	5,450	5	4	99.6
Start of Phase 6					7,410	6,340	8,180	6,090			99.8
<i>Duration of Phase 5</i>											
					<i>840</i>	<i>2,340</i>	<i>2</i>	<i>2,860</i>			<i>99.5</i>
End of Phase 5					8,640	7,690	9,020	7,080			99.7
SW2A	9,210	8,510	9,560	8,160	9,180	8,570	9,490	8,260	5	4	99.9
SW2B	8,420	7,760	8,750	7,430	8,770	8,080	9,120	7,720	5	6	99.7
NW4	9,350	8,010	10,020	7,350	9,280	8,390	9,700	7,910	5	4	99.9
SW3A	10,360	9,490	10,790	9,060	9,740	8,990	10,130	8,640	5	6	99.8
SW3B	10,370	9,330	10,890	8,820	9,680	8,880	10,090	8,540	5	5	99.8
Start of Phase 5					10,080	9,250	10,530	8,850			99.6
<i>Duration of Phase 4</i>											
					<i>12,390</i>	<i>14,770</i>	<i>11,100</i>	<i>15,950</i>			<i>99.5</i>
End of Phase 4					13,670	12,730	14,210	12,210			99.6
NW5	13,350	12,320	13,870	11,800	13,970	13,040	14,890	12,360	5	10	98.9
SW4A	15,640	14,220	16,340	13,510	15,650	14,250	16,350	13,590	5	4	99.3
SW4B	15,300	14,090	15,910	13,480	15,320	14,100	15,910	13,550	5	4	99.2
NW6	21,870	20,450	22,580	19,740	21,910	20,430	22,630	19,690	5	5	99.0
SW5A(UA)	24,260	21,280	25,750	19,800	24,270	21,290	25,620	19,810	5	5	98.6
SW5A(UOW)	22,810	21,240	23,590	20,460	22,830	21,190	23,630	20,430	5	5	98.8
SW5B	24,060	21,990	25,090	20,960	24,090	21,970	25,050	20,930	5	5	98.9
NW7	24,770	22,870	25,710	21,920	24,770	22,820	25,660	21,860	5	5	98.9

Sample name	Unmodelled age range (yrs)				Modelled age range (yrs)				Outlier data		Convergence
	68.2% probability from	68.2% probability to	95.4% probability from	95.4% probability to	68.2% probability from	68.2% probability to	95.4% probability from	95.4% probability to	prior	posterior	
SW6A	28,380	26,270	29,430	25,220	27,050	25,060	28,190	23,730	5	9	98.4
Start of Phase 4					27,860	25,710	28,920	24,560			99.7
<i>Duration of Phase 3</i>											
End of Phase 3					21,880	25,090	20,300	26,750			99.5
SW6B	31,730	29,030	33,070	27,680	29,130	27,120	30,110	26,000			99.7
NW8	29,110	27,170	30,080	26,210	31,790	29,260	33,070	28,180	5	5	98.8
SW7A(UA)	34,120	30,250	36,040	28,330	29,870	28,070	30,810	27,160	5	5	98.7
SW7A(UOW)	34,690	32,250	35,910	31,030	34,050	30,340	35,950	28,750	5	5	98.2
SW7B	37,840	35,190	39,160	33,870	34,730	32,230	35,950	30,980	5	5	98.7
NW9	40,750	38,100	42,070	36,780	37,890	35,140	39,230	33,830	5	5	98.5
SW8A	44,340	41,210	45,900	39,650	40,790	38,040	42,110	36,720	5	5	98.4
NW8B	48,110	44,590	49,870	42,830	44,410	41,170	45,940	39,580	5	6	98.2
NW10	45,330	42,220	46,880	40,660	48,110	44,560	49,790	42,870	5	6	98.4
NE1B	54,930	51,060	56,850	49,130	45,390	42,170	46,910	40,630	5	6	98.6
SW9A	53,910	49,930	55,890	47,950	51,830	49,110	53,100	47,540	5	6	98.1
NW15	50,280	46,510	52,150	44,640	51,610	48,720	52,810	47,060	5	5	98.0
Start of Phase 3					50,040	46,500	51,390	44,660	5	5	98.6
					52,820	50,350	53,980	49,160			99.6
<i>Duration of Phase 2</i>											
End of Phase 2					9,690	14,480	7,500	17,060			99.0
NW9B	58,960	54,370	61,240	52,090	53,890	51,480	55,090	50,380			99.5
SW10A	57,150	53,400	59,020	51,530	58,930	54,590	61,040	52,980	5	5	98.9
NW11	54,660	50,580	56,690	48,550	57,260	53,860	59,020	52,550	5	5	98.8
KTL164(RGR)	53,700	44,200	58,440	39,450	55,710	52,800	57,480	51,500	5	5	98.8
KTL164(UO W)					57,310	52,530	61,260	51,240	100	100	98.5
SW11A(UA)	57,030	48,180	61,450	43,770	58,070	52,900	61,690	51,570	5	5	98.6
	52,410	46,080	55,570	42,920	55,800	52,440	58,050	51,130	5	6	98.6

Sample name	Unmodelled age range (yrs)				Modelled age range (yrs)				Outlier data		Convergence
	68.2% probability from	to	95.4% probability from	to	68.2% probability from	to	95.4% probability from	to	prior	posterior	
SW11A(UO W)	54,300	49,020	56,920	46,400	55,920	52,630	58,070	51,340	5	5	98.6
NW12	57,660	53,300	59,820	51,140	57,700	53,910	59,770	52,480	5	5	98.8
NW13	60,590	55,850	62,950	53,490	60,590	55,930	62,620	53,930	5	5	98.8
SW2C	67,170	62,530	69,480	60,220	64,760	61,010	66,490	59,090	5	5	98.5
KTL158(UO W)	65,770	51,370	72,960	44,180	62,230	54,570	65,090	52,410	5	5	98.9
SW13A(UA)	69,240	60,280	73,720	55,810	64,480	58,810	66,440	55,310	5	5	98.6
SW13A(UO W)	65,170	60,050	67,730	57,490	63,870	59,600	65,620	57,230	5	5	98.7
KTL162(RGR)	74,520	53,100	85,210	42,400	63,360	55,350	65,660	52,510	100	100	98.8
KTL162(UO W)	71,070	53,620	79,770	44,920	63,350	55,500	65,620	52,630	5	5	98.8
NW14	65,580	60,090	68,310	57,360	64,030	59,570	65,800	57,050	5	5	98.7
SW3C	66,450	61,510	68,910	59,050	64,400	60,510	66,210	58,300	5	5	98.6
SW4C	65,470	60,030	68,180	57,320	63,940	59,540	65,730	57,030	5	5	98.8
Start of Phase 2					66,480	62,850	68,690	61,260			98.9
End of Phase 1					74,900	68,790	76,600	65,440			98.1
SW5C	76,020	69,410	79,320	66,110	76,750	72,070	78,900	69,460	5	5	99.1
NW8C	73,270	67,560	76,120	64,710	76,010	71,230	77,820	68,610	5	5	98.8
SW6C	81,260	73,930	84,910	70,270	78,260	73,250	81,400	71,050	5	5	99.1
SW14A	85,270	77,930	88,940	74,270	79,530	73,820	83,170	71,910	5	5	98.6
SW7C	82,330	75,700	85,630	72,390	78,770	73,680	81,940	71,750	5	5	98.9
Start of Phase 1					82,120	74,900	87,410	72,960			96.2

Supplementary Table 12: The CQL code for the Bayesian age model used in Figure 3.

```

Options()
{
  Plot()
  {
    Outlier_Model("General",T(5),U(0,4),"t");
  };
  Sequence()
  {
    Boundary("Start 1");
    Phase("1")
    {
      C_Date("SW7C", calBP(79010), 3318)
      {
        Outlier(0.05);
      };
      C_Date("SW14A", calBP(81600), 3675)
      {
        Outlier(0.05);
      };
      C_Date("SW6C", calBP(77590), 3668)
      {
        Outlier(0.05);
      };
      C_Date("NW8C", calBP(70416), 2857)
      {
        Outlier(0.05);
      };
      C_Date("SW5C", calBP(72715), 3309)
      {
        Outlier(0.05);
      };
    };
    Boundary("End 1");
    Difference("difference 1 top and 1 bottom",
"End 1", "Start 1");
    Boundary("Start 2");
    Phase("2")
    {
      C_Date("SW4C", calBP(62747), 2722)
      {
        Outlier(0.05);
      };
      C_Date("SW3C", calBP(63980), 2471)
      {
        Outlier(0.05);
      };
      C_Date("NW14", calBP(62835), 2745)
      {
        Outlier(0.05);
      };
      C_Date("KTL162(UOW)", calBP(62344), 8732)
      {
        Outlier(0.05);
      };
      C_Date("KTL162(RGR)", calBP(63808), 10727)
      {
        color="green";
        Outlier(1.00);
      };
      C_Date("SW13A(UOW)", calBP(62609), 2564)
      {
        Outlier(0.05);
      };
      C_Date("SW13A(UA)", calBP(64761), 4488)
      {
        color="blue";
        Outlier(0.05);
      };
      C_Date("KTL158(UOW)", calBP(58568), 7211)
      {
        Outlier(0.05);
      };
      C_Date("SW2C", calBP(64851), 2320)
      {
        Outlier(0.05);
      };
      C_Date("NW13", calBP(58217), 2369)
      {
        Outlier(0.05);
      };
      C_Date("NW12", calBP(55479), 2177)
      {
        Outlier(0.05);
      };
      C_Date("SW11A(UOW)", calBP(51659), 2638)
      {
        Outlier(0.05);
      };
      C_Date("SW11A(UA)", calBP(49245), 3169)
      {
        color="blue";
        Outlier(0.05);
      };
      C_Date("KTL164(UOW)", calBP(52606), 4430)
      {
        Outlier(0.05);
      };
      C_Date("KTL164(RGR)", calBP(48947), 4758)
      {
        color="green";
        Outlier(1.00);
      };
      C_Date("NW11", calBP(52621), 2041)
      {
        Outlier(0.05);
      };
      C_Date("SW10A", calBP(55277), 1877)
      {

```

```

    Outlier(0.05);
  };
  C_Date("NW9B", calBP(56664), 2294)
  {
    Outlier(0.05);
  };
  Boundary("End 2");
  Difference("difference 2 top and 2 bottom",
"End 2", "Start 2");
  Boundary("Start 3");
  Phase("3")
  {
    C_Date("NW15", calBP(48394), 1883)
    {
      Outlier(0.05);
    };
    C_Date("SW9A", calBP(51919), 1991)
    {
      Outlier(0.05);
    };
    C_Date("NE1B", calBP(52991), 1935)
    {
      Outlier(0.05);
    };
    C_Date("NW10", calBP(43773), 1558)
    {
      Outlier(0.05);
    };
    C_Date("NW8B", calBP(46347), 1763)
    {
      Outlier(0.05);
    };
    C_Date("SW8A", calBP(42773), 1567)
    {
      Outlier(0.05);
    };
    C_Date("NW9", calBP(39425), 1325)
    {
      Outlier(0.05);
    };
    C_Date("SW7B", calBP(36517), 1325)
    {
      Outlier(0.05);
    };
    C_Date("SW7A(UOW)", calBP(33470), 1222)
    {
      Outlier(0.05);
    };
    C_Date("SW7A(UA)", calBP(32185), 1933)
    {
      color="blue";
      Outlier(0.05);
    };
    C_Date("NW8", calBP(28142), 968)
    {
      Outlier(0.05);
    };
    C_Date("SW6B", calBP(30379), 1350)
    {
      Outlier(0.05);
    };
    Boundary("End 3");
    Difference("difference 3 top and 3 bottom",
"End 3", "Start 3");
    Boundary("Start 4");
    Phase("4")
    {
      C_Date("SW6A", calBP(27324), 1056)
      {
        Outlier(0.05);
      };
      C_Date("NW7", calBP(23815), 950)
      {
        Outlier(0.05);
      };
      C_Date("SW5B", calBP(23026), 1034)
      {
        Outlier(0.05);
      };
      C_Date("SW5A(UOW)", calBP(22024), 782)
      {
        Outlier(0.05);
      };
      C_Date("SW5A(UA)", calBP(22772), 1491)
      {
        color="blue";
        Outlier(0.05);
      };
      C_Date("NW6", calBP(21159), 710)
      {
        Outlier(0.05);
      };
      C_Date("SW4B", calBP(14693), 608)
      {
        Outlier(0.05);
      };
      C_Date("SW4A", calBP(14927), 709)
      {
        Outlier(0.05);
      };
      C_Date("NW5", calBP(12834), 518)
      {
        Outlier(0.05);
      };
    };
    Boundary("End 4");
    Difference("difference 4 top and 4 bottom",
"End 4", "Start 4");
    Interval(N(4000,500));
    Boundary("Start 5");
    Phase("5")
    {

```

```

C_Date("SW3B", calBP(9851), 518)
{
  Outlier(0.05);
};
C_Date("SW3A", calBP(9923), 433)
{
  Outlier(0.05);
};
C_Date("NW4", calBP(8684), 669)
{
  Outlier(0.05);
};
C_Date("SW2B", calBP(8093), 330)
{
  Outlier(0.05);
};
C_Date("SW2A", calBP(8856), 350)
{
  Outlier(0.05);
};
Boundary("End 5");
Difference("difference 5 top and 5 bottom",
"End 5", "Start 5");
Boundary("Start 6");

```

```

Phase("6")
{
  C_Date("NW3", calBP(6122), 319)
  {
    Outlier(0.05);
  };
  C_Date("NW1B", calBP(6365), 262)
  {
    Outlier(0.05);
  };
  C_Date("NW2", calBP(4096), 255)
  {
    Outlier(0.05);
  };
  C_Date("NW1", calBP(2898), 207)
  {
    Outlier(0.05);
  };
  Boundary("End 6");
  Difference("difference 6 top and 6 bottom",
"End 6", "Start 6");
};
};
};

```

SI SECTION 4

Artefact analysis

The entire sorted assemblage from Madjedbebe was counted, sorted into raw material and technological types, and weighed. Raw material types include milky quartz, crystal quartz, silcrete, fine quartzite, buff coarse quartzite, brown quartzite, dark grey quartzite, mudstone, Oenpelli dolerite, weathered volcanic stone, sandstone, Gerowie tuff, chert and glass. Only milky quartz, buff coarse quartzite and sandstone are local to the site, with quartz obtainable from conglomerate seams in the Djuwamba massif sandstone, and quartzite of low to medium flaking quality from the back wall of the shelter, which shows some signs of flaking. The assemblage is overwhelmingly comprised of flakes and flaked pieces, however cores are present in low numbers. For this study, cores are defined as nuclei showing only negative scars and no positive bulbar features. Bipolar cores and flakes are defined as those with crushed initiations at opposed ends, often showing flat or twisted fracture surfaces, pronounced force ripples and occasionally bulbs at both ends. Bipolar technology is most commonly found on quartz artefacts, but was also rarely used on fine quartzite, quartzite, chert and silcrete materials, typically showing small size and extensive reduction. Retouched flakes are defined as flakes that show retouching on one or more margins that in some way modifies the ventral surface and thus originates after the flake was struck. Thinning flakes are defined as very thin, often expanding, somewhat ventrally arched flakes with complex ventral scars and tiny platforms and lipped or crushed initiations (see Clarkson et al., 2015 for illustrations of thinning flakes from Madjedbebe). Convergent flakes are defined as flakes with regular converging margins forming a sharp point (Clarkson et al., 2015 for illustrations of converging flakes from Madjedbebe). Bifacial points are found only in the midden component of the upper 50 cm of the site. These are typically made from chert, fine quartzite, quartz and Gerowie tuff and are extensively invasively flaked and sometimes broken by heat. Counts for raw materials and technological types described above are provided in Supplementary Tables 13 and 14 for Squares B6 and C4, respectively.

The vertical distribution of stone artefacts can be used to investigate mixing of deposits resulting from post-depositional processes. If mixing of artefacts from different depths of the deposit has been very extensive at Madjedbebe, then artefacts of each raw material type might be evenly distributed down the excavated sequence. We tested this with a chi-square test on the association of artefact raw material frequencies by depth with data from square B6. This sample consisted of 12,243 artefacts made from chert, quartz, quartzite, and

silcrete (rare materials were excluded from the chi-square test). The spits were grouped by depth into the seven phases described above. The chi-square test returns a very low p-value, indicating a significantly non-random association of raw materials with phases (chi-squared = 1495.6, $df = 18$, $p\text{-value} < 2.2e-16$) (Supplementary Table 15). This shows that there is a non-random structure in the distribution of raw material and artefacts at Madjedbebe. This argues against extensive mixing of the deposit.

A striking feature of the Madjedbebe assemblage is strong continuity in several key artefact types over the span of occupation, such as grinding stones, edge-ground hatchets, ground ochre and ochre slabs. These four artefact types are found in abundance in all phases of occupation, whereas the chipped stone artefact assemblage changes continuously over time. The impression gained from this pattern is one of constant change in flaked technology, perhaps reflecting changes in mobility, access to raw materials and site function, underlain by strong continuity in ground technologies. While we cannot yet show that ground pigment production was aimed at producing parietal art, there are suggestions this was so in the form of reflective additives, extensive ochre grinding, ochre residues on grinding stones, and fragments of sandstone covered in pigment that may once have been attached to the back wall. This is suggestive that art may well have been a fundamental aspect of activities carried out at the site from initial occupation until the very recent past (May et al. 2017, in press).

Supplementary Table 13: Stone artefact counts by raw material and technological type from Square B6.

Spit	Phase	Total	Quartzite - coarse	Milky quartz	Crystal quartz	Silcrete	Brown and dark grey quartzite	Mudstone	Fine quartzite	Chert	Weathered volcanic	Glass	Gerowie tuff	Thinning flakes	Retouched	Bifacial points	Cores	Bipolar	Convergent flakes	Hatchet flakes/fragments	Grinding stones and fragments	Mica	
1	7	53	10	25	6	1	0	0	9	0	0	2	0	0	0	0	0	0	0	0	0	0	0
2	7	38	3	21	6	0	0	0	8	0	0	0	0	0	0	0	0	5	0	0	0	0	0
3	7	59	3	32	23	0	0	0	0	0	0	0	0	0	1	0	0	0	0	0	0	1	0
4	7	116	23	15	69	0	0	0	8	0	1	0	0	3	0	0	0	20	0	0	1	0	0
5	7	33	11	10	4	0	0	0	5	0	2	0	0	2	0	0	0	0	0	0	0	1	0
6	7	27	13	8	3	0	0	0	2	0	0	0	0	0	0	0	0	1	0	0	0	1	0
7	7	7	2	2	0	0	0	0	2	0	1	0	0	0	0	0	0	0	0	0	0	0	0
8	7	14	3	8	0	0	0	0	3	0	0	0	0	1	1	0	0	3	0	0	0	0	0
9	7	7	1	4	2	0	0	0	0	0	0	0	0	0	0	0	0	0	0	0	0	0	0
10	7	7	0	5	0	0	0	0	1	1	0	0	0	0	0	1	0	0	0	0	0	0	0
11	7	101	6	69	20	0	0	0	1	0	0	0	0	0	0	0	0	0	0	0	0	0	0
12	7	97	6	80	7	0	0	0	1	0	1	0	0	0	0	0	0	0	0	0	0	1	0
13	6	112	3	82	26	0	0	0	0	0	1	0	0	0	0	0	0	0	0	0	0	0	0
14	6	282	0	254	23	0	0	0	0	2	1	0	0	0	0	0	0	8	0	0	0	2	0
15	6	196	2	158	35	0	0	0	1	0	0	0	0	0	0	0	0	1	0	0	0	1	0
16	6	351	4	289	54	0	0	0	0	0	1	0	0	0	0	0	0	1	0	0	0	3	0
17	6	293	0	268	20	1	0	0	0	2	1	0	0	0	0	0	0	4	0	0	0	1	0
18	5	489	3	349	129	1	0	0	0	5	0	0	0	0	0	0	0	20	0	0	0	2	0
19	5	260	2	230	22	1	0	0	0	5	0	0	0	0	0	0	0	0	0	0	1	0	0
20	5	233	1	212	8	0	0	0	0	11	0	0	0	0	0	0	0	0	0	0	0	0	0
21	5	341	1	311	19	1	0	0	0	6	2	0	0	0	0	0	0	0	0	0	0	0	0
22	5	175	4	111	59	0	0	0	0	0	0	0	0	0	0	0	0	7	0	0	0	1	0

Spit	Phase	Total	Quartzite - coarse	Milky quartz	Crystal quartz	Silcrete	Brown and dark grey quartzite	Mudstone	Fine quartzite	Chert	Weathered volcanic	Glass	Gerowie tuff	Thinning flakes	Retouched	Bifacial points	Cores	Bipolar	Convergent flakes	Hatchet flakes/fragments	Grinding stones and fragments	Mica
23	4	192	5	145	31	0	0	0	0	1	0	0	0	0	1	0	0	7	0	0	1	0
24	4	231	10	197	13	0	0	2	0	0	0	0	0	0	0	0	0	9	0	0	2	0
25	4	262	12	187	55	1	0	0	2	2	0	0	0	0	0	0	0	3	0	0	3	0
26	4	381	22	297	47	4	0	0	0	5	0	0	0	0	0	0	1	3	0	0	4	0
27	4	370	22	272	50	5	0	0	10	1	0	0	0	0	0	0	0	3	0	0	7	0
28	4	257	18	208	21	7	1	0	0	0	0	0	0	0	0	0	0	0	0	0	2	0
29	4	678	58	508	64	14	4	1	6	12	1	0	0	0	2	0	0	6	0	0	5	0
30	4	475	24	338	89	6	1	0	9	4	0	0	0	0	1	0	0	11	0	0	4	0
31	4	509	31	390	64	12	0	0	6	4	0	0	0	0	1	0	0	21	0	0	2	0
32	4	496	18	355	63	14	3	0	16	14	0	0	0	0	3	0	1	9	0	0	8	0
33	4	431	28	260	102	10	2	0	22	5	0	0	0	0	0	0	2	11	0	0	2	0
34	4	260	20	123	87	12	1	0	8	6	1	0	0	0	0	0	1	8	0	1	2	0
35	4	279	15	214	35	1	0	0	3	6	0	0	0	0	1	0	1	13	0	0	4	0
36	3	296	30	171	83	1	1	0	2	5	0	0	0	0	0	0	2	12	0	0	2	0
37	3	261	27	156	71	1	0	0	0	3	0	0	0	0	0	0	1	22	0	0	3	0
38	3	306	28	178	80	4	0	0	0	12	0	0	0	0	0	0	0	12	0	0	1	0
39	3	251	2	237	3	0	0	0	1	8	0	0	0	0	0	0	0	5	0	0	2	0
40	3	134	2	129	2	0	0	0	0	0	0	0	0	0	0	0	0	0	0	0	1	0
41	3	273	13	248	6	2	0	0	0	4	0	0	0	0	1	0	0	0	0	0	0	0
42	3	382	22	337	14	0	0	0	0	4	0	0	0	0	1	0	0	6	0	0	0	0
43	3	420	30	320	63	1	0	0	0	1	0	0	0	0	0	0	0	1	0	0	8	0
44	3	129	5	117	5	0	0	0	0	1	0	0	0	0	1	0	1	2	0	0	1	0
45	3	558	6	499	25	2	0	0	0	5	0	0	0	0	1	0	2	3	0	0	8	0

Spit	Phase	Total	Quartzite - coarse	Milky quartz	Crystal quartz	Silcrete	Brown and dark grey quartzite	Mudstone	Fine quartzite	Chert	Weathered volcanic	Glass	Gerowie tuff	Thinning flakes	Retouched	Bifacial points	Cores	Bipolar	Convergent flakes	Hatchet flakes/fragments	Grinding stones and fragments	Mica
46	3	182	13	159	0	0	1	0	0	8	0	0	0	0	0	0	0	2	0	0	1	0
47	2	268	16	235	4	1	1	0	0	9	1	0	0	0	0	0	1	0	0	0	4	0
48	2	167	14	136	3	4	1	1	0	8	0	0	0	0	0	0	0	0	0	0	0	0
49	2	177	22	123	8	1	0	1	4	9	5	0	0	0	0	0	0	1	0	0	3	0
50	2	216	26	165	3	1	0	0	0	8	0	0	0	0	1	0	0	1	0	0	12	0
51	2	236	46	154	9	3	0	0	0	8	5	0	0	0	0	0	1	1	0	3	13	2
52	2	400	53	218	29	7	0	0	11	13	5	0	1	0	1	0	1	5	0	3	29	6
53	2	150	32	91	11	4	1	0	0	2	0	0	0	0	1	0	0	1	0	2	10	0
54	2	206	39	129	17	11	2	1	4	0	1	0	0	3	0	0	0	0	0	1	4	0
55	2	205	34	129	20	8	2	0	6	0	1	0	0	0	0	0	0	9	0	0	8	0
56	2	199	38	127	11	7	7	0	5	2	0	0	0	0	0	0	0	0	0	0	3	0
57	2	394	75	278	17	8	8	0	2	4	1	0	0	5	0	0	1	2	0	1	1	0
58	2	143	55	50	16	5	7	1	5	3	0	0	0	5	1	0	1	1	0	0	0	0
59	2	119	57	36	12	4	2	0	7	1	0	0	0	1	2	0	0	0	0	0	0	0
60	2	78	35	16	13	4	1	0	3	1	0	0	0	2	1	0	0	0	0	0	5	0
61	2	126	65	38	6	10	4	1	1	0	0	0	0	0	1	0	0	0	1	0	0	0
62	2	111	67	25	6	9	2	0	1	1	0	0	0	0	3	0	0	0	0	0	0	0
63	1	64	33	19	3	2	1	0	5	0	0	0	0	1	0	0	0	0	0	0	1	0
64	1	3	2	0	0	1	0	0	0	0	0	0	0	0	0	0	0	0	0	0	0	0
65	1	0	0	0	0	0	0	0	0	0	0	0	0	0	0	0	0	0	0	0	0	0
66	1	1	1	0	0	0	0	0	0	0	0	0	0	0	0	0	0	0	0	0	0	0
67	1	1	0	1	0	0	0	0	0	0	0	0	0	0	0	0	0	1	0	0	0	0
68	1	0	0	0	0	0	0	0	0	0	0	0	0	0	0	0	0	0	0	0	0	0

Supplementary Table 14: Stone artefact counts by raw material and technological type from Square C4.

Spit	Phase	Total	Quartzite - coarse	Milky quartz	Crystal quartz	Silcrete	Brown and dark grey quartzite	Mudstone	Fine quartzite	Chert	Volcanic	Glass	Gerowie tuff	Thinning flakes	Retouched	Bifacial points	Cores	Bipolar	Axe flakes	Grinding stones and fragments	Mica
1	7	34	1	28	0	0	0	0	3	0	0	2	0	1	0	0	0	0	0	0	0
2	7	46	6	26	8	0	1	0	1	1	0	0	0	0	0	0	0	1	0	0	0
3	7	140	6	111	17	0	0	0	4	0	0	1	0	0	0	0	0	2	0	0	0
4	7	112	12	57	24	0	2	0	14	0	0	0	5	2	0	0	0	1	0	0	0
5	7	38	4	35	0	0	0	0	1	0	0	0	0	0	0	0	0	1	0	0	0
6	7	42	3	28	7	0	0	0	2	3	0	0	0	0	0	0	0	0	1	0	0
7	7	131	25	82	9	1	0	0	7	3	1	0	0	4	0	0	0	0	1	0	0
8	7	134	30	78	16	0	0	0	0	4	0	0	1	2	0	1	0	0	0	1	1
9	7	72	4	49	7	0	0	0	5	1	0	0	0	0	0	0	0	0	0	0	1
10	7	82	15	58	5	0	0	0	1	3	0	0	0	1	0	0	0	0	0	0	0
11	7	211	9	183	17	1	0	0	3	0	0	0	0	0	0	0	0	0	0	0	0
12	7	244	2	217	21	0	0	0	1	2	0	0	0	0	0	0	0	0	0	0	0
13	6	379	2	335	46	0	0	0	0	0	0	0	0	0	0	0	0	1	0	0	0
14	6	296	5	244	47	0	0	0	0	0	0	0	0	0	0	0	0	0	0	0	0
15	6	466	5	428	30	0	0	0	0	3	0	0	0	0	0	0	0	0	0	0	0
16	6	329	4	312	13	0	0	1	0	1	0	0	0	0	0	0	0	0	0	2	0
17	6	174	1	138	28	0	0	0	4	2	0	0	0	0	0	0	0	4	0	0	0
18	5	122	2	111	5	0	0	1	0	5	0	0	0	0	0	0	0	0	0	0	0
19	5	319	1	237	73	0	0	2	3	4	0	0	0	0	0	0	0	0	0	0	0
20	5	167	2	150	13	0	0	1	1	0	0	0	0	0	0	0	0	0	0	0	3
21	5	159	6	143	3	1	0	1	0	0	0	0	0	0	0	0	0	0	4	0	0
22	5	105	2	89	6	4	0	0	2	2	4	0	0	0	0	0	0	0	0	0	0

Spit	Phase	Total	Quartzite - coarse	Milky quartz	Crystal quartz	Silcrete	Brown and dark grey quartzite	Mudstone	Fine quartzite	Chert	Volcanic	Glass	Gerowie tuff	Thinning flakes	Retouched	Bifacial points	Cores	Bipolar	Axe flakes	Grinding stones and fragments	Mica
23	4	227	4	210	3	1	0	0	0	6	0	0	0	0	0	0	0	0	0	0	0
24	4	235	2	201	16	2	0	0	2	12	2	0	0	0	0	0	0	0	0	0	0
25	4	227	12	164	15	0	1	0	5	8	5	0	0	0	0	0	0	0	0	0	2
26	4	284	7	229	20	1	0	0	0	17	9	0	0	0	0	0	0	0	0	0	2
27	4	175	2	124	24	0	2	0	2	11	10	0	0	0	0	0	0	0	0	0	1
28	4	123	3	65	45	7	0	0	1	5	3	0	0	0	0	0	0	0	0	0	1
29	4	151	3	88	37	2	0	3	1	7	0	0	0	0	0	0	0	0	0	0	19
30	4	363	5	190	125	1	0	0	0	6	32	0	0	0	0	0	0	0	1	0	2
31	4	222	1	165	45	3	0	0	1	5	7	0	0	0	0	0	0	0	1	0	0
32	4	289	5	184	81	0	0	1	5	5	3	0	0	0	0	0	0	0	0	0	0
33	4	251	2	180	46	1	0	0	0	7	13	0	0	0	0	0	0	0	0	0	0
34	4	182	3	124	55	0	0	0	0	2	0	0	0	0	0	0	0	0	0	0	3
35	4	261	1	167	79	0	0	0	1	3	7	0	0	0	0	0	0	0	0	0	0
36	3	198	1	153	41	0	1	0	0	0	0	0	0	0	0	0	0	0	0	0	0
37	3	260	3	194	59	0	0	0	0	0	1	0	0	0	0	0	0	0	1	0	0
38	3	190	3	138	41	1	1	0	0	2	0	0	0	0	0	0	0	0	0	0	0
39	3	277	5	193	71	1	1	0	5	2	0	0	0	0	0	0	0	0	0	0	1
40	3	310	5	211	77	0	3	0	1	5	7	0	0	0	0	0	0	0	0	0	0
41	3	114	7	90	16	1	0	0	3	0	0	0	0	0	0	0	0	0	0	0	0
42	3	169	6	129	31	0	0	0	0	2	0	0	0	0	0	0	0	1	0	0	1
43	3	80	4	40	28	1	0	1	0	3	5	0	0	0	0	0	0	0	0	2	0
44	3	137	8	106	15	4	0	0	4	10	1	0	0	0	0	0	0	1	1	0	0
45	3	166	14	64	40	10	3	0	7	25	13	0	0	2	0	0	0	0	4	0	0
46	3	151	12	47	23	14	3	2	6	30	1	0	0	5	0	0	0	1	1	0	3

Spit	Phase	Total	Quartzite - coarse	Milky quartz	Crystal quartz	Silcrete	Brown and dark grey quartzite	Mudstone	Fine qtzite	Chert	Volcanic	Glass	Gerowie tuff	Thinning flakes	Retouched	Bifacial points	Cores	Bipolar	Axe flakes	Grinding stones and fragments	Mica
47	2	320	50	119	54	40	5	2	15	19	9	0	0	2	0	0	0	0	1	0	0
48	2	603	55	172	120	44	21	16	32	29	21	0	0	3	0	0	0	0	0	0	35
49	2	291	33	77	58	47	14	12	21	11	13	0	0	3	0	0	1	0	0	1	14
50	2	365	40	107	55	64	13	14	15	10	19	0	0	13	0	0	0	0	0	0	5
51	2	394	25	136	66	49	9	25	27	12	4	0	0	9	1	0	1	0	0	0	1
52	2	416	34	107	83	20	6	22	30	17	13	0	0	13	0	0	0	0	1	0	11
53	2	162	19	53	46	15	2	3	2	3	0	0	0	14	0	0	0	0	0	2	7
54	2	132	8	71	15	4	7	0	2	2	1	0	0	7	0	0	0	0	0	0	1
SF57	2	33	4	12	2	3	1	0	0	2	0	0	0	0	0	0	0	0	0	0	0
55	2	5	3	2	0	0	1	0	0	1	1	0	0	3	0	0	0	0	0	1	0
56	2	8	2	2	3	0	0	0	0	1	0	0	0	0	0	0	0	0	1	0	0
57	2	0	3	0	0	0	0	0	0	0	0	0	0	0	0	0	0	0	0	0	0
58	2	7	8	0	0	1	0	0	0	0	0	0	0	0	0	0	0	0	0	0	0
59	2	8	1	3	3	0	0	0	0	0	0	0	0	0	0	0	0	0	0	0	0
60	2	19	4	9	3	5	0	1	1	1	0	0	0	0	0	0	0	0	0	0	1
61	2	14	4	4	2	2	0	1	0	0	0	0	0	3	0	0	0	0	0	0	1
62	2	9	3	2	5	0	0	0	0	1	0	0	0	2	0	0	0	0	0	0	0
63	1	14	2	7	0	8	0	0	0	1	0	0	0	1	0	0	0	0	0	0	0
64	1	27	7	21	2	2	0	0	0	0	0	0	0	0	0	0	0	0	0	0	0
65	1	9	3	5	4	1	0	1	1	0	0	0	0	0	0	0	0	0	0	0	0
66	1	4	3	3	1	3	0	0	0	0	0	0	0	0	0	0	0	0	0	0	0
67	1	6	2	0	1	0	0	0	0	1	0	0	0	0	0	0	0	0	0	0	0
68	1	5	1	5	2	0	0	0	0	1	0	0	0	0	0	0	0	0	0	0	0
69	1	0	1	0	0	0	0	0	0	0	0	0	0	0	0	0	0	0	0	0	0

Supplementary Table 15: Summary of stone artefact counts by raw material from Square B6 for the chi-square test for non-random association of raw material frequency and phase.

Phase	Chert	Quartz	Quartzite	Silcrete
1	36	1319	632	83
2	49	1754	132	10
3	42	1670	139	9
4	45	1974	179	68
5	15	1629	94	17
6	25	1941	15	4
7	1	279	81	1

SI SECTION 5

Usewear and Residues

Grinding stones

2012 Assemblage: Ninety-one grinding stones were collected during the 2012 field season and examined for usewear and residue traces. Analyses indicated the stones had been used for a range of activities, with evidence for the processing of pigments (n=16 specimens), plants and seeds (n=52), animal tissue (n=4) and stone (n=3). At least 11 specimens were identified as multi-functional tools used to process more than one material.

The earliest grinding stones from the 2012 assemblage with traces diagnostic of worked material come from Phase 2 (spits 44, 42 and 38) and were used for filing/grinding haematite. Red and sometimes yellow mineral pigments were recognised on most grinding stones (n=79), and 16 (~18%) of the 91 tools were considered to have been used for the processing of pigments. Transfer of pigments could have occurred through various agencies including actual use, handling in the past, post depositional processes and post-excavation sieving. Pigments were not considered to be use related unless they were present in lower interstices of the grinding surface, occurred in abundance (i.e. >20% of the artefact surface) and appeared to be “smeared” or have alignments running through them—as was found on experimental filing tools. The earliest grinding stone from the 2012 excavations, UP GS 36 (E2/28A), was recovered from a depth of 222 cm and has compelling evidence for filing red haematite. This stone is a small (82 g) quartzite fragment with the same macroscopic traces of haematite, abrasive smoothing and diagnostic microscopic characteristics found on experimental sandstones used for filing haematite (Extended Data Fig. 3a-f).

Grinding stones used for plant processing, including seeds (n=52; ~57%) were identified from usewear and residue traces consistent with traces on experimental and ethnographic plant processing tools. Diagnostic usewear included highly levelled and smoothed quartz grains and a reticular use-polish forming on abrasively smoothed quartz grains. Typical residues included cellulose fibres, lignified and woody tissue; intact and gelatinised starch grains; microfossils such as raphides, phytoliths and pollen; and various structures of vascular plant tissue, such as perforation plates, sieve cells and bordered pits. The earliest tool with evidence for seed grinding, GS 39 (D1/37) (Extended Data Fig. 3g,h), was recovered from Phase 2 at a depth of 201 cm and has compelling evidence for the processing of seeds. The stone has a macroscopically visible zone of abrasive smoothing with a well-developed micro-polish (Extended Data Fig. 3i-k), diagnostic of grinding small seeds

of siliceous plants. Starch grains (n=6) were documented in ultrasonicated extractions but have not yet been taxonomically identified. GC-MS analysis detected plant compounds consistent with the processing of burnt seeds and nuts. All detected plant compounds were restricted to the grinding surface and were absent from controls (i.e., sediment samples and unground surface).

Grinding stones with evidence for the processing of animal tissue (n=4) were recognised predominately from the presence of a combination of residues, including collagen, bone, hair and/or feathers. Some of these tools also had evidence for the processing of other materials (such as plant or pigment) and were suggested to be multi-functional tools. Stones that were used to work stone (n=3) were identified based on their usewear and morphology. Two water-worn cobblestones were identified as hammers (GS 7 from C2/22A (Phase 5) and GS 18 from D3/26 (Phase 4)) and both contained pounding damage and abrasion/buffing wear. The other specimen was a modern (post European) whetstone, found near the surface of the excavation, and displayed evidence for working metal and stone axes.

2015 Assemblage: Thirty-seven grinding stones were collected during the 2015 field season and are currently being analysed for usewear and residues at the University of Wollongong. At least one of the analysed specimens, GS79 (B6/54) from Phase 2 displayed wear traces consistent with the manufacture and sharpening of stone hatchets (Extended Data Fig. 3m-r). These traces included, at low magnification: (1) a slight (2 mm at the centre) concave curvature across the width of the specimen and a very flat longitudinal cross-section (Extended Data Fig. 3m-p); (2) longitudinal striations running parallel to the long axis are very common and clearly visible at low magnification indicating back and forward motion with a hard material; and (3) removal of the quartz grains and fresh fracturing of the larger quartz grains on the grinding surface making it appear uneven (Extended Data Fig. 3r). At high magnification, the surface of the specimen lacked distinctive polish with the main form of wear being abrasive smoothing. The lack of interconnected polish linkage is not consistent with plant processing or seed grinding. Furthermore, the design of the tool, which has its margins flaked, presumably to deliberately shape the stone to make a relatively uniform thickness and rectangular shape, supports its use as a portable filing stone (Extended Data Fig. 3p,q).

Preliminary analyses on another grinding stone from Phase 2 of the 2015 assemblage, GS 73 (B5/52), has further indicated the probable processing of plant materials. This specimen was found (grinding face down) in sediments below the earliest plant-processing

tool recognized from the 2012 assemblage, at a depth of 2.35 m). This fragment had a large curvature cross section and could possibly represent the ridge and partial groove of a larger (now broken) millstone (Extended Data Fig. 3s-u). At low magnification, parallel striations run longitudinally to the length of the groove where grains have been removed, creating an uneven surface. At higher magnifications, interconnected zones of levelling were documented on the grinding surface. Wear at high magnification is dominantly abrasive smoothing, however, there are several isolated zones where polish appears interconnected (Extended Data Fig. 3l). Such polish is consistent with that documented on plant-processing tools including seed grinding. Associated with this polish are abundant plant fibres, indicating support for a plant processing interpretation. Only one starch grain was documented in pipette extractions sampled from the ground surface. Extraction via ultrasonication is yet to be completed but will likely enhance starch grain recovery. Tiny fragments of haematite are pressed into lower parts of the microtopography at some locations on GS 73, indicating possible grinding of haematite prior to its more recent use (Extended Data Fig. 3l). A smoothed fragment of haematite is pressed on the face up surface.

Edge-Ground Hatchets

Ten complete or large broken fragments of dolerite edge-ground hatchet heads were collected during the 2012 field season. These included six complete specimens (weighing 128–1062 g); two specimens with the butt only (249 and 355 g); and two very weathered but near complete specimens, each comprising numerous eroded fragments (weighing 130 and 356 g) (Supplementary Data Table 16). An additional hatchet head, comprising broken fragments only, was identified initially as a stained ovoid shape during excavation. It was then removed as a pedestalled block and x-rayed to reveal the weathered broken dolerite fragments (EGH 11, Supplementary Table 16). Hafting of hatchet heads was indicated by usewear, residues and morphology (Supplementary Data Table 17). The morphology, size and various designs all suggest a haft made of moulded wood or vine wrapping on gum or resin. Other possible hafting arrangements are being investigated. Residues from use, hafting and pigment mixing were generally in low abundance but distinctive structures and tests indicate presence of starchy tissue and cellulose. Mineral crystals, lignin and unidentified organic tissues were more common on haft zones. Numerous edge-ground hatchet fragments were also recognized throughout the site, including eight specimens with bevelled edges and two ground surfaces.

Supplementary Table 16: Summary data for dolerite edge-ground hatchet heads recovered from the 2012 excavations at Madjedbebe.

Code/Number	Square/Spit	Phase	Ground edge preserved intact	Weight (g)	Length (mm)	Width (mm)	Thickness (mm)	Scarring on blade	Completeness (%)	Preservation	Interpretation
EGH Surface	E2/10	7	YES	463	112	95	26	Yes	100	Good	Hatchet head
EGH 2	D2/27	4	NO	130	68	60	38	?	50	Very poor	Hatchet head
EGH 3	C2/27	4	YES	356	116	87	37	?	80	Very poor	Hatchet head
EGH 4	D2/27	4	NO	249	55	83	36	N/A	25	Fair	Butt only
EGH 10	C4/31	4	NO	355	82	100	30	N/A	25	Poor	Butt only
EGH 1	C1/33	4	YES	892	141	100	51	No	100	Good	Hatchet head
EGH 6	C1/33	3	YES	1062	150	103	44	No	100	Good	Hatchet head
EGH 7	C1/35	Base of 3	YES	128	76	65	25	Yes	100	Poor	Hatchet head
EGH 11	D3/39	Base of 3	No	N/A	N/A	N/A	N/A	N/A		Very poor	Highly fragmented
EGH 8	C1/38	Base of 3	YES	394	98	76	40	Yes	100	Poor	Hatchet head
EGH 9	B1/36	2	YES	267	90	76	29	No	100	Poor	Hatchet head

Supplementary Table 17: Microwear and residues on the working edge and haft zone of dolerite edge-ground hatchet heads. An 'x' indicates presence or a positive result.

Code/Number	Microscope observations				Tests on residues from working edge				Residues from working edge				Tests on residues from haft zone				Residues from haft zone									
	Manufacture flaking B: bifacial, U: unifacial	Pecking visible	Hafting groove (G) or shoulder (S)	Hafting microwear	Wrapping on resin haft	Usewear-scarring	Protein	Carbohydrates	Starch	Fatty acids	Haem	Cellulose (fibres)	Lignin	Mineral crystals	Unidentified organic tissue	Resin fragments	Protein	Carbohydrates	Starch	Fatty acids	Haem	Cellulose	Lignin	Mineral crystals	Unidentified organic tissue	Resin fragments
EGH Surface	B	-	-	x	x	x	x	x	x	-	x	x	-	-	-	-	-	-	-	x	-	x	-	-	-	-
EGH 2	B	?	-	-	x	-	x	x	-	-	x	x	-	-	-	-	-	-	-	x	-	x	-	-	-	-
EGH 3	-	?	-	-	?	-	-	x	-	-	x	-	x	-	-	-	-	-	-	-	-	x	-	-	-	-
EGH 4	B	?	-	-	?	-	-	-	-	-	-	-	-	-	-	-	-	-	-	-	-	-	-	-	-	-
EGH 10	-	?	-	x	?	-	-	-	-	-	-	-	-	-	-	-	-	-	-	-	-	-	-	-	-	-
EGH 6	U	x	G	x	x	x	-	x	-	-	x	x	-	-	-	-	-	-	-	x	-	-	x	-	-	-
EGH 1	B	x	G	x	x	-	x	-	-	-	x	x	-	-	-	-	-	-	-	-	-	x	-	-	-	-
EGH 7	B	x	S	-	x	x	-	x	-	-	-	x	-	-	-	-	-	-	-	x	-	-	-	-	-	-
EGH 9	B	-	-	x	x	x	-	x	-	-	-	-	-	-	-	-	-	-	-	-	-	-	x	-	-	-
EGH 8	-	x	S	-	x	x	-	x	-	-	-	-	-	-	-	-	-	-	-	-	-	-	x	-	-	-

SI SECTION 6

Archaeobotanical Analysis and Hearths

Flotation recovered plant remains from fourteen hearths dating from 240-7 yr cal BP to c. 55 kyr (Supplementary Table 18). The presences of discrete hearths in the upper and lower deposit demonstrate the site's stratigraphic integrity. The taxonomic composition of wood charcoals from these fourteen hearths demonstrate human fuel wood selection predominately targeted open eucalypt woodland and monsoon vine forest. Across the ten most recent hearths there is a clear diachronic shift from a dominance of *Acacia* sp. to higher taxon richness. The oldest Madjedbebe hearth, SF55, located near the back wall, contained six fuel wood taxa and parenchymatous tissue, but was dominated (66% of the identified wood charcoal) by *Acacia* sp. taxa. Details of the composition of all the hearths can be found in Supplementary Table 18.

Flotation was also used to systematically recover macrobotanical remains from all excavated deposits, including the sediment matrix in which hearths were preserved, in two one-by-one metre excavation squares. As demonstrated in Extended Data Figure 7 this allowed for the recovery of macrobotanical remains from all phases of occupation, demonstrating the efficacy of this method in Pleistocene Australian contexts.

Macrobotanical remains recovered from the earliest phase of occupation included *Pandanus* sp. drupe (nutshell) and vegetative parenchyma, the latter probably from geophytes, comprising one of the oldest macrofossil assemblages of plant foods found in an archaeological site globally. It is likely that both these types of plant remains, found within hearths and the general sediment matrix, are the remnants of past plant food exploitation. The kernel of *Pandanus* sp. plants (containing 44-50% fat and 20-34% protein; Low 1991:42) is documented to be an important resource for the Indigenous populations of the Arnhem Land region (Jones and Meehan 1989:122; Meehan *et al.* 1978). In the historic period, metal axes were used to open the drupes in order to pry out the kernels. However, Meehan *et al.* (1978) hypothesise that, pre-contact, fire may have been used in the processing of pandanus kernels prior to their fracturing with stone implements. This is a convincing explanation for the introduction of charred fragments of drupe into the archaeological record, especially as the particularly robust seed locules are present only in heavily fragmented form.

Geophytes are a prominent part of the diet of the Indigenous populations of western Arnhem Land (Jones and Meehan 1989; McArthur 1960; Meehan 1989). As many of these geophytes required cooking to become edible, the entry of fragments of charred vegetative parenchyma into the archaeological record is not surprising (Jones and Meehan 1989; Low 1991;

McArthur 1960; Wightman and Andrews 1989). Further, geophytes, plants which rely on underground organs to regenerate, are designed to survive Australian bushfires (Specht 1994:327). As Specht (1994:327) writes, “although the above-ground part of the vegetation may be razed by fire, these underground organs survive and rapidly regenerate new aerial shoots.” Such a design suggests that, despite their proximity to the site at different environmental phases in prehistory, geophytes would not have been burnt in bushfires.

Comparative taxonomic analysis of the wood charcoals from recent bushfires, one of the most recent archaeological hearths, and general sediment matrix contexts at Madjedbebe (C3/4A, C3/4) confirm that the charcoals from the site matrix are likely to be anthropogenic in origin rather than derived from bushfire sources. A taxonomic comparison of the hearth C3/4A, its surrounding matrix charcoal C3/4, and the charcoal deriving from bushfires drawn from a transect of the local environment was undertaken. A chi-square test for linear trend (Supplementary Table 17) demonstrated a strong, significant compositional difference between the hearth and transect charcoal ($\chi^2 = 149.286$, $p < <0.001$). This difference is driven by a higher taxon richness in the hearth ($n = 12$) than the transect sample ($n = 6$). While there is also a statistically significant difference in the taxonomic composition of the hearth charcoal and that from its surrounding matrix ($\chi^2 = 27.115$, $p = 0.012$), the difference in chi-square value is much lower. The compositional difference between the hearth and the matrix charcoal, caused by the presence of *Alstonia* sp. and *Syzygium* sp. in the matrix sample, cannot be explained by the transect data (modern environmental charcoal) from which they are absent. This analysis therefore demonstrates that the charcoal dispersed in the sedimentary matrix at Madjedbebe was the accumulation of multiple anthropogenic hearths rather than bushfire debris.

Supplementary Table 17: Chi-square test of hearth matrix taxonomic composition.

Context	Chi-square	p-value
Hearths V Matrix	21.115	0.012
Hearths V Transect	149.286	<0.001
Matrix V Transect	104.6426	<0.001

Supplementary Table 19. Madjedbebe hearths, ages, taxonomic composition and sample size.

Hearth	Sediment Feature	¹⁴ C Age (cal yr BP)	Taxonomic composition
E3/5A	20	240 – 7 Wk43609	A hearth measuring 40 x 20 cm in size containing charcoal, burnt bone and shell. This hearth contained fifteen taxa which represented open Eucalypt woodland and monsoon vine forest vegetation communities*. It also contained fragments of polydrupe <i>Pandanus</i> sp. drupes and parenchymatous tissue.
C3/4A	1	260 – 0 OZQ464 – this age range is for C3/4	This hearth measured 30 x 30 cm in size and contained ash and charcoal. The hearth contained eleven taxa and one unidentified angiosperm type. These taxa represent open Eucalypt woodland and monsoon vine forest vegetation communities*. It also contained fragments of polydrupe <i>Pandanus</i> sp. drupes, parenchymatous tissue and fruit endocarp.
E4/6A	7	450 – 300 OZQ460	Hearth measure 60 x 25 cm in size. The hearth was located within the midden. The hearth contained fourteen taxa. These taxa represent open Eucalypt woodland and monsoon vine forest vegetation communities*. It also contained fragments of polydrupe <i>Pandanus</i> sp. drupes and parenchymatous tissue.
B3/5A	3	720 – 650 OZQ471 – this age range is for B3/5	This hearth was directly on top of the midden layer. It contained ash and charcoal, identified as thirteen different taxa. These taxa represent open Eucalypt woodland and monsoon vine forest vegetation communities*. It also contained fragments of parenchymatous tissue.
C4/9A	16	2860 – 2760 Wk43604	This hearth contained ash and charcoal, it was 2 cm thick and 60 x 60 cm in size. It contained six different taxa which represented open Eucalypt woodland and monsoon vine forest vegetation communities*. It also contained fragments of parenchymatous tissue.
C3/18A	41	9130 – 9000 Wk43603	This hearth contained only two taxa, <i>Acacia</i> sp. and <i>Pavetta</i> sp. It was approximately 20 x 15 cm in size. The taxa present are from open Eucalypt woodland and monsoon vine forest vegetation communities*.
D2/21A	44	9398 – 9034 Wk43606	A small hearth, 10 cm diameter and 5 mm thick. This hearth contained seven taxa and one unidentified angiosperm type. <i>Acacia</i> sp. made up 76% of the identified charcoal. The taxa represent open Eucalypt forest and monsoon vine forest vegetation communities*. It also contained fragments of parenchymatous tissue.
D3/16B	33	8360 – 8180 OZQ472 – this age range is for D3/16	A hearth feature containing charcoal and four large rocks. Approximately 35 x 35 cm in size. All of the identified charcoal was <i>Acacia</i> sp. This taxa is found in open Eucalypt woodland and monsoon forest vegetation communities*. It also contained fragments of polydrupe <i>Pandanus</i> sp. drupes and parenchymatous tissue.
E3/20A	43	12810 – 12710 Wk43610	This hearth contained seven taxa and one unidentified angiosperm type. It was dominated by <i>Acacia</i> sp. making up 66% of the total identified charcoal. The taxa present in this hearth are from open Eucalypt woodland and monsoon vine forest vegetation communities*.

Hearth	Sediment Feature	¹⁴ C Age (cal yr BP)	Taxonomic composition
D3/21A	46		This hearth measures 20 x 30 cm in size. It contains four taxa but is dominated by <i>Acacia</i> sp. which accounts for 97% of the identified charcoal. These taxa are from open Eucalypt forest and monsoon vine forest vegetation communities*. It also contained fragments of parenchymatous tissue.
E4/22A	47	18690 – 18410 Wk43611	This is a large hearth measuring 1 x 0.5 m. The hearth contained ten taxa and one unidentified angiosperm type. <i>Acacia</i> sp. is the dominant (37%) charcoal present. These taxa are from open Eucalypt forest and monsoon vine forest vegetation communities*. It also contained fragments of parenchymatous tissue.
D2/30	57		This is a hearth measuring 15 x 15 cm. The hearth contained three taxa identified taxa and one unidentified angiosperm type. The hearth is dominated by <i>Callitris</i> sp. a fire sensitive native pine, but also contains <i>Acacia</i> sp. and <i>Grewia</i> sp. These taxa are from open Eucalypt woodland and monsoon vine forest vegetation communities*. It also contained fragments of polydrupe <i>Pandanus</i> sp. drupes.
C4/36A	56	24970 – 24340 Wk43605	A hearth 30 x 40 cm, surrounded by rocks (including grindstones). This hearth only contained one taxa, the gymnosperm <i>Callitris</i> sp. It did not contain any other botanical remains. <i>Callitris</i> sp. is a fire sensitive taxa found in sheltered areas in open Eucalypt forest and monsoon vine forest vegetation communities*.
C1/43A	55		A small 10 x 10 cm hearth, consisting of very small pieces of charcoal and darker sediment and a retainer stone. The charcoal from the hearth is mainly <i>Acacia</i> sp. as well as five other taxa. These taxa are from open Eucalypt woodland and monsoon vine forest vegetation communities*. It also contained fragments of parenchymatous tissue.

*Wilson et al. 1996

SI SECTION 7

Pigment Characterisation

Portable X-ray fluorescence (pXRF) spectrometry and Synchrotron Powder X-ray diffraction (XRD) analyses have been undertaken to describe pigment residues on sandstone slabs and ground ochre nodules. The chemical and mineral composition of the mulberry/red pigment found on slabs is consistent with the composition of the subsurface ochres, but contain additional chemicals/minerals. This may suggest that the sandstones were exposed to the natural environment for a period of time prior to being incorporated into the deposit (Supplementary Tables 20 and 21). The coeval lack of chemical evidence for weathering products such as silica skins and geological slats that are commonly found in association with rock art in the region may indicate that the slabs were portable objects, rather than once being part of the parietal art within the shelter.

pXRF analyses showed that transition metals (such as Mn, Ba and Ce) correlate strongly with mulberry/red pigment residues found on the subsurface slabs. The pink pigment residues on a small slab found in C1/41 has a different chemical signature. The latter is indicative of evaporite salts previously described for other rock art panels in the region (Watchman, 1985). We, therefore, consider the mulberry/red residues are likely applied pigment and the light pink residues natural precipitates associated with geological weathering (Supplementary Table 20). This is further supported by multivariate analysis of pXRF spectra (Principle Components and Hierarchical Cluster), which revealed that the mulberry/red pigments from ART9 (fragments 3 and 4; Figure 2i) consistently group together, whereas the lighter red pigmentation on fragment 1 of the same artefact consistently separate.

Powder diffraction shows the pigment on ART9 contains quartz, haematite, alunite, phlogopite, lizardite and kaolinite. By contrast, the internal mineralogy of ochre nodules from C4/51 and C4/54 indicates that they are 'pure' iron oxide, comprising 74–100% haematite, with their remaining fraction being quartz. Only in one instance has a minor phase (~3%) of magnetite been observed in the subsurface ochres (Supplementary Table 21).

It is, therefore, of interest that kaolinite, lizardite, alunite and phlogopite are only present on mobile sandstone slab ART9. Phosphate, magnesium and aluminosilicate minerals are common on panels in the Kimberley rock art complex to the west, which has a similar geological/environmental context (Watchman, 1985, 1997; Ford et al., 1994; Ward et al., 2001; Huntley et al., 2015). Previous investigations of silica skins from rock art sites in the Kakadu National Park, predominantly within the Deaf Adder George to the south of Madjedbebe, identified abundant geological salts associated with the precipitate silica, mostly

polyhalite, as well as whewellite and apatite (Watchman, 1985). If we are to assume that the buried slabs at Madjedbebe were once part of a parietal art panel, then the absence of geological salts on these buried slabs is surprising.

Crystallography of the pigment on ART9, specifically the identification of a minor mica phase (phlogopite), supports the microscopic observation of mica flecks within the pigment layer (inset Figure 2i). Phlogopite is known to occur naturally in a mulberry coloured siltstone strata that was exploited as pigment in the Kimberley region (Huntley et al. 2015). However, the mica sheets recovered from Phase 2 (Figure 2k) shows that this reflective mineral was imported into the site as a separate constituent. We suggest that the mica, both in pigment and as a manuport, in the earliest occupation phase shows a clear cultural preference for this reflective mineral. ART9 represents one of the earliest archaeological examples of the anthropogenic use of 'reflective' pigments yet reported. We are currently undertaking a further program of material investigation on the ochre/sandstone slab assemblages from Madjedbebe to further examine pigment use throughout the cultural sequence.

Supplementary Table 20. pXRF spectra from subsurface sandstone slab residues at Madjedbebe. Element concentrations reported in parts per million (relative abundance). CRM refers to n=13 assays collected on certified reference material/internal standard for the dataset (a siliceous Navachab skarn matrix, commonly used for industrial mining applications). Certified values derived from acid digest laboratory XRF. CV is the coefficient of variation. Mean error is the average of error terms reported by the manufactures onboard software.

	MJB Art9	MJB Slab1	MJB Slab3	MJB Slab1 Spec1	MJB Art9 Slab1 Spec1	MJB Art9 Slab3 Spec1	MJB Art9 Slab4 Spec1	MJB Art9 Slab4 Spec2	MJB Art9 Slab4 Spec1 Red	MJB Art9 Slab4 Spec2 Red	MJB C240f Spec1 Red	MJB C226 Art11 Spec1 Black	MJB C141 Spec1 Pink	CRM Mean	CRM SD (standard error)	CRM CV (%)	Mean Error CRM (%)	Certified value (laboratory XRF)
<i>Al</i>	0	0	42456	14606	157777	141300	132986	77195	9379	0	0	0	0	34934	1294	3.71	5.75	35000
<i>Sr</i>	800609	947846	255380	543674	216269	210610	298024	413436	566901	997678	997955	997955	997955	137251	3310	2.41	0.82	141000
<i>P</i>	1155	940	141	1595	3080	1368	2288	2692	824	280	6636	6636	6636	1097	56	5.11	3.17	677
<i>S</i>	0	0	369	0	21296	9853	7670	0	0	0	0	0	0	41947	611	1.46	0.68	<i>Na</i>
<i>K</i>	20653	20580	1990	19747	21282	12229	21433	23956	14613	19966	9234	9234	9234	8182	169	2.07	1.11	14000
<i>Ca</i>	0	0	1098	1122	10417	7910	10346	8066	329	205	260	260	260	81222	1108	1.36	0.32	104000
<i>Ti</i>	1987	932	877	1803	2986	3095	4002	4395	995	1259	1473	1473	1473	2802	50	1.80	2.10	2400
<i>V</i>	0	0	11	0	77	98	20	0	0	0	0	0	0	168	9	5.46	10.12	75.8
<i>Cr</i>	0	0	13	0	140	158	109	0	0	0	0	0	0	176	9	5.33	9.65	132
<i>Mn</i>	21	0	20	99	216	72	219	179	0	0	0	0	0	22204	438	1.97	1.05	28206
<i>Fe</i>	11905	3207	3480	9229	39091	69623	95820	68970	30562	3372	37235	37235	37235	187497	2536	1.35	0.34	186000
<i>Co</i>	15	5	1	4	9	5	46	41	3	6	60	60	60	0	0	0.00	0.00	0
<i>Ni</i>	0	0	11	0	26	34	49	21	0	0	0	0	0	95	5	5.72	15.48	63
<i>Cu</i>	0	0	23	50	84	57	29	46	0	0	0	0	0	1747	56	3.21	4.12	1637
<i>Zn</i>	2	1	2	4	15	16	10	18	0	0	0	0	0	94	4	4.73	13.58	73
<i>As</i>	0	0	0	2	13	23	16	20	4	0	0	0	0	11	1	11.88	19.11	12
<i>Rb</i>	2	0	4	12	21	14	25	22	1	0	0	0	0	56	3	4.49	10.65	77
<i>Sr</i>	357	207	36	368	1496	2316	1805	2325	237	198	45	45	45	131	3	2.00	3.05	341
<i>Y</i>	1	1	0	2	4	5	9	3	0	3	0	0	0	8	1	9.59	25.46	73

	MJB Art9 Slab1 Spec1 Black	MJB Art9 Slab1 Spec1 Rock	MJB Art9 Slab3 Spec1 Dirt	MJB Art9 Slab1 Spec1 Red	MJB Art9 Slab3 Spec1 Red	MJB Art9 Slab3 Spec2 Red	MJB Art9 Slab4 Spec1 Red	MJB Art9 Slab4 Spec2 Red	MJB C240f Spec1 Red Black	MJB C226 Art11 Spec1 Black	MJB C141 Spec1 Pink Red	CRM Mean	CRM SD (standard error)	CRM CV (%)	Mean Error CRM (%)	Certified value (laboratory XRF)
Zr	0	0	413	0	0	0	0	0	0	0	0	36	3	8.54	25.23	60
Ag	0	0	5	0	11	0	9	1	0	1	27	32	6	17.87	58.80	2
Cd	0	0	0	0	0	0	0	0	89	0	0	0	0	0.00	0.00	0
Sn	0	0	1	0	11	17	10	0	0	0	0	62	7	11.53	35.10	4
Ba	0	0	0	0	159	299	155	61	0	0	0	471	203	43.15	43.00	342
La	17	9	0	18	17	17	17	21	9	11	13	7	1	13.48	14.36	15
Ce	0	0	1	24	285	197	210	144	3	0	0	42	2	3.89	24.25	31
U	0	0	0	1	9	12	8	11	0	1	0	8	2	19.31	62.93	7

Loss of Ignition 35100

Supplementary Table 21. Mineral phase identifications of the pigment residues on Art 9 and lower ochres from Square C4. Weight % reported is a percentage of the crystalline material within the samples (additional amorphous material may be present which is insensitive to XRD). The disordered crystal structures Kaolinite, Lizardite and Phlogopite, have not been fully corrected for and results should be considered semi-quantitative (~). Surf = sample from the ochre nodule surface. Int = sample taken after drilling > 5mm into the interior of the ochre piece.

Sample ↓	Mineral Phase (weight %) →	Haematite	Qtz	Magnetite	Alunite	Phlogopite	Lizardite	Kaolinite
MJB_C4_51_HM403_int		89	11					
MJB_C4_51_HM403_surf		29	68	3				
MJB_C4_51_HM404_int		74	26					
MJB_C4_51_HM404_surf		42	58					
MJB_C4_54_7mm_ground_1_3298_int		100						
MJB_C4_54_7mm_ground_1_3298_surf		95	5					
MJB_C4_54_7mm_ground_2_3298_int		100						
MJB_C4_54_7mm_ground_2_3298_surf		100						
MJB_C4_54_7mm_ground_3_3298_seam		98	2					
MJB_PS1 (Art 9 D2/33 Fragment 4)		6	84		2	~4	~4	
MJB_PS2 (Art 9 D2/33 Fragment 4)		4	84		2	~4		~5

SI SECTION 8

Northern Australian Palaeoclimate around 65 kyr ago

Sea-levels between 70 and 65 kyr ago were 75 m lower than the present (Waelbroeck et al., 2002). This is sufficient to turn the Gulf of Carpentaria into a lake (e.g., Reeves et al., 2008), connecting New Guinea to Australia with a broad land bridge and exposing much of the Sahul shelf. Except for the peak of the last glacial maximum (c. 21 kyr ago), this time period represent the shortest distance required, for anytime in the last glacial cycle, to cross from Sunda to Sahul. There was a rapid rise in sea-level after ~65 kyr which would have partially flooded the shelf and made travel between Sunda and Sahul much challenging.

The period from ~75 to 70 kyr was arid with desert dunes active in central Australia from ~73 to 66 kyr ago (e.g., Fitzsimmons et al., 2007). The summer monsoon was likely at a minimum at this time as Lake Eyre was dry (Magee et al., 2004; Cohen et al., 2012). By ~65 kyr the Lake Eyre basin had filled up and a perennial lake occupied the basin for ~5,000 years. Lake Eyre is fed almost exclusively by monsoon moisture from the north and this lake phase indicates a much stronger monsoon than at the present. Rivers also ran more strongly into the Gulf of Carpentaria at this time (Nanson et al., 2008). Thus, the period 70–65 kyr was a phase of intensifying summer monsoons coincident with a summer insolation maximum at ~70 kyr ago, but probably amplified by the rapid flooding of part of the Sahul after the low sea-stand that peaked between ~74 and 70 kyr ago. By ~65 kyr, conditions were favourable for human habitation with a strong summer monsoon active across northern Australia.

SI SECTION 9

Ground pigment from Phase 2

There are 273 pieces of ground pigment from Phase 2 of Square B6 at Madjedbebe, with a combined mass of 3.534 kg. A further 180 pieces of ground pigment are found in Phase 2 of the adjoining square, C6, with a combined mass of 1.651 kg. These are two of the densest accumulations of ground ochre at the site, but all excavated squares contained numerous pieces of ground ochre in Phase 2. More than 6 kg of ground ochre are found in Phase 2 of Squares C4 to B6 (Supplementary Table 22).

Over 25% of the analysed worked pigment pieces have either been flaked or broken, before or after grinding. The majority of these were flaked or broken prior to use. This might suggest preparation of the material before processing to allow for easier ochre procurement or to gain a superior final product.

Almost 60% of the Phase 2 worked pigment assemblage shows minimal working, with on average 1-2 ground facets per piece. Over 20% have 3-5 ground facets per piece, suggesting moderate use, while 3% have been used intensively with over 5, and up to 11, ground facets per piece. Three yellow pieces of ochre recovered from square B6/53 fall into this last category. These pieces were ground down on all sides, suggesting a strong desire for yellow ochre at this time.

In Square B6, it is evident that the intensity of grinding activities on any single piece of haematite increases from Spit 57 onwards. Prior to this, the percentage of ground surface area reached a maximum of around 30% of a piece. From Spit 57 onwards, worked haematite was utilised more thoroughly, with many pieces having at least 50%, and up to 100% of their surfaces ground. A similar pattern occurs in Square C4, where ground surface area increases from a maximum of 25% to over 40% (and up to 95%) from Spit 49 and above.

The most frequent colours for pigments from Phase 2 are various shades of maroon, representing almost 50% of all worked haematite. Over 20% are made up of pink or mulberry coloured ochres, while just over 10% are various shades of red. The remaining assemblage is made up of colours including browns, grey, silver, orange and yellow. It should be noted that the silver pieces are made up of haematite crystals that appear silver but generally grind down into a reddish ochre powder.

In Square C4, the entire Phase 2 pigment assemblage is dominated by a collection of maroon coloured haematite with a blue-silver sheen. Only a couple of pieces of this same material was recovered from Square B6, perhaps suggesting use of different materials in different areas at the site.

Mulberry coloured pigments were present throughout the Phase 2 assemblage, however, this colour became more prevalent during the latter half of the phase. It was noted during analysis of one mulberry coloured piece, however, that the interior was maroon in colour. This is likely due to weathering and chemical processes which alter the exterior surface over long periods of time. It is unclear whether this colour differentiation also occurs with other mulberry coloured ochres recovered from the site.

Reflective Properties

Many of the worked pigment pieces recovered from Madjedbebe (especially the mulberry colours) are reflective, and these account for 30% of the analysed Phase 2 assemblage. It is unknown whether these pieces were chosen specifically because of their reflective surface. Traces of mica or another similar material have been detected within pigment coatings used at the site, and on the surface of at least one piece of worked pigment, suggesting that the reflective properties of these pigments were important in their choice.

Quality

The worked pigment at Madjedbebe is mostly of high quality, with over 50% of the assemblage classified as high quality. Quality is determined by the clay and iron content within a piece. Pigment with a high iron content is difficult to grind and produces a deeper, brown powder, while clay-rich pigments produce softer, redder powders. Slightly higher frequencies of high quality pigment are found towards the back wall (70%) versus the front of the shelter (40%).

Supplementary Table 22: Total counts and weights for the sorted 7 mm and plotted worked pigment from Phase 2, Madjedbebe.

<i>Spit No.</i>	<i>B5</i>		<i>B6</i>		<i>C4</i>		<i>C5</i>		<i>C6</i>	
	Total	Weight (g)								
47			43	735.52	21	32.17	1	34.05	6	177.33
48			23	302.48	13	116.88			32	266.89
49	7	41.41	37	753.32	21	192.68	2	230.77		
50	1	1.57	16	180.86	3	95.49			21	95.50
51	2	54.48	37	471.42	5	174.23			15	59.27
52			28	232.05	3	36.91			6	38.71
53	5	8.49	12	54.34	5				18	115.35
54	1	0.79	12	158.30	5				11	118.60
55			8	35.45	1	1.80			11	35.04
56	1	0.64	7	65.43					8	52.79
57	2	2.66	18	127.47					6	11.03
58	4	9.80	3	62.10					7	87.48
59			11	116.82					11	207.17
60			11	143.92					8	88.19
61	2	2.84	3	31.54					3	40.33
62			1	42.50					8	123.88
63	1	1.31	3	20.41					9	134.29
Total	26	123.99	273	3533.93	77	650.16	3	264.82	180	1651.85

SI SECTION 10

Geoarchaeology

Geoarchaeological investigations at Madjebebe were motivated by two broad goals: 1) to identify site formation processes, and 2) to evaluate site integrity. We undertook several analyses, including granulometry, grain surface texture, micromorphology, carbon isotopes, and magnetic susceptibility to achieve these aims. Here we summarise the key results of these analyses.

Field observations of the sedimentary deposit

The surface of the excavation is a ~10 cm layer of black very silty loose sand containing fine grained charcoal and partially decomposed plant matter. The surface has shallow depressions that indicate recent animal disturbance, most likely kangaroos, especially near the rockshelter wall. Below this surface layer, the upper ~60 cm of deposit is a black silty sand containing gastropods, bivalves, stone artefacts, faunal remains, plant remains and roots, and articulated and disarticulated human remains. Grave-digging to create the Mid Holocene burials has extensively disturbed the upper deposits of the midden (Phase 6). The midden is thickest near the rockshelter wall and tapers slightly with increasing distance from the back wall. Beyond the dripline the midden is absent, presumably due to a combination of rain water dissolving shells, and the focus of past human activity close to the back wall.

The midden includes discontinuous, horizontally linear and amorphous stratigraphic features where the deposit is darker (Extended Data Fig. 7d). We interpret these as a result of differential organic matter accumulation due to plant roots and minor variations in preservation conditions. Plant roots and horizontal channel features of decayed plant roots were observed in and just below the midden deposit. At the base of the midden the deposit grades to a lighter coloured and less silty deposit with less shell and organic content.

The base of the midden forms a highly diffuse and undulating boundary with the massive layer of well-sorted sand that extends to the base of the excavation (Extended Data Fig. 7d). This massive deposit contains almost no organic material except for small amounts of charcoal in hearth features and as rare isolated fragments. Hearth features were distinctive as small localised clusters of charcoal particles, often in sediment that was more compact than the surrounding deposit. Magnetic susceptibility analysis of a sample of hearth shown in Extended Data Figure 7 showed that the mineralogy of the sediment in the hearth had been altered by heating.

Within this massive sand deposit, there are amorphous grey-brown stratigraphic features close to the rockshelter wall. These are probably a result of preservation and diffusion of microscopic charcoal and organic material in the deposit at locations where the deposit was sheltered from rainfall and weathering by the overhang of the rockshelter. Over all of the excavated area this sand deposit becomes increasingly light in colour as depth increases.

In the massive sand deposit underlying the midden there are isolated pieces and isolated clusters of naturally broken rock. The rock is a coarse, banded sandstone, identical to the geology of the rockshelter formation. In one instance we were able to exactly refit a rock found in the excavation with a cavity in the rockshelter wall directly vertically above. This confirms the local origin of the coarse banded sandstone, and that, at least in this one case, there has been minimal disturbance from the rock's original deposit location. These rock deposits sharply increase in density to the front of the excavation, at the dripline of the rockshelter. We interpret this to be a result of accelerated weathering of the rock formation due to exposure to rainfall. There is no pattern in the structure, orientation or size distribution of the rock pieces in the sedimentary deposit.

Granulometry

The particle size results show that most of the texture variation in the deposit relates to changes in the proportions of sand and silt, with clay making up a very small percentage of the deposit (Extended Data Fig. 7a). The proportion of silt peaks in the middle of the midden in Phase 7 and then gradually declines with depth. The proportion of clay is low overall, and drops to below 1% in Phases 1 and 2. This may indicate reduced local weathering during that time, and increased inputs from sand transported from distant locations, suggesting aridity and increased wind speeds.

Stratigraphically constrained cluster analysis of the size distributions identifies chronological phases with similar sediment textures (Extended Data Fig. 7 a). There are two high-level clusters, with Phases 1-4 in one group, and Phases 5-7 in another group. Phases 1-4 have in common high proportions of sand, and very low proportions of silt and clay. Phases 5-7 have greater variability, and generally higher proportions of silt and clay. The upper part of Phase 4 also clusters with Phases 5-6, demonstrating the gradational contact between the silt-rich midden deposit and lower depositional units that are dominated by sand. Phases 5-7 indicate different depositional environments from Phases 1-4, with increased proportions of wind-blown sand in the lower phases. The gradual changes of sediment texture down the

profile that we see in these particle size data are consistent with the field observations of diffuse contacts between deposits.

Grain surface texture

Scanning electron microscope (SEM) images of the surface textures of quartz sand grains from different sedimentary environments has revealed that certain sedimentary processes result in characteristic textures (Margolis and Kennett, 1971; Krinsley and Doornkamp, 1973). These textures and the frequencies with which they occur, in turn, can be used to determine the sedimentary histories of quartz grains. Two representative grains are shown in Extended Data Figure 7c. A grain from the upper part of the deposit at 135 cm (Phase 4) below the surface is an angular quartz grain displaying high-relief, subparallel linear fractures, with occasional linear steps. In the centre of the image the grain has a small fracture face with straight grooves (indicated on Extended Data Fig. 7c by the red arrow on the upper image). These features indicate a freshly-fractured grain that has not been extensively modified by transportation. In contrast, the grain from the lower part of the deposit (320 cm below the surface, Phase 1) shows very well-rounded edges, dish-shaped depressions (indicated on Extended Data Fig. 7c by the red arrow on the lower image), and chattermark fractures characteristic of wind transportation (cf. Bull and Morgan 2006). The variation in surface textures of these representative grains indicates a local source for the upper deposits, in contrast with long-distance transport of wind-carried grains in the lower deposit.

Magnetic susceptibility

The mass-specific low frequency magnetic susceptibility data show several peaks down the deposit. Modification of magnetic minerals in sediments occurs due to both cultural and natural processes (e.g., fires, pedogenesis, chemical weathering, and parent material; Ellwood et al., 1997; Dalan and Banerjee, 1998; Linford, Linford, & Platzman, 2005). At Madjedbebe there are several distinct magnetic susceptibility enhancement events down the sedimentary profile. This shows a clear signal of stratigraphic structure, rather than extensive mixing which would average out the enhanced sediment zones and make the peaks and troughs indistinct. Visual inspection of Extended Data Figure 7b shows weak synchronicity between changes in magnetic susceptibility and changes in burnt artefacts and charcoal. In Phases 3 and 7 there are increases in both magnetic susceptibility and charcoal, but in the other phases there is no clear relationship. This indicates that heating of the sediments may have enhanced magnetic susceptibility in this deposit, but is not the only mechanism. Increases in magnetic

susceptibility values occur during some increases in the number of stone artefacts. For example, in Phases 2 and 4 there are increases in magnetic susceptibility and stone artefacts (and in Phase 4, an increase in charcoal also), but not in Phase 6. These increases may relate to pedogenesis occurring during human occupation of the site, potentially also heating of sediments that were subsequently mixed and dispersed, leaving little charcoal residue. These correlations indicate that magnetic susceptibility values are a credible signal of human occupation at Madjedbebe. Multiple mechanisms are responsible for changes in magnetic susceptibility, these include different combinations of heating of sediments, weathering and pedogenesis.

Carbon isotopes

Soil organic carbon is derived mainly from plants and so closely reflects that of the standing plant biomass (Balesdent et al. 1987). The $\delta^{13}\text{C}$ values in the soil organic matter of sediment samples from Madjedbebe range between -26‰ and -24.2‰ . The tissues of C_3 plants have $\delta^{13}\text{C}$ values ranging from -32‰ to -20‰ , while those of C_4 plants range from -17‰ to -9‰ (Deines, 1980). The values reported here indicate an overall dominance of C_3 plants in the site environs, such as forested-grassland vegetation, including evergreen trees and shrubs (DeNiro, 1987), with no major changes in the vegetation community. The isotope variation of $\sim 2\text{‰}$ is small, and probably related to the isotope fractionation that occurs during the soil organic matter decomposition (Boutton, 1996 and Nadelhoffer and Fry, 1988). However, a primary control on soil carbon isotope values in Australia's deserts and savannas is the annual availability of water in an ecosystem (Wynn and Bird 2008). Drought stress in C_3 plants results in ^{13}C -enriched $\delta^{13}\text{C}$ in living plants because of reduced stomatal conductance. Peak enrichment of $\delta^{13}\text{C}$ at Madjedbebe occurs in Phases 6-7, and if this variation is due to water availability, it may correspond to regional drying trends relating to a northward contraction of the ITCZ at this time, or a more El Niño-dominated system at around 5 kyr ago (Reeves et al. 2013). A gradual enrichment peaks in Phase 3, probably corresponding to Last Glacial Maximum aridity at 30–18 kyr (Reeves et al. 2013). The enrichment of $\delta^{13}\text{C}$ at the boundary of Phases 1 and 2 may reflect the intensification of summer monsoons in OIS 4 (Nanson et al. 2008), as discussed above.

Micromorphology

The two thin sections representing the midden (Extended Data Fig. 7e, f) show a deposit dominated by quartz sand and silt with a wide range of organic components. There is no

microstratigraphy and the orientations of components is highly mixed, suggesting extensive post-depositional disturbance. Organics include shell fragments (indicated by the red arrow in Extended Data Fig. 7e), plant roots (indicated by the blue arrow in Extended Data Fig. 7e), animal bone, charcoal (indicated by the green arrow in Extended Data Fig. 7e) and humified plant matter. In Extended Data Figure 7e we see a rounded quartz grain with a thick, unlaminated silty clay capping. This capping probably resulted from *in situ* soil formation in another part of the deposit from where this grain has been transported.

A common pedofeature in the thin sections from throughout this site are linked-capped grains, for example in Extended Data Figure 7f. This image shows two well-rounded quartz grains with a thin, unlaminated coating of silt and clay. This coating, and fine silt grains within it (indicated by the blue arrow in Extended Data Fig. 7f), link the two grains together. Linked grains are also present in lower parts of the deposit, indicated by the red arrows in Extended Data Figure 7k, l. This pedofeature indicates the formation of a stable surface of linked grains, probably during wet conditions that made the clay and silt mobile, combined with a period of minimal surface disturbance. After the formation of this stable surface, it was disturbed, and most of the linked grains disaggregated, except for small aggregates such as in Extended Data Figure 7f, l. Isolated linked-capped grains are remnants of these stable surfaces, and shows that although bioturbation has been extensive, some microscopic structures are preserved in the deposit. In images Extended Data Figure 7f and l there are large voids between the quartz grains (indicated by the green arrows in Extended Data Figure 7f, l), unlike Extended Data Figure 7e which has fewer voids and more organics and clay between the quartz grains. These voids in Extended Data Figure 7f and l reflect the loss of organic material due to longer exposure to weathering.

Single grains with coatings in the Madjedbebe deposits are also an important pedofeature for understanding site formation processes. The view in Extended Data Figure 7i shows two grains with very different types of coatings (indicated by the red and blue arrows in Extended Data Figure 7i), surrounded by grains with mostly a very thin coating or no coating (indicated by the green arrow in Extended Data Fig. 7i). The grain indicated by the red arrow in Extended Data Figure 7i has an unstructured silty clay coating, similar to the grains in Extended Data Figure 7f, with charcoal inclusions. By contrast, the grain indicated by the blue arrow in Extended Data Figure 7i shows laminated clay pendant coatings, with very few inclusions and restricted to two sides of the grain. These grain coatings result from different processes, likely related to different locations with differences in moisture and

composition of the matrix. The close co-occurrence of these two different types of coatings in Extended Data Figure 7i indicates a high degree of mobility of quartz grains in the deposit at Madjedbebe.

A third important observation from the Madjedbebe thin sections are the charcoal fragments. Charcoal fragments are highly diverse and mixed, with some showing clear vessel structures, some infilled with clay and others empty. Extended Data Figure 7g shows an example of a typical heavily weathered charcoal fragment with clay infill in some vessel voids (indicated by the red arrow in Extended Data Fig. 7g). The rounded outline of this fragment, the deformed vessel voids, and the clay infill indicate a complex taphonomic history including extensive mechanical damage and multiple episodes of wetting and drying. This might be due to an off-site origin for this piece of charcoal and frequent movement within the deposit. A more extensively weathered charcoal fragment is visible in Extended Data Figure 7h, which has substantial clay infills in the voids within the fragment. In Extended Data Figure 7h the quartz grains have only thin clay coatings, or no coatings at all, indicating that the charcoal fragment with its extensive clay fill is an intrusive pedofeature rather than an *in situ* formation. The condition of the charcoal fragments in Extended Data Figure 7g and h contrast with the fragment in Extended Data Figure 7j, with its well-defined outline, mostly intact delicate vessel structures, and minimal clay infilling. Extended Data Figure 7j shows sediment from the hearth in C2/36, so this fragment is likely an *in situ* remnant of the hearth. However no other common traces of combustion features, such as calcitic ashes, phytoliths, burned bone fragments, rubified earth secondary phosphatic minerals (Mentzer 2014), are visible in this thin section, or any of the others. This is due to extensive post-depositional modifications of burned materials in Madjedbebe, most likely due to colluvial reworking and bioturbation. The variable conditions of the microscopic charcoal pieces at Madjedbebe shows the diverse sources and histories of these particles, and their high mobility in the deposit.

Summary

The deposit at Madjedbebe presents macroscale stratification with highly diffuse contacts between layers that primarily vary by texture and organic content. The diffuse nature of the stratigraphic contacts is due to a combination of weathering from seasonal wetting and drying, and bioturbation from flora and fauna, including human trampling. Horizontal variation in the deposit is tied to distance from the back wall and the protection it affords from rainfall. Deposit formation in the midden sediments resulted from human activity,

biological activity, pedogenesis and the accumulation of wind-blown sediments. In the lower layers wind-blown sediments are more prominent, and there are fewer signs of biological activity and pedogenesis. Variation in charcoal and magnetic susceptibility values show some connection with stone artefact discard rates, demonstrating the role of human activity on deposit formation. Carbon isotope values vary over a narrow range, but indicate trends consistent with the regional climate history.

On a microscopic scale, the general pattern is of distinct, but gradual, changes in the deposit with depth. The microstructure and composition of the midden deposits is clearly distinct from the lower layers, and the differences increase gradually with depth. No horizontally-oriented sediment structures are present, but linked-capped pedofeatures indicates that they were once present and have been disturbed. These details imply that although bioturbation is an important factor in site formation at Madjedbebe, it has not removed all traces of sediment structure, and probably did not operate over large vertical distances.

A second key observation from the microscopic analysis is occasional evidence of extensive mobility of individual particles. The highly variable condition of charcoal micro-fragments demonstrates extensive mobility of some particles. Similarly the variety of grain coatings found in close proximity to each other shows mixing of grains from different pedogenic contexts. The implications of these observations of the charcoal fragment is that attempts to date isolated fragments from deposits such as Madjedbebe (cf. Bird et al. 2002) is likely to be problematic because of the high mobility of charcoal in these deposits.

Taken together, these microscopic observations indicate that site integrity at Madjedbebe is related to two processes. First are the frequent, but small distance bioturbation events, and second are the infrequent, but large distance movements of individual particles. The implications for understanding the stone artefact assemblage is that while it is unlikely that any of the artefacts have been recovered from their exact discard context due to frequent small-distance disturbance, it is also unlikely that they have been extensively mixed with artefacts from different major occupational episodes because large-disturbance is rare.

References

- Aitken, M.J., 1985. Thermoluminescence Dating. Academic Press, London.
- Aitken, M.J., 1998. An Introduction to Optical Dating. Oxford University Press, Oxford.
- Arnold, L.J., Demuro, M., Navazo Ruiz, M., Benito-Calvo, A., Pérez-González, A., 2013. OSL dating of the Middle Palaeolithic Hotel California site, Sierra de Atapuerca, north-central Spain. *Boreas* 42, 285–305.
- Arnold, L.J., Duval, M., Demuro, M., Spooner, N.A., Santonja, M., Pérez-González, A., 2016. OSL dating of individual quartz ‘supergrains’ from the ancient Middle Palaeolithic site of Cuesta de la Bajada, Spain. *Quaternary Geochronology* 36, 78–101.
- Balesdent, J., Mariotti, A., Guillet, B. 1987. Natural ^{13}C abundance as a tracer for studies of soil organic matter dynamics. *Soil Biology and Biochemistry* 19, 25–30.
- Bell, W.T., Zimmerman, D.W., 1978. The effect of HF acid etching on the morphology of quartz inclusions for thermoluminescence dating. *Archaeometry* 20, 63–65.
- Bird, M.I., Ascough, P.L., 2012. Isotopes in pyrogenic carbon: a review. *Organic Geochemistry* 42, 1529–1539.
- Bird, M.I., Ayliffe, L.K., Fifield, L.K., Turney, C.S.M., Cresswell, R.G., Barrows, T.T., David, B., 1999a. Radiocarbon dating of “old” charcoal using a wet oxidation, stepped-combustion procedure. *Radiocarbon* 41, 127–140.
- Bird, M.I., Levchenko, V., Ascough, P.L., Meredith, W., Wurster, C.M., Williams, A., Tilston, E.L., Snape, C.E., Apperley, D.C., 2014. The efficiency of charcoal decontamination for radiocarbon dating by three pre-treatments – ABOX, ABA and hypy. *Quaternary Geochronology* 22, 25–32.
- Bird, M.I., Moyo, E., Veenendaal, E., Lloyd, J.J., Frost, P., 1999b. Stability of elemental carbon in a savanna soil. *Global Biogeochemical Cycles* 13, 923–932.
- Bird, M.I., Turney, C.S.M., Fifield, L.K., Jones, R., Ayliffe, L.K., Palmer, A., Cresswell, R., Robertson, S., 2002. Radiocarbon analysis of the early archaeological site of Nauwalabila I, Arnhem Land, Australia: implications for sample suitability and stratigraphic integrity. *Quaternary Science Reviews* 21, 1061–1075.
- Bøtter-Jensen, L., Bulur, E., Duller, G.A.T., Murray, A.S., 2000. Advances in luminescence instrument systems. *Radiation Measurements* 32, 523–528.
- Bøtter-Jensen, L., Mejdahl, V., 1988. Assessment of beta dose-rate using a GM multiscaler system. *Nuclear Tracks and Radiation Measurements* 14, 187–191.
- Boutton, W., 1996. Stable carbon isotopes ratios of soil organic matter and their use of indicators of vegetation and climate change. In: Boutton, T.W., Yamasaki, S., (Eds), *Mass Spectrometry of Soils*, pp. 47–82. Dekker, New York.

- Bronk Ramsey, C., 2009a. Bayesian analysis of radiocarbon dates. *Radiocarbon* 51, 337–360.
- Bronk Ramsey, C., 2009b. Dealing with outliers and offsets in radiocarbon dating. *Radiocarbon* 51, 1023–1045.
- Bronk Ramsey, C., Lee, S., 2013. Recent and planned developments of the program OxCal. *Radiocarbon* 55, 720–730.
- Bull, P., Morgan, R., 2006. Sediment fingerprints: A forensic technique using quartz sand grains. *Science and Justice* 46, 46–107.
- Clarkson, C., Smith, M., Marwick, B., Fullagar, R., Wallis, L.A., Faulkner, P., Manne, T., Hayes, E., Roberts, R.G., Jacobs, Z., Carah, X., Lowe, K.M., Matthews, J., Florin, S.A., 2015. The archaeology, chronology and stratigraphy of Madjedbebe (Malakunanja II): a site in northern Australia with early occupation. *Journal of Human Evolution* 83, 46–64.
- Cohen, T.J., Nanson, G.C., Jansen, J.D., Jones, B.G., Jacobs, Z., Larsen, J.R., May, J.-H., Treble, P., Price, D.M., Smith, A.M., 2012. Late Quaternary mega-lakes fed by the northern and southern river systems of central Australia: varying moisture sources and increased continental aridity. *Palaeogeography Palaeoclimatology Palaeoecology* 356–357, 89–108.
- Dalan, R.A., Banerjee, S.K. 1998. Solving archaeological problems using techniques of soil magnetism. *Geoarchaeology* 13, 3–36.
- Deines, P. 1980. The isotopic composition of reduced organic carbon A2. In: Fritz, P. (Ed.), *The Terrestrial Environment*, pp. 329–406. Elsevier, Amsterdam.
- Duller, G.A.T., 2003. Distinguishing quartz and feldspar in single grain luminescence measurements. *Radiation Measurements* 37, 161–165.
- Duller, G.A.T., 2004. Luminescence dating of Quaternary sediments: recent advances. *Journal of Quaternary Science* 19, 183–192.
- Duller, G.A.T., 2007. Assessing the error on equivalent dose estimates derived from single aliquot regenerative dose measurements. *Ancient TL* 25, 15–24.
- Ellwood, B.B., Petruso, K.M., Harrold, F.B., Schuldenrein, J., 1997. High-resolution paleoclimatic trends for the Holocene identified using magnetic susceptibility data from archaeological excavations in caves. *Journal of Archaeological Science* 24, 569–573.
- Fitzsimmons, K.E., Rhodes, E.J., Magee, J.W., Barrows, T.T., 2007. The timing of linear dune activity in the Strzelecki and Tirari Deserts, Australia. *Quaternary Science Reviews* 26, 2598–2616.
- Ford, B., MacLeod, I., Haydock, P., 1994. Rock art pigments from the Kimberley region of Western Australia: identification of the minerals and conversion mechanisms. *Studies in Conservation* 39, 57–69.

- Galbraith, R.F., Roberts, R.G., 2012. Statistical aspects of equivalent dose and error calculation and display in OSL dating: an overview and some recommendations. *Quaternary Geochronology* 11, 1–27.
- Galbraith, R.F., Roberts, R.G., Laslett, G.M., Yoshida, H., Olley, J.M., 1999. Optical dating of single grain and multiple grains of quartz from Jinmium rock shelter, northern Australia: Part I, experimental design and statistical models. *Archaeometry* 41, 339–364.
- Gillespie, R., Temple, R.B., 1976. Sydney University natural radiocarbon measurements III. *Radiocarbon* 18, 96–109.
- Gillespie, R., Temple, R.B., 1977. Radiocarbon dating of shell middens. *Archaeology and Physical Anthropology in Oceania* XII, 26–37.
- Guérin, G., Mercier, N., Adamiec, G., 2011. Dose-rate conversion factors: update. *Ancient TL* 29, 5–9.
- Guérin, G., Mercier, N., Nathan, R., Adamiec, G., Lefrais, Y., 2012. On the use of the infinite matrix assumption and associated concepts: a critical review. *Radiation Measurements* 47, 778–785.
- Hogg, A.G., Hua, Q., Blackwell, P.G., Niu, M., Buck, C.E., Guilderson, T.P., Heaton T.J., et al. 2013. SHCal13 Southern Hemisphere calibration, 0–50,000 years cal BP. *Radiocarbon* 55, 1–15.
- Huntley, D.J., Godfrey-Smith, D.I., Thewalt, M.L.W., 1985. Optical dating of sediments. *Nature* 313, 105–107.
- Huntley, J., Aubert, M., Ross, J., Brand, H.E.A., Morwood, M.J., 2015. One colour, (at least) two minerals: a study of mulberry rock art pigment and a mulberry pigment ‘quarry’ from the Kimberley, northern Australia. *Archaeometry* 57, 77–99.
- Jacobs, Z., Duller, G.A.T., Wintle, A.G., 2006. Interpretation of single grain D_e distributions and calculation of D_e . *Radiation Measurements* 41, 264–277.
- Jacobs, Z., Roberts, R.G., 2007. Advances in optically stimulated luminescence dating of individual grains of quartz from archeological deposits. *Evolutionary Anthropology* 16, 210–223.
- Jacobs, Z., Roberts, R.G., 2015. An improved single grain OSL chronology for the sedimentary deposits from Diepkloof Rockshelter, Western Cape, South Africa. *Journal of Archaeological Science* 63, 175–192.
- Jacobs, Z., Roberts, R.G., Galbraith, R.F., Deacon, H.J., Grün, R., Mackay, A., Mitchell, P., Vogelsang, R., Wadley, L., 2008. Ages for the Middle Stone Age of southern Africa: implications for human behavior and dispersal. *Science* 322, 733–735.

- Jones, R., and Meehan, B., 1989. Plant foods of the Gidjingali: Ethnographic and archaeological perspectives from northern Australia on tuber and seed exploitation. In: Harris, D.R., and Hillman, G.C. (Eds), *Foraging and Farming: The Evolution of Plant Exploitation*, pp.120-135. Unwin Hyman, London.
- Kammaing, J., Allen, H., 1973. Alligator Rivers environmental fact finding study: report of the archaeological survey. Australian Government, Canberra.
- Krinsley, D.H., Doornkamp, J.C., 1973. *Atlas of quartz sand surface textures*. Cambridge University Press, London
- Lian, O.B., Roberts, R.G., 2006. Dating the Quaternary: progress in luminescence dating of sediments. *Quaternary Science Reviews* 25, 2449–2468.
- Linford, N.T., Linford, P., Platzman, E., 2005. Dating environmental change using magnetic bacteria in archaeological soils from the upper Thames valley, United Kingdom. *Journal of Archaeological Science* 32, 1037–1043.
- Low, T., 1991. *Wild food plants of Australia*. Angus & Robertson Publishing, North Ryde.
- Margolis, S.V., Kennett, J.P., 1971. Cenozoic paleoglacial history of glacial events in a marine core from Frobisher Bay, Baffin Island. *American Journal of Science* 274, 1–36.
- Marwick, B., Hayes, E., Clarkson, C., Fullagar, R., 2017. Movement of lithics by trampling: An experiment in the Madjedbebe sediments, northern Australia. *Journal of Archaeological Science* 79, 73–85.
- May, S.K., Wesley, D., Goldhahn, J., Litster, M. and Manera, B., 2017. Symbols of power: the firearm paintings of Madjedbebe (Malakunanja II). *International journal of historical archaeology* 2017, 1-18.
- May, S.K., Taçon, P.S.C., Wright, D., Marshall, M., Goldhahn, J. and I. Domingo Sanz. In press The rock art of Madjedbebe (Malakunanja II). In: David, B., Taçon, P.S.C., Geneste J.-M., Delannoy, J.-J. (Eds), *The Archaeology of Rock Art in Arnhem Land*. Terra Australis series. Canberra: Australian National University (accepted January 2015).
- McArthur, M., 1960. Report of the nutrition unit: Food consumption and dietary levels of groups of Aborigines living on naturally occurring foods. In: Mountford, C.P. (Ed.), *Anthropology and Nutrition*, pp.90–135. Records of the American Australian Scientific Expedition to Arnhem Land. Melbourne University Press, Melbourne.
- Meehan, B., 1989. Plant use in a contemporary Aboriginal community and prehistoric Implications. In: Beck, J., Clarke, A., Head, L. (Eds), *Plants in Australian Archaeology*, pp.14-30. Anthropology Museum, University of Queensland, Brisbane.
- Meehan, B., Gaffey, P., Jones, R., 1978. Fire to steel: Aboriginal exploitation of pandanus and some wider implications. In: Lauer, P.K. (Ed.), *Readings in Material Culture*, pp.73-96. Occasional papers in anthropology. Anthropology Museum, University of Queensland, Brisbane.

- Mejdahl, V., 1979. Thermoluminescence dating: beta-dose attenuation in quartz grains. *Archaeometry* 21, 61–72.
- Mentzer, S.M., 2014. Microarchaeological approaches to the identification and interpretation of combustion features in prehistoric archaeological sites. *Journal of Archaeological Method and Theory* 21, 616–668.
- Mercier, N., Falguères, C., 2007. Field gamma dose-rate measurement with a NaI(Tl) detector: re-evaluation of the ‘threshold’ technique. *Ancient TL* 25, 1–4.
- Murray, A.S., Roberts, R.G., 1997. Determining the burial time of single grains of quartz using optically stimulated luminescence. *Earth and Planetary Science Letters* 152, 163–180.
- Murray, A.S., Roberts, R.G., 1998. Measurement of the equivalent dose in quartz using a regenerative-dose single-aliquot protocol. *Radiation Measurements* 29, 503–515.
- Murray, A.S., Wintle, A.G., 2000. Luminescence dating of quartz using an improved single-aliquot regenerative-dose protocol. *Radiation Measurements* 32, 57–73.
- Nadelhoffer, K.F., Fry, B., 1988. Controls on natural nitrogen-15 and carbon-13 abundance in forest soil organic matter. *Soil Science Society of America Journal* 52, 1633–1640
- Nanson, G.C., Jones, B.G., Price, D.M., Maroulis, J.C., Coleman, M., Bowman, H.H., Cohen, T.J., Pietsch, T., 2008. Alluvial evidence for major climate and flow-regime changes during the Middle and Late Quaternary in eastern central Australia. *Geomorphology* 101, 109–129.
- Nathan, R.P., Mauz, B., 2008. On the dose-rate estimate of carbonate-rich sediments for trapped charge dating. *Radiation Measurements* 43, 14–25.
- Powell, R., Hergt, J., Woodhead, J., 2002. Improving isochron calculations with robust statistics and the bootstrap. *Chemical Geology* 185, 191–204.
- Prescott, J.R., Hutton, J.T., 1994. Cosmic ray contributions to dose rates for luminescence and ESR dating: large depths and long-term time variations. *Radiation Measurements* 23, 497–500.
- Reeves, J.M., Bostock, H.C., Ayliffe, L.K., Barrows, T.T., De Deckker, P., Devriendt, L.S., Dunbar, G.B., Drysdale, R.N., Fitzsimmons, K.E., Gagan, M.K., Griffiths, M.L., Haberle, S.G., Jansen, J.D., Krause, C., Lewis, S., McGregor, H.V., Mooney, S.D., Moss, P., Nanson, G.C., Purcell, A., van der Kaars, S., 2013. Palaeoenvironmental change in tropical Australasia over the last 30,000 years – a synthesis by the OZ-INTIMATE group. *Quaternary Science Reviews* 74, 97–114.
- Rhodes, E.J., Bronk Ramsey, C., Outram, Z., Batt, C., Willis, L., Dockrill, S., Bond, J., 2003. Bayesian methods applied to the interpretation of multiple OSL dates: high precision sediment ages from Old Scatness Broch excavations, Shetland Isles. *Quaternary Science Reviews* 22, 1231–1244.

- Rhodes, E.J., Schwenninger, J.-L., 2007. Dose rates and radioisotope concentrations in the concrete calibration blocks at Oxford. *Ancient TL* 25, 5–8.
- Roberts, R.G., Jacobs, Z., Li, B., Jankowski, N.R., Cunningham, A.C., Rosenfeld, A.B., 2015. Optical dating in archaeology: thirty years in retrospect and grand challenges for the future. *Journal of Archaeological Science* 56, 41–60.
- Roberts, R.G., Jones, R., 1994. Luminescence dating of sediments: new light on the human colonisation of Australia. *Australian Aboriginal Studies* 1994/2, 2–17.
- Roberts, R.G., Jones, R., Smith, M.A., 1990a. Thermoluminescence dating of a 50,000-year-old human occupation site in northern Australia. *Nature* 345, 153–156.
- Roberts, R.G., Jones, R., Smith, M.A., 1990b. Stratigraphy and statistics at Malakunanja II: reply to Hiscock. *Archaeology in Oceania* 25, 125–129.
- Roberts, R.G., Yoshida, H., Galbraith, R., Laslett, G., Jones, R., Smith, M.A., 1998. Single-aliquot and single-grain optical dating confirm thermoluminescence age estimates at Malakunanja II rockshelter in northern Australia. *Ancient TL* 16, 19–24.
- Rousseeuw, P.J., Croux, C., 1993. Alternatives to the median absolute deviation. *Journal of the American Statistical Association* 88, 1273–1283.
- Rousseeuw, P.J., Debruyne, M., Engelen, S., Hubert, M., 2006. Robustness and outlier detection in chemometrics. *Critical Reviews in Analytical Chemistry* 36, 221–242.
- Smith, M. A., Spriggs, M., Fankhauser, B. L. (Eds). 1993. *Sahul in Review: Pleistocene Archaeology in Australia, New Guinea and Island Melanesia*.
- Smith, M.A., Prescott, J.R., Head, M.J., 1997. Comparison of ^{14}C and luminescence chronologies at Puritjarra rock shelter, central Australia. *Quaternary Science Reviews* 16, 299–320.
- Specht, R.L., 1994. Heathlands. In: Groves, R.H. (Ed.), *Australian Vegetation*, pp.321–344. Cambridge University Press, Cambridge.
- Storey, M., Roberts, R.G., Saidin, M., 2012. Astronomically calibrated $^{40}\text{Ar}/^{39}\text{Ar}$ age for the Toba supereruption and global synchronization of late Quaternary records. *Proceedings of the National Academy of Sciences of the United States of America* 109, 18684–18688.
- Tomiyama, S., Minami, M., Nakamura, T., Mimura, K., Kagi, H., 2016. Changes of chemical structure and composition of charcoal by radiocarbon pretreatments: decontamination by ABA and ABOx treatments. *Radiocarbon* (in press, doi:10.1017/rdc.2016.29).
- Waelbroeck, C., Labeyrie, L., Michel, E., Duplessy, J.C., McManus, J.F., Lambeck, K., Balbon, E., Labracherie, M., 2002. Sea-level and deep water temperature changes derived from benthic foraminifera isotopic records. *Quaternary Science Reviews* 21, 295–305.

- Ward, G.K., Wilson, S.R., 1978. Procedures for comparing and combining radiocarbon age determinations: a critique. *Archaeometry* 20, 19–31.
- Ward, I., Watchman, A., Cole, N., Morwood, M.J., 2001. Identification of minerals in pigments from Aboriginal art in the Laura and Kimberley Regions, Australia. *Rock Art Research* 18, 15–23.
- Watchman, A., 1985. Mineralogical analysis of silica skins covering rock art. In: Jones, R. (Ed.), *Archaeological Research in Kakadu National Park*, Special Publication No. 13, pp. 281–289. Australian National Parks and Wildlife Service, Canberra.
- Watchman, A., 1997. Dating the Kimberley rock paintings. In: Kenneally, K.F., Lewis, M.R., Donaldson, M., Clement, C. (Eds), *Aboriginal Rock Art of the Kimberley: proceedings of a seminar held at the University of Western Australia, Perth, 8th March 1997*. Kimberley Society Occasional Paper No. 1, pp. 39–45. Kimberley Society, Perth.
- Wightman, G.M., Andrews, M.R., 1989. *Plants of the Northern Territory monsoon vine forests*. Conservation Commission of the Northern Territory, Darwin.
- Wilson, B.A., Russell-Smith, J., Williams, R. 1996. Terrestrial Vegetation. In: Finlayson C.M., von Oertzen, I. (Eds) *Landscape and vegetation ecology of the Kakadu region, northern Australia*, pp.57–79. Kluwer Academic Publishers, The Netherlands.
- Wilson, S.R., Ward, G.K., 1981. Evaluation and clustering of radiocarbon age determinations: procedures and paradigms. *Archaeometry* 23, 19–39.
- Wintle, A.G., 2014. Luminescence dating methods. In: Holland, H., Turekian, K. (Eds), *Treatise on Geochemistry*, 2nd ed., vol. 14, pp. 17–35. Elsevier, Oxford.
- Wood, R., Jacobs, Z., Vannieuwenhuysse, D., Balme, J., O'Connor, S., Whitau, R., 2016. Towards an accurate and precise chronology for the colonization of Australia: the example of Riwi, Kimberley, Western Australia. *PLoS One* 11, e0160123.
- Wynn, J. G., Bird, M.I., 2008. Environmental controls on the stable carbon isotopic composition of soil organic carbon: Implications for modelling the distribution of C3 and C4 plants, Australia. *Tellus B* 60, 604–621.